

REVIEWS OF TOPICAL PROBLEMS

PACS numbers: 34.50.Fa, **34.10.+x, 34.70.+e**

Atomic processes involving highly charged ions

I Yu Tolstikhina, V P Shevelko

DOI: https://doi.org/10.3367/UFNe.2022.12.039289

Contents

1. Introduction **1177**
2. Charge-changing processes of ions colliding with atomic particles **1178**
2.1 Ion-atom collisions; 2.2 Electron-ion collisions; 2.3 Ion-ion collisions
3. Ionization of ions by neutral atoms (electron loss) **1180**
3.1 Role of ionization of inner-shell electrons of an ion; 3.2 Specific features of electron-loss processes at relativistic energies; 3.3 Multi-electron ionization; 3.4 Scaling laws for total electron-loss cross sections
4. Electron capture in ion-atom collisions **1184**
4.1 Nonradiative electron capture. Role of capture of the inner-shell electron of target atoms; 4.2 Target-density effects in electron capture and ionization; 4.3 Multi-electron capture; 4.4 Electron capture at relativistic energies
5. Collisions of ions with molecules **1189**
5.1 Bragg's additivity rule; 5.2 Violation of Bragg's rule for cross sections for one-electron capture of ions on H_2 molecules; 5.3 Lifetimes of ion beams in an accelerator. Vacuum conditions
6. Collisions of ions with electrons **1192**
6.1 One-electron ionization; 6.2 Multi-electron ionization of ions by electrons; 6.3 Radiative recombination; 6.4 Dielectronic recombination: ions in plasma and in an incident beam; 6.5 Ternary recombination
7. Interaction of heavy ion beams with media **1200**
7.1 Ionic fractions. Balance equations; 7.2 Equilibrium fractions and average charge of an ion beam upon interaction with a medium; 7.3 Equilibrium target thickness; 7.4 Computer programs for calculating charge fractions of ions. BREIT program
8. Features of interaction of ion beams with plasma **1203**
8.1 Role of dielectronic recombination. DRIMP program; 8.2 Dielectronic recombination of ions in interaction of an ion beam with plasma; 8.3 Charge-state distribution of process rates with account for dielectronic recombination
9. Conclusion **1206**
References **1208**

Abstract. **Atomic processes of ionization, recombination, and electron capture in collisions of positive ions with atoms, ions, electrons, and molecules are considered. The impact of these processes on the interaction of ion beams with media in a wide range of energies — from low to super-relativistic — is discussed, focusing primarily on energies $E \sim$ 10 keV–100 GeV per nucleon. The main features of the effective cross sections of the processes are described as a function of the collision energy, atomic structure, and density effects in gases, solids, and plasmas. The role of dielectronic recombination in the interaction of beams of heavy multi-electron ions with a plasma is considered in detail. The progress in experimental and theoretical studies in accelerator physics and the physics of collisions of heavy ions with atomic systems, achieved over the last five to ten years is reviewed.**

I Yu Tolstikhina [a], **V P Shevelko** [b]
Lebedev Physical Institute, Russian Academy of Sciences,
Leninskii prosp. 53, 119991 Moscow, Russian Federation
E-mail: [a] inga-san@mail.ru, [b] shevelkovp@lebedev.ru

Received 9 November 2022, revised 5 December 2022
Uspekhi Fizicheskikh Nauk **193** (12) 1249 – 1283 (2023)
Translated by M Zh Shmatikov

Keywords: effective cross sections and rates of atomic processes, charge exchange, ionization, dielectronic recombination, interaction of ion beams with gases, plasma, and foils, ion beam lifetime

1. Introduction

This review is a continuation of works [1–3] on the study of elementary processes involving heavy highly charged ions (such as Bi^{q+}, Au^{q+}, W^{q+}, U^{q+}) in atomic and accelerator physics and astrophysics at ion energies $E = 10$ keV/u–100 GeV/u, i.e., from low to ultra-relativistic energies. The amount of information on the interaction of heavy ions with atomic particles — electrons, atoms, ions, and molecules — has increased significantly over the past 10 years due to the rapid development of accelerator technology and the advent of powerful sources of heavy ions, such as NICA (Nuclotron-based Ion Collider fAcility), JINR (Joint Institute for Nuclear Research, Dubna, Russia), CERN (European Organization for Nuclear Research, Geneva, Switzerland), UNILAC (UNIversal Linear ACcelerator, Darmstadt, Germany), BEVALAC (BEVAtron Linear Accelerator, Berkeley, USA), RHIC (Relativistic Heavy IonCollider, Upton, USA), RIKEN (Wako, Japan), and HIRFL (Heavy Ion Research Facility, Lanzhou, China).

Information on effective cross sections (probabilities) and rates of processes involving positive ions is required for research in atomic physics (physics of multiply charged ions, X-ray radiation spectra, QED (quantum electrodynamics) effects, stopping power of matter) [3–9] , in the physics of laboratory and astrophysical plasma (beam diagnostics, energy and charge losses) [10, 11], in the physics of accelerators (lifetimes of ion beams, vacuum conditions, optimization of beam-foil interaction) [12–14], in nuclear physics (detection of superheavy elements using gas-filled separators, study of exotic isotopes) [15, 16], in medicine [17], in materials science [18], etc.

The purpose of this review is to present information on the effective cross sections and rates of elementary processes occurring with a change in the charge state of incident ions colliding with atomic systems and to outline the use of this information in many applications. It is these processes that play the main role in the interaction of ion beams with various media: gases, foils, and plasma. The features of the processes of electron capture and electron loss during the interaction of ions with neutral atoms are considered. These processes are accompanied by a change in the charge state of colliding particles and determine the lifetime of beams of heavy multi-electron ions in planning experiments with accelerators and storage rings in the projects NICA (Dubna) [19–21], Gamma Factory (CERN) [22], FAIR (Germany) [23], etc.

The interaction of ions with molecules (electron capture and electron loss) is considered, which is necessary, for example, for conducting experiments in ion accelerators, where ion beams interact primarily with molecular gases of a vacuum facility containing the molecules H_2, N_2, H_2O, CO_2, CH_4, etc. To estimate cross sections of interaction with molecules, experimental data and theoretical calculations for atomic targets are used, taking into account *Bragg's additivity rule*. According to this rule, the cross section for the interaction of an ion with a molecule is a sum of the cross sections for interaction with the atoms of which the molecule consists. Bragg's additivity rule is used in practice to determine the cross sections for the electron capture and electron loss of ions in collisions with molecular targets. We examine the violation of Bragg's additivity rule in the case of one-electron capture of ions on hydrogen molecules.

The features of the interaction of ions with electrons, in particular, in processes such as one- and multi-electron ionization by electron impact and radiative and dielectronic recombination, are considered. The approximation parameters for determining one-electron cross sections and ionization rates of multiply charged ions in a wide range of energies and temperatures, obtained using numerical calculations, are presented. Radiative and dielectronic recombination during the interaction of ions with electrons plays an important role if an electron beam cooling system is used and strongly affects the beam lifetime in the accelerator. The role of dielectronic recombination in the interaction of ion beams with free plasma electrons is considered for the first time.

The dynamics of the charge state of ion beams interacting with gas, solid-state, and plasma targets is considered. A new definition of the equilibrium target thickness depending on the distribution of equilibrium fractions over the ion charge has been proposed; the dependence of ion fractions on the charge of the incident ion in the beam has been studied, etc. Semi-empirical formulas and parameters for approximating effective cross sections and process rates are presented in a form convenient for their practical application.

We use the system of atomic units $m = e = \hbar = 1$, where m and e are the mass and charge of the electron, and $\hbar$ is Planck's constant.

2. Charge-changing processes of ions colliding with atomic particles

This section provides a list of the main atomic processes occurring during the interaction of ions with atomic particles — atoms, molecules, ions, and electrons — which are accompanied by a change in the charge state of the incident ions. More detailed information about processes and computer programs for calculating the atomic characteristics of the processes is presented in [1–6, 10, 11].

2.1 Ion-atom collisions

Collisions of ions with gaseous and solid (foil) media are primarily characterized by the interaction of ions with target *atoms*. The most common process is *transfer ionization* (TI), when electrons of both colliding particles are simultaneously captured and ionized:

$$X^{q+} + A \to X^{q'+} + A^{k+} + (q' - q + k)\, e^- \,, \qquad (2.1)$$

where q and q' are the charge state of the incident ion X^{q+} before and after the collision, respectively, and k is the charge of the target atom A after the collision. Reaction (2.1) is a multi-electron process accompanied by a change in the charge states of colliding particles and the production of free electrons.

The study of effective cross sections for multi-electron processes (2.1) as a function of ion energy E and charges q, q' and k is a fairly challenging problem. In experiments, this requires the use of a special *coincidence technique*, and, in theoretical studies, solving the problem of multi-electron transitions, taking into account the atomic structure of both colliding particles (see, for example, [1, 3, 24, 25]). In practice, such detailed information about processes (2.1) is usually required quite rarely.

Three important atomic processes are distinguished that are special cases of the TI reaction.

(1) Direct one- and multi-electron ionization of *atoms* by ions, $q = q'$ (pure target multi-electron ionization, PI):

$$X^{q+} + A \to X^{q+} + A^{k+} + k e^- \,, \quad k \geqslant 1 \,. \qquad (2.2)$$

Process (2.2) is more complex than the ionization of atoms by electrons due to the influence of the atomic structure of the incident ion.

(2) Direct one- and multi-electron ionization of incident *ions* by neutral atoms, or, *electron loss* (EL):

$$X^{q+} + A \to X^{(q+k)+} + A + k e^- \,, \quad k \geqslant 1 \,. \qquad (2.3)$$

(3) Nonradiative one- and multi-electron capture (NRC):

$$X^{q+} + A \to X^{(q-k)+} + A^{k+} \,, \quad k \geqslant 1 \,, \qquad (2.4)$$

i.e., a process accompanied by the capture of one or more electrons, which leads to a redistribution of the charge states of colliding particles.

(4) Radiative electron capture (REC), which is the capture of one or more electrons, accompanied by photon emission; usually, a single electron is captured in REC:

$$X^{q+} + A \to X^{(q-1)+} + A^+ + \hbar\omega \,. \qquad (2.5)$$

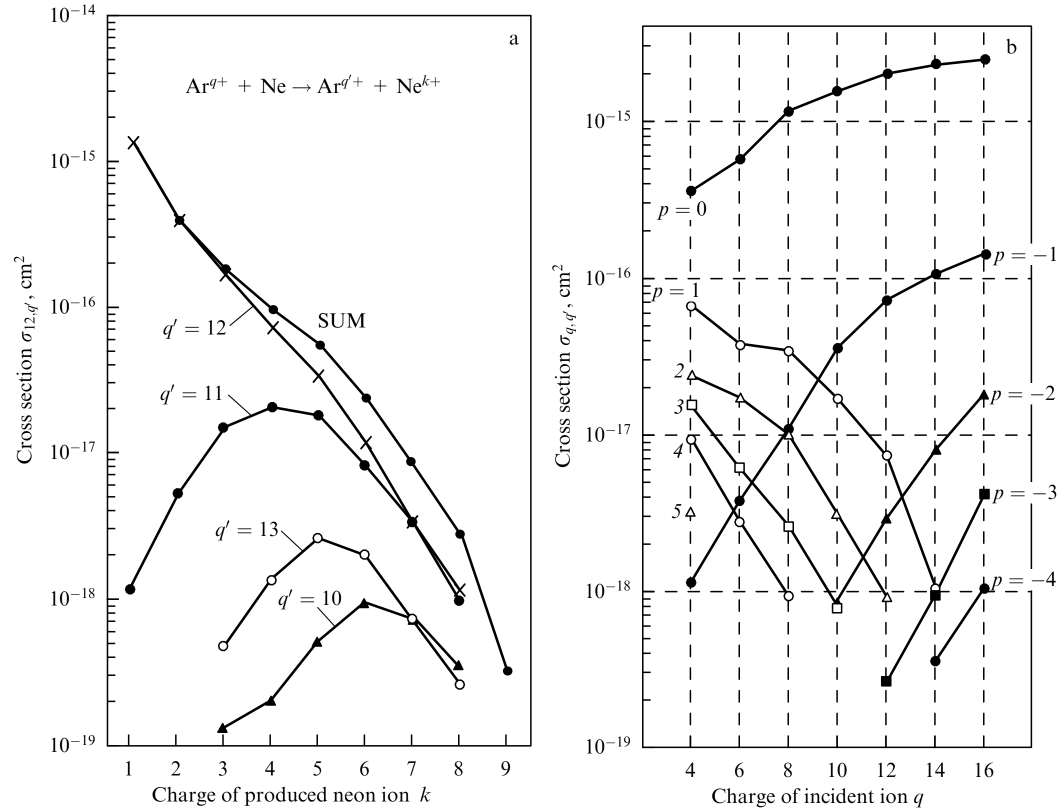

Figure 1. Experimental TI cross sections, reaction (2.6), in the collision of Ar^{q+} ions with Ne atoms at energy $E = 1.05$ MeV/u. (a) TI cross sections for collisions of Ar^{12+} ions with Ne atoms as a function of the number of ionized electrons k. Curve $q' = 12$ presents the cross section for multi-electron ionization of Ne atoms; curves with $q' \neq 12$ show transfer ionization cross sections, SUM is the total cross section, (b) TI cross sections as a function of charge q, summed over all values of k, for various values of $p = q' - q$. Curve $p = 0$ presents the total ionization cross section of Ne atoms, curves $p = 1-4$ are multi-electron-loss cross sections, $p = -(1-4)$ are multi-electron-capture cross sections (2.4). (From [25].)

The REC radiation spectrum depends on the incident ion energy and the atomic structure of the colliding particles. REC plays an important role in collisions of heavy ions with multi-electron atoms and at relativistic energies [26, 27].

Shown as examples in Fig. 1a and b are the experimental effective cross sections of TI processes for the reaction

$$\mathrm{Ar}^{q+} + \mathrm{Ne} \to \mathrm{Ar}^{q'+} + \mathrm{Ne}^{k+} + (q' - q + k)\,\mathrm{e}^- \tag{2.6}$$

at the argon ion energy $E = 1.05$ MeV/u. For $q = 12$, partial cross sections as a function of parameter $k = 1 - 9$ are displayed in Fig. 1a. Curve $q' = 12$ corresponds to the process of pure ionization (2.2), while the remaining curves are the cross sections of reaction (2.6) at $q' \neq 12$; the SUM curve presents the sum of all cross sections.

Experimental TI cross sections of reaction (2.6) as a function of the initial ion charge q for various values of $p = q' - q$ and the cross sections summed for all p are shown in Fig. 1b. The curve $p = 0$ corresponds to cross section (2.2) for the ionization of Ne atoms, $p = 1-4$, to cross sections of multi-electron loss (2.3) of Ar ions, and $p = -(1-4)$, to cross sections of multi-electron capture (2.4).

2.2 Electron-ion collisions

The interaction of ions with electrons is characterized by atomic processes that play an important role in laboratory and astrophysical plasmas, the diagnostics of tokamak plasmas using characteristic emission spectra of ions, accelerator systems for electron cooling of ion beams, studies of the structure of atoms and ions, etc. [2, 12, 28, 29]. The main processes of interaction with electrons are:

(1) One- and multi-electron ionization (multiple ionization, MI):

$$\mathrm{X}^{q+} + \mathrm{e}^- \to \mathrm{X}^{(q+k)+} + \mathrm{e}^- + k\mathrm{e}^-\,, \quad k \geqslant 1\,. \tag{2.7}$$

In the case of ionization of heavy multi-electron ions, the contribution of multi-electron ionization to the total cross section may exceed 50%.

(2) Three-body recombination (ternary recombination, TR):

$$\mathrm{X}^{q+} + \mathrm{e}^- + \mathrm{e}^- \to \mathrm{X}^{(q-1)+} + \mathrm{e}^-\,, \tag{2.8}$$

which is the inverse process to ionization by electrons and plays an important role in dense and low-temperature plasma [4, 30, 31].

(3) Radiative recombination (RR), the capture of free electrons (plasma) by ions with the emission of photons:

$$\mathrm{X}^{q+} + \mathrm{e}^- \to \mathrm{X}^{(q-1)+} + \hbar\omega\,. \tag{2.9}$$

Process (2.9), which occurs at *all* energies of free electrons, plays an important role in the cooling of ion beams by an electron beam in accelerating systems (electron cooling) (Section 5.3.3).

(4) Dielectronic recombination (DR):

$$\mathrm{X}^{q+} + \mathrm{e}^- \to [\mathrm{X}^{(q-1)+}]^{**} \to \mathrm{X}^{(q-1)+} + \hbar\omega\,, \tag{2.10}$$

a process involving photon emission, which is accompanied by the capture of a free electron and simultaneous excitation of an inner electron in the ion [5, 32]. Unlike radiative recombination, DR has a *resonant* character, since it only occurs at certain (resonant) values of the kinetic energy of a free electron (Section 6.4). Along with RR processes, dielectronic recombination plays an important role in the interaction of heavy ions with plasma and in the electron cooling of ion beams in accelerator systems (Sections 6.3 and 6.4).

2.3 Ion-ion collisions

Information about ion-ion collisions is required for studying processes in nonequilibrium laboratory and astrophysical plasmas, thermonuclear fusion, the interaction of ion beams with plasma, etc. (see [3, 5, 6, 33]). The main processes that occur during ion-ion collisions are:

(1) Direct ionization:

$$X^{q+} + A^{q'+} \to X^{(q+k)+} + A^{q'+} + ke^- , \quad k \geqslant 1 . \qquad (2.11)$$

The cross sections of such processes are small compared to those of ion-atomic processes due to the large influence of the Coulomb repulsion of colliding ions.

(2) Electron capture:

$$X^{q+} + A^{k+} \to X^{(q-1)+} + A^{(k+1)+} . \qquad (2.12)$$

Ion-ion electron capture occurs with a low probability for the same reason (Coulomb repulsion); however, if the charges of incident ions are small, $q = 1, 2$, their contribution to the total cross section can be comparable to that of ionization by electron impact.

3. Ionization of ions by neutral atoms (electron loss)

3.1 Role of ionization inner-shell electrons of an ion

Experimental data on ionization cross sections and theoretical methods for calculating cross sections for the ionization of heavy ions by neutral atoms and molecules (*electron loss* cross sections),

$$X^{q+} + A \to X^{(q+k)+} + \sum A + ke^- , \quad k \geqslant 1 , \qquad (3.1)$$

can be found in [1–3]. The term $\sum A$ in reaction (3.1) is an indication that the target atom can be excited or ionized.

Experimental data for the cross sections for one- and multi-electron loss of heavy ions were obtained primarily for beams passing through gas targets H_2, He, N_2, O_2, Ne, Kr, Xe, and molecular gases in the nonrelativistic energy region $E < 200$ MeV/u. At relativistic energies, $E > 200$ MeV/u, experimental data are available primarily for H- and He-like ions (Section 3.2).

Currently, a large amount of theoretical data on the cross sections for one-electron loss of atoms and ions has been obtained in the relativistic approximation using RICODE and RICODE-M computer codes (see [34] and [35], respectively), which use the relativistic interaction operator. The more advanced RICODE-M program uses relativistic electron wave functions for bound states and the continuum, unlike RICODE, where nonrelativistic wave functions are used. The RICODE-M program is intended for calculating

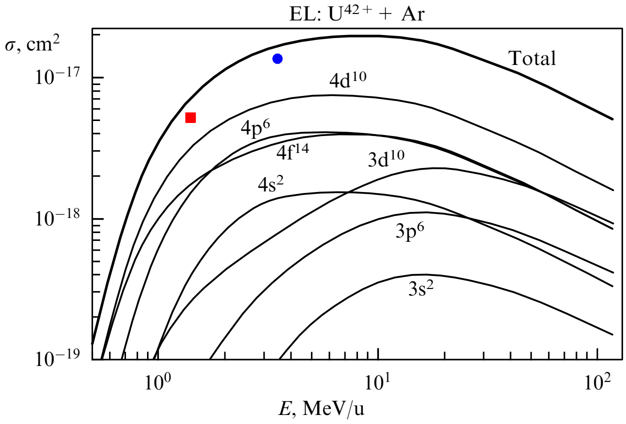

Figure 2. Cross sections for one-electron ionization (electron loss) of U^{42+} ions by Ar atoms as a function of ion energy. Curves with the indication of shells nl^N are the cross sections of ionization of these shells, Total is the total cross section calculated using the RICODE program. Experiment: square, $E = 1.4$ MeV/u [38]; dot, $E = 3.6$ MeV/u [39]. (From [40].)

the electron-loss cross sections of atoms and ions from the hydrogen atom to superheavy elements with a nuclear charge of up to $Z = 120$ in a collision with an arbitrary heavy particle from a proton to heavy atoms and ions at an ion energy of 10 keV/u $< E <$ 100 GeV/u. At medium and lower energies, it is necessary to take into account multi-electron ionization, which significantly affects the total cross sections even in the ionization of multiply charged ions (Section 3.3).

In one-electron ionization of a heavy multi-electron ion by neutral atoms, a significant contribution is made by the ionization of electrons in the *inner* shells of the initial ion. This feature is explained by two main factors: close values of binding energies $I(nl)$ in heavy ions and a large number of electrons in the filled p^6, d^{10}, and f^{14} shells.

Figure 2 shows the electron-loss cross sections of U^{42+} ions with the electron configuration $1s^2 \ldots 3s^2\,3p^6 4s^2\,4p^6\,4d^{10}\,4f^4$ by Ar atoms. In the region of the maximum at $E \approx 10$ MeV/u, the contribution to the total ionization cross section of electrons of the $4d^{10}$ and $4f^4$ shells is $\sim 40\%$: $\sigma(4d^{10}) + \sigma(4f^4) \approx 1.2 \times 10^{-18}$ cm^2, and the total cross section is $\sigma_{tot} \approx 2 \times 10^{-17}$ cm^2. The binding energies of U^{42+} ion shells are quite close: $I_P(4f^4) \approx 2.0$, $I_P(4d^{10}) \approx 2.3$, $I_P(4p^6) \approx 2.7$, and $I_P(4s^2) \approx 3.0$ eV, respectively [36]. In relatively 'light' ions, the $I(nl)$ values rapidly increase in passing from outer to inner shells [37]. For example, in the $Ar^{6+}(1s^2 2s^2 2p^6 3s^2)$ ion, the binding energies are $I_P(3s^2) \approx 124$, $I_P(2p^6) \approx 373$, and $I_P(2s^2) \approx 447$ eV, respectively.

At high, but not relativistic energies, the cross section of ionization of an ion by an atom with a nuclear charge Z_T from a *single* electron shell decreases according to the Bethe–Born formula (Born approximation):

$$\sigma^{B}_{EL} \sim Z_T^2 \frac{\ln E}{q^2 E} , \qquad (3.2)$$

where q and E are the charge and energy of the incident ion, respectively. The total contribution of the ionization of inner electrons of incident ions leads not only to a significant increase in cross sections but also to a weakening of the quadratic dependence Z_T^2 in Eqn (3.2):

$$\sigma_{sum} = \sum_k \sigma_k \sim Z_T^{a(q)} , \quad 1.3 \leqslant a(q) \leqslant 1.8 . \qquad (3.3)$$

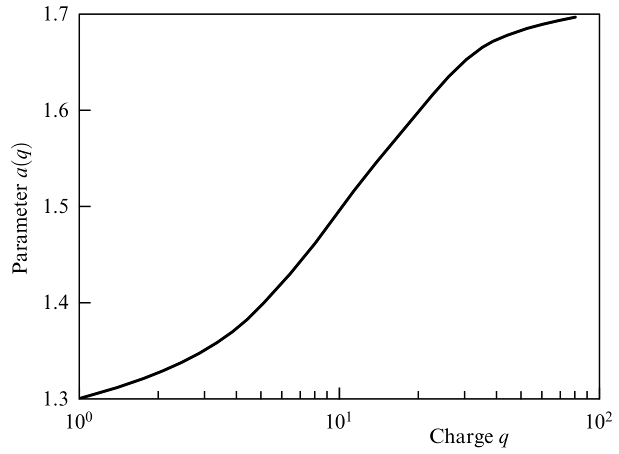

Figure 3. Power exponent $a(q)$ in Eqn (3.3) as a function of charge q for U^{q+} ions with energy $E = 100$ MeV/u in collisions with H, N, and Ar atoms numerically calculated using the RICODE program. (From [34].)

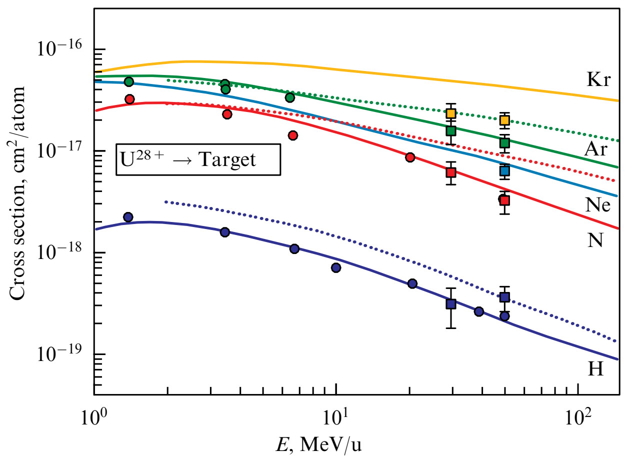

Figure 4. Total electron-loss cross sections of U^{28+} ions in collisions with H, N, Ne, Ar, and Kr atoms. Dashed curves are CTMC calculation [43]; solid curves are calculations using the DEPOSIT and RICODE programs; symbols indicate experimental data. (From [44].)

Figure 3 shows the dependence of the power exponent $a(q)$ on the charge q in the ionization of uranium ions U^{q+} by neutral atoms, obtained using the RICODE program. The increase in $a(q)$ with increasing ion charge q is associated with screening of the effective charge acting on the ionized (active) electron of the incident ion. Namely, for low-charge ions ($q \leqslant 10$), weakly bound outer-shell electrons are ionized at large impact parameters, when the charge of the atom nucleus is screened by its electrons, while electrons of multiply charged ions ($q \gg 1$) are ionized at small impact parameters, at which the screening of the target atom charge Z_T is much weaker.

Figure 4 shows the experimental cross sections for the electron loss of U^{28+} ions in collisions with H_2, N_2, Ne, Ar, and Kr atoms (symbols) in comparison with calculations obtained by the classical trajectory Monte Carlo (CTMC) method (dashed curves) and using the DEPOSIT and RICODE programs (solid curves). Experimental cross sections for H_2 and N_2 molecules were obtained using Bragg's additivity rule (Section 5.1), i.e., by dividing by 2. The DEPOSIT program [41, 42] is intended for calculating cross sections for one- and multi-electron ionization of ions by neutral atoms at low and medium collision energies (Section 3.3). It can be seen that the CTMC data overestimates the cross sections at high energies, while the cross sections calculated using the DEPOSIT and RICODE programs agree with experiment significantly better.

3.2 Specific features of electron-loss processes at relativistic energies

At relativistic energies, the nature of the ionization of heavy ions by neutral atoms changes dramatically: the main contribution is made by one-electron ionization, and the cross sections no longer decrease with increasing energy and become quasi-constant, which is due to the influence of purely relativistic effects of interaction between the ion and the atom. Born asymptotic behavior (3.2) is replaced by weak energy dependence of the cross sections, and the dependence on atomic parameters can be estimated using the semi-empirical formula [34]

$$\sigma_{\mathrm{EL}}^{\mathrm{rel}} \sim {Z_{\mathrm{T}}}^2 I_{\mathrm{P}}^{-0.01q}\,, \tag{3.4}$$

where Z_{T} is the atomic number of the target atom, and q, I_{P} are the charge and ionization potential of the incident ion.

The quasi-constant behavior of the cross sections is the most important feature of the electron loss of heavy ions in collisions with neutral atoms at relativistic energies $E > 200$ MeV/u (ion velocity $v > c/2$, c is the speed of light). This feature determines the lifetime of heavy ion beams at relativistic energies (Section 5.3).

In collisions with target *ions*, the ionization cross section increases with increasing energy as $\ln\gamma$ [45] due to the strong Coulomb interaction between colliding particles:

$$\sigma_{\mathrm{EL}}^{\mathrm{rel}} \sim Z_{\mathrm{T}}^2 \ln\gamma\,, \quad \gamma = \left(1 - \frac{v^2}{c^2}\right)^{-1/2}, \tag{3.5}$$

where γ is the relativistic factor.

Basic experimental results on ionization cross sections and ion fractions at energies $E = 80-1000$ MeV/u of heavy ions from Xe to U in collisions with gas and solid targets from Be to U are reported in [46], where a description of computer CHARGE and GLOBAL programs widely used to calculate ion fractions in collisions of relativistic beams of heavy ions with atomic targets is also presented. Currently, one of the most accurate methods for calculating relativistic electron-loss cross sections is the relativistic Born approximation, taking into account the relativistic (magnetic) interaction between colliding particles and using relativistic wave functions [47–54].

In the relativistic approximation, the matrix element of ionization (electron loss) has the form

$$M_{if} = \left\langle f \middle| (1 - \beta\alpha) \exp(\mathrm{i}Qr) \middle| i \right\rangle, \tag{3.6}$$

where Q is the momentum transfer, $\beta = v/c$ is the relativistic factor, α is the Dirac matrix component, r is the distance from the ion nucleus, and $|i\rangle$ and $|f\rangle$ are the total wave functions of the system in the initial and final states.

The first term in Eqn (3.6) corresponds to the 'ordinary' Born approximation, which describes the electric (Coulomb) interaction between colliding particles, while the second term represents the relativistic (magnetic) interaction with the Liénard–Wiechert potential, the order of magnitude of

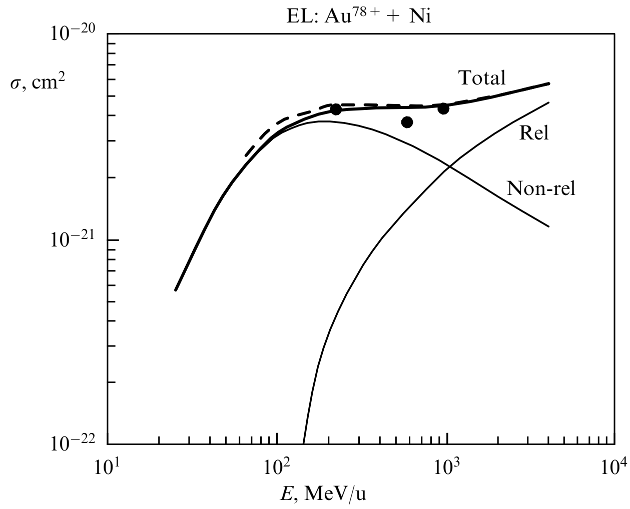

Figure 5. Cross sections for ionization (electron loss) of H-like Au^{78+} ions by nickel atoms as a function of ion energy. Circles show experimental data [53]; dashed line represents a relativistic calculation [46]. Solid curves are calculations using the RICODE-M program [35], thin curves are the contribution of relativistic (Rel) and nonrelativistic (Non-rel) parts of interaction (3.6). Total — total cross section, this work.

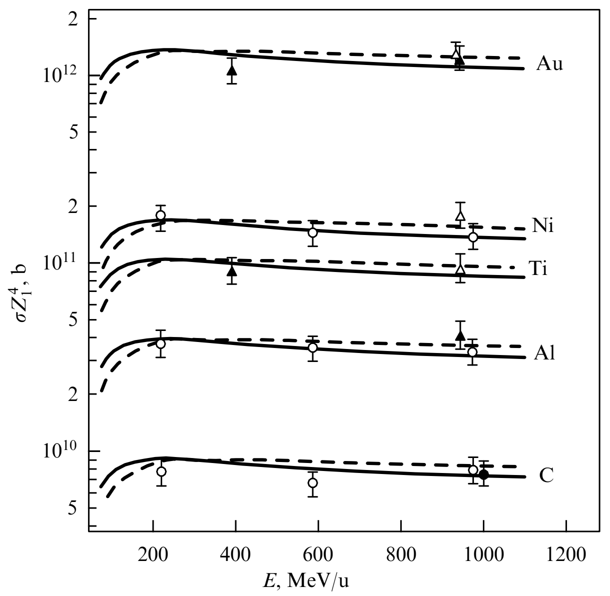

Figure 6. Scaled ionization (electron loss) cross sections of H-like ions of gold, $Z_1 = 78$, and bismuth, $Z_1 = 82$, in collisions with C, Al, Ti, Ni, and Au atoms as a function of ion energy. Symbols — experiment [53]. Solid and dashed curves represent relativistic calculations of the interaction of gold ions Au^{78+} and bismuth Bi^{82+}, respectively, with neutral atoms indicated in the figure. (From [46].)

which is

$$\beta\alpha \sim \frac{v}{c}\frac{\langle p_{\mathrm{e}}\rangle}{m} \sim \frac{v}{c}\frac{v_{\mathrm{e}}}{c}\,, \tag{3.7}$$

where m, v_{e}, and $\langle p_{\mathrm{e}}\rangle$ are the mass, orbital velocity, and matrix element of the momentum of the active electron in the incident ion, and c is the speed of light. Equation (3.7) shows that the relativistic interaction is greatest ($\beta\alpha \sim 1$) when both velocities, of the ion v and electron v_{e}, are close to the speed of light.

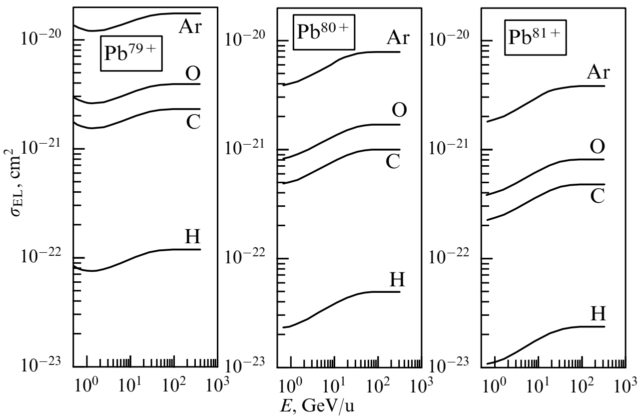

Figure 7. Relativistic cross sections for ionization (electron loss) of Pb^{79+}, Pb^{80+}, and Pb^{81+} ions in collisions with H, C, O, and Ar atoms as a function of ion energy calculated using the RICODE-M program. (From [54].)

Figure 5 shows the contributions of the relativistic and nonrelativistic parts of interaction (3.6) to the total ionization cross section of an H-like gold ion in collisions with nickel atoms. Up to an energy $E \sim 400$ MeV/u, the cross section is well described by the Born nonrelativistic matrix element $\langle f|\exp(\mathrm{i}Qr)|i\rangle$; at $E > 400$ MeV/u, the cross section rapidly decreases according to law (3.2), and the contribution coming from the increasing relativistic part of the cross section described by the matrix element $\langle f|\beta\alpha\exp(\mathrm{i}Qr)|i\rangle$ begins to grow. The calculated total section in the region $E = 100-4000$ MeV/u is primarily determined by relativistic interaction, weakly depends on energy, and is in good agreement with experimental data (dots) and relativistic calculations of other authors [46].

Figure 6 shows the scaled ionization cross sections of H-like gold ions Au^{78+} and bismuth Bi^{82+} in passing through C, Al, Ti, Ni, and Au foils as a function of ion energy. Experimental data (symbols) are in good agreement with calculations for K-electrons of incident ions [46] made using relativistic wave functions and the relativistic Liénard–Wiechert interaction potential.

Finally, Fig. 7 presents calculations of the relativistic ionization cross sections of H-, He-, and Li-like lead ions in collisions with H, C, O, and Ar atoms, which are the basic components of the residual accelerator gas. Calculations were carried out using the RICODE-M program [35] based on the use of relativistic interaction (3.5) and relativistic wave functions for electrons in a bound state and a continuous spectrum. The cross sections displayed in Fig. 7 were used to estimate the lifetimes of relativistic lead ions in the Gamma Factory project (CERN) (Section 5.3).

3.3 Multi-electron ionization

At relatively low and medium collision energies, the cross sections for the ionization of heavy ions by neutral atoms,

$$\mathrm{X}^{q+} + \mathrm{A} \to \mathrm{X}^{(q+k)+} + \sum \mathrm{A} + k\mathrm{e}^-\,, \quad k \geqslant 1\,, \tag{3.8}$$

are characterized by a significant contribution (up to 70%) of multi-electron ionization, i.e., the large ratio

$$\sum_{k \geqslant 2} \frac{\sigma_k}{\sigma_{\mathrm{tot}}}\,, \quad \sigma_{\mathrm{tot}} = \sum_{k=1}^{N} \sigma_k(v)\,, \tag{3.9}$$

where N is the total number of electrons in the X^{q+} ion, v is its velocity, and σ_k is the partial cross section of k-electron ionization.

Experimental data on the total electron-loss cross sections of heavy ions were obtained primarily in the large accelerators Super-HILAC (LLL), LEIR (CERN), the Texas A&M cyclotron, and GSI (Darmstadt) at energies $E \approx 1$ keV/u–160 MeV/u (see references in [41]). These data show that σ_{tot} cross sections reach the maximum at the velocity

$$v_{\max}^2 \sim 0.75\, I_{\text{P}} \,, \tag{3.10}$$

where I_{P} is the ionization potential of the ion in Ry units (1 Ry = 13.606 eV). Table 1 presents experimental data for the electron-loss cross sections σ_k and σ_{tot} of Ar, Xe, and U ions. It can be seen that, even for the relatively light multiply charged Ar^{8+} ion with 10 electrons, the contribution of multi-electron processes (3.8) is about 50%. It is also seen that the contribution of k-electron ionization increases with increasing atomic number of the target atom.

Calculations of multi-electron ionization cross sections σ_k and σ_{tot} for heavy ions, which provide a satisfactory description of the experimental data, were carried out in the classical approximation using the Monte Carlo CTMC method [57–59] and the energy transfer method (DEPOSIT program) [41, 42]. Both approaches yield approximately the same accuracy of 50–80% in calculating sections. As an example, Fig. 8 shows the experimental partial σ_k ($k = 1-4$) and total σ_{tot} cross sections for multi-electron ionization of Ba^{2+} ions by oxygen atoms in comparison with calculations made using the DEPOSIT program [41]. Calculation of electron-loss cross sections taking into account multi-electron processes is very quite complicated and requires information about the binding energies of all inner shells of heavy ions, which is very scarce. For example, for uranium ions, calculations of binding energies are often used [36], and for ions of elements up to $Z_{\text{n}} \leqslant 30$ inclusive (up to zinc), semi-empirical data are employed [37].

In the intermediate-energy region, the classical total electron-loss cross sections decrease much more slowly than the Born cross sections for one-electron ionization:

$$\sigma_{\text{EL}}^{\text{cl}} \sim E^{-a(Z_{\text{T}})}\,, \quad a(Z_{\text{T}}) < 1\,, \quad \sigma_{\text{B}} \sim E^{-2}\,, \tag{3.11}$$

which is due to the large contribution of multi-electron ionization of the ion. According to calculations using the DEPOSIT program [61], the power exponent $a(Z_{\text{T}})$ in Eqn (3.11) depends on the atomic number (Z_{T}) of the target atom:

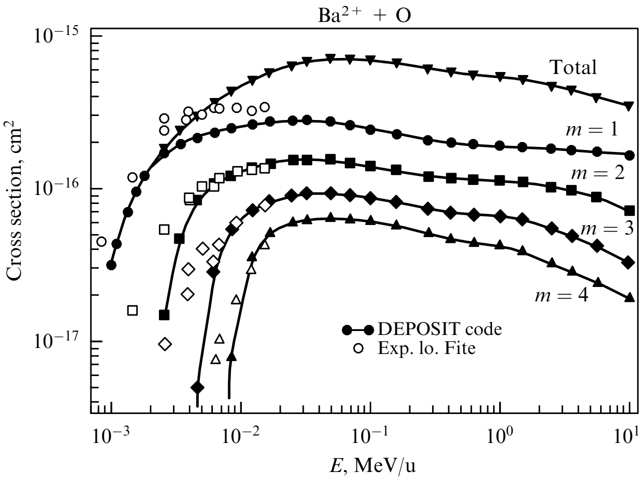

Figure 8. Multi-electron-loss cross sections σ_k, $k = 1-4$, and total cross section (Total) of Ba^{2+} ions ($Z_{\text{n}} = 56$) in interaction with oxygen atoms. Unfilled symbols — experiment [60], curves — calculations using the DEPOSIT program. (From [42].)

$$a(Z_{\text{T}}) \approx \frac{0.8}{Z_{\text{T}}^{0.3}}\,; \tag{3.12}$$

for example, for hydrogen atoms, $a(\text{H}) = 0.80$, for nitrogen, $a(\text{N}) = 0.44$, and for others, $a(\text{Ar}) = 0.34$, $a(\text{Xe}) = 0.24$, etc. Calculations using the DEPOSIT program also showed that the program can be used at ion velocities

$$v > 0.1 v_0\,, \tag{3.13}$$

where $v_0 = 2.2 \times 10^8$ cm s^{-1} is the atomic unit of velocity.

At low and ultra-low energies $v \sim (0.001-0.01)v_0$, to estimate electron-loss cross sections in atom-atom and ion-atom collisions, analytical models of the classical impulse approximation are used [61, 62], the accuracy of which is on the order of a factor of 3–5.

3.4 Scaling laws for total electron-loss cross sections

In practice, to estimate cross sections for atomic processes, semi-empirical formulas are often used, which are obtained on the basis of experimental data and fairly accurate theoretical calculations. In [63], a large number of experimental data were analyzed for the total electron-loss cross sections of σ_{tot} ions from Ar^{6+} to U^{63+} in collisions with targets from H_2 to Xe in the energy range $E = 1-150$ MeV/u

Table 1. Experimental electron-loss cross sections (in units of 10^{-18} cm^2) of Ar^{8+}, Xe^{18+}, and U^{q+}, $q = 28-42$, in collisions with inert gas atoms, where σ_1, σ_2, σ_3, and σ_{tot} are the cross-section single-, double-, and ternary ionization and total cross sections, respectively. (From [3].)

Reaction	Energy, MeV/u	σ_1	σ_2	σ_3	...	σ_{tot}	$\sum_{k \geqslant 2} \sigma/\sigma_{\text{tot}}$, %	Source
Ar^{8+} + Xe	19.0	23	10	5.5	...	44	48	[55]
Xe^{18+} + He	6.0	3.0	1.7	0.2	...	4.9	39	[56]
Xe^{18+} + Ne	6.0	16	7.8	3.8	...	36	56	[56]
Xe^{18+} + Ar	6.0	24	11	5.6	...	56	57	[56]
Xe^{18+} + Kr	6.0	27	13	7.2	...	75	64	[56]
Xe^{18+} + Xe	6.0	34	16	9.0	...	95	64	[56]
U^{28+} + Ar	3.5	13.4	6.8	4.6	...	40.6	67	[38]
U^{31+} + Ar	3.5	12.5	5.9	3.9	...	34.7	64	[38]
U^{33+} + Ar	3.5	8.7	4.4	3.5	...	26.3	67	[38]
U^{39+} + Ar	3.5	8.0	4.1	2.9	...	19.7	59	[38]
U^{42+} + Ar	3.5	6.7	3.2	2.0	...	13.8	51	[38]

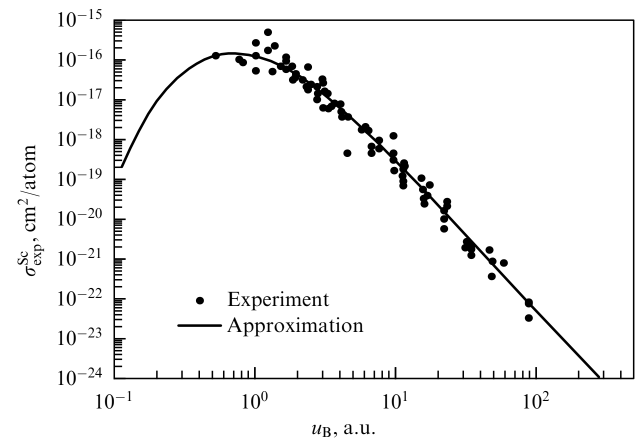

Figure 9. Scaled total cross sections for electron loss of ions by neutral atoms (3.14). Dots — experimental data; solid curve — Eqn (3.15). (From [63].)

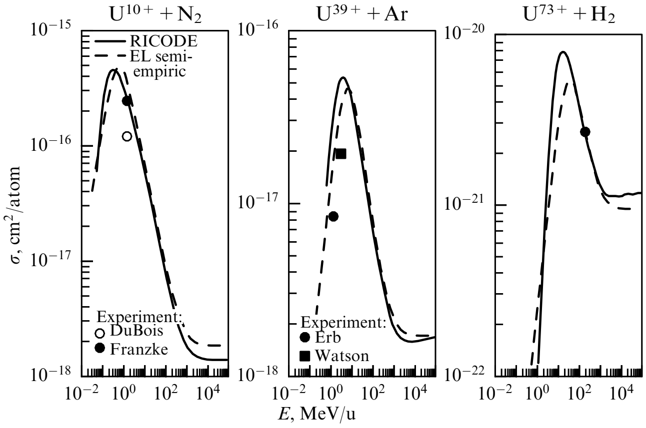

Figure 10. Cross sections of one-electron loss of uranium ions U^{q+}, $q = 10$, 39, 73 in collisions with atoms and gas molecules as a function of ion energy. Experiment: $U^{10+} + N_2$ — • [64], ○ [65]; $U^{39+} + Ar$ — • [36], ■ [56]. $U^{73+} + H_2$ — • [66]. Solid curves — calculations using the RICODE program [34], dashed curves — Eqn (3.16). (From [34].)

(i.e., up to the relativistic region $E > 200$ MeV/u). The cross-section scaling law was obtained in the form

$$\sigma^{\rm sc}(u) = \sigma_{\rm tot}\,\frac{I_{\rm P}^{1.5}}{u^{2.7}\,Z_{\rm T}^{1.3}}\,, \quad u = \frac{v^2}{I_{\rm P}}\,, \tag{3.14}$$

where v and $I_{\rm P}$ are the velocity and ionization potential of the incident ion in atomic units and $Z_{\rm T}$ is the atomic number of the target atom. Scaled experimental data in coordinates (3.14) are approximated by a semi-empirical formula accurate to a factor of 2–3 (Fig. 9):

$$\sigma^{\rm sc}(u)\,[{\rm cm^2\,atom^{-1}}] = 1.28\times10^{-16}\,u^{-0.934} \times 10^{-2.63\,[\log u]^2 + 1.20\,[\log u]^3 - 0.295\,[\log u]^4 + 0.040\,[\log u]^5 - 0.0025\,[\log u]^6}\,. \tag{3.15}$$

In [34], based on numerical calculations using the RICODE program, a semi-empirical formula was obtained for the cross sections for one-electron loss of heavy ions in reactions with neutral atoms in a wide energy range, including the relativistic region:

$$\sigma[{\rm cm^2\,atom^{-1}}] = 0.88\times10^{-16}(Z_{\rm T}+1)^2\,\frac{u}{u^2+3.5} \times I_{\rm P}^{-(1+0.01q)}\left[1 + \frac{1.31}{n_0}\,\ln\,(4u+1)\right], \tag{3.16}$$

$$u = \frac{v^2}{I_{\rm P}} = \frac{(\beta c)^2}{I_{\rm P}}\,, \tag{3.17}$$

where $I_{\rm P}$ and q are the ionization potential in Ry units and the charge of the original ion, and c is the speed of light ($c = 137$ a.u.).

Cross section (3.16) reaches its maximum at $u \approx 2$:

$$\sigma_{\rm max}[{\rm cm^2\,atom^{-1}}] \approx 10^{-16}(Z_{\rm T}+1)^2 I_{\rm P}^{-(1+0.01q)}\,, \quad u \approx 2\,, \tag{3.18}$$

and, in the relativistic region, $v \to c$, the cross section tends to a constant value

$$\sigma[{\rm cm^2\,atom^{-1}}] \approx 3\times10^{-20}(Z_{\rm T}+1)^2 I_{\rm P}^{-0.01q}\,, \quad v \sim c\,. \tag{3.19}$$

Equation (3.16) for $u > 2$ is accurate up to a factor of 2, as is shown in Fig. 10 for the cross sections for the electron loss of uranium ions in collisions with gas atoms. The cross sections for the electron loss of ions in reactions with molecules are calculated using Bragg's additivity rule (Section 5.1).

Finally, the electron-loss cross sections can be represented in a scaled form, taking into account the properties of semi-empirical formula (3.16), as shown in Fig. 11 for the cross sections for ionization of uranium ions by hydrogen atoms. It can be seen how, with increasing energy and ion charge, relativistic effects significantly change the *shape* of the electron-loss cross sections.

4. Electron capture in ion-atom collisions

4.1 Nonradiative electron capture. Role of capture of the inner-shell electron of target atoms

We discuss in this section the features of one-electron capture

$$X^{q+} + A \to X^{(q-1)+} + A^+ \tag{4.1}$$

at energies $E > 1$ keV/u. Electron capture at low energies $E < 1$ keV/u is considered in [1], and multi-electron capture, in Section 4.3.

At energies $E \sim 1-25$ keV/u, the incident ion captures an electron from the outer shell of the target atom into a large number of excited states of the $X^{(q-1)+}$ ion, the energy of which is close to the ionization potential of the A atom. Due to the total contribution of electron capture to the excited states, the total cross section becomes *quasi-constant*, i.e., weakly depends on energy E [67–70]. The cross section is proportional to the charge q of the incident ion according to the model of tunneling of the electron being captured through the Coulomb barrier created by the atom and the incident ion [70]:

$$\sigma\,[{\rm cm^2}] \approx 10^{-15}\,\frac{q}{I_{\rm T}^{3/2}}\,, \quad q > 5\,, \quad v^2 < I_{\rm T}\,, \tag{4.2}$$

where $I_{\rm T}$ is the ionization potential of the atom in Ry units. According to this model, primarily populated are the levels of

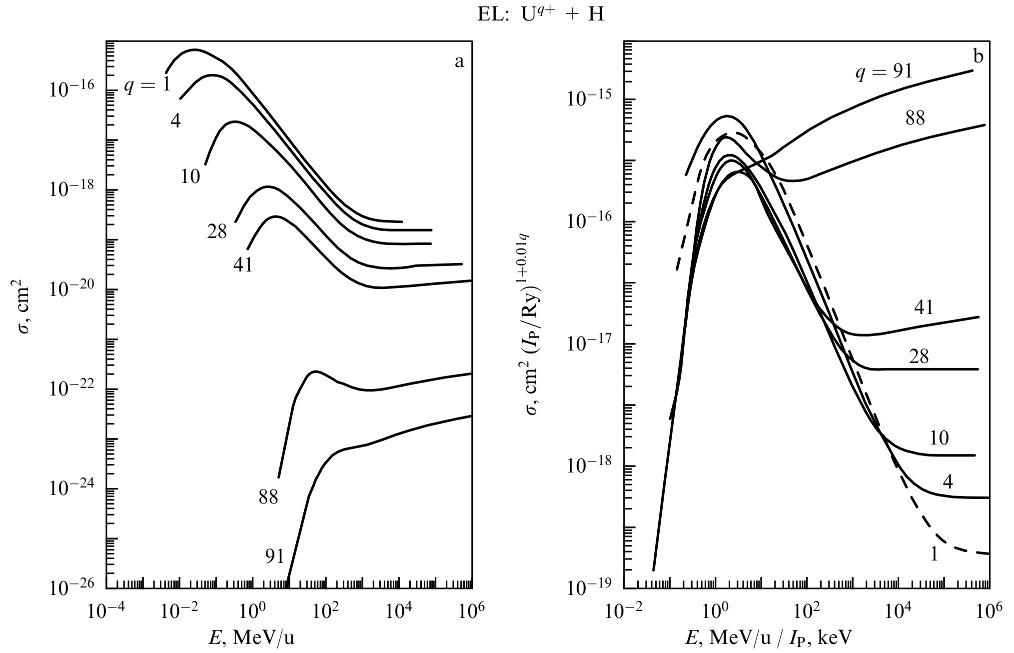

Figure 11. Cross sections for one-electron ionization of uranium ions U^{q+}, $q = 1-91$, by hydrogen atoms. (a) Calculations using the RICODE program, (b) the same in scaled form.

$X^{(q-1)+}(n)$ ions with principal quantum numbers n:

$$n \approx \frac{q^{3/4}}{I_T^{1/2}} \,. \tag{4.3}$$

With increasing energy, $E \sim 25$ keV/u–30 MeV/u, the structure of the electron shells of the target atom begins to play a more significant role: the capture of electrons from the *inner* shells becomes the main, predominant process, which is a feature of nonradiative electron capture, distinguishing it from other ion-atomic processes at these collision energies. The cross section for the capture of a target electron from one shell of the target rapidly decreases approximately as $\sim E^{-5.5}$ (in contrast to the ionization and excitation cross sections, which decrease as $\sim E^{-1}$), and the capture of electrons from the *inner* shells, whose orbital velocity v_e is close to the velocity of the incident ion v, becomes significant — this is the so-called velocity *matching condition*. The cross section for the capture of *outer* electrons becomes negligibly small in contrast to electron capture at low and medium energies.

As a result, the electron capture cross section summed over the target shells decreases according to the law

$$\sigma_{\text{tot}}(E) \sim E^{-a}\,, \quad 1 < a < 5.5\,. \tag{4.4}$$

The value of the parameter a depends on the contribution from the capture of inner electrons to the total cross section; the larger the contribution, the smaller is a, i.e., the slower the decrease in the total cross section summed over the shells. The maximum value $a = 5.5$ is attained at high energies, when the main contribution comes from the capture of 1s electrons of the target. For this reason, the cross sections of electron capture on light atoms H and He decrease much faster than on heavy atoms such as Ne, Ar, Xe, which have a large number of electron shells.

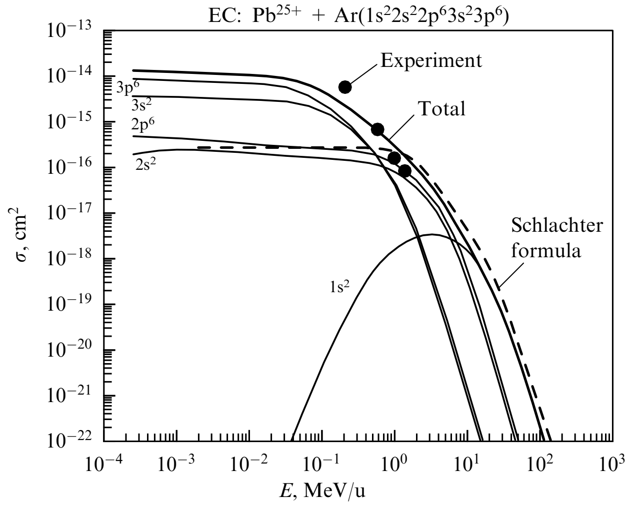

Figure 12. Cross sections for electron capture of Pb^{25+} ions on argon atoms as a function of ion energy. Dots — experiment [36]; dashed curve — semi-empiric Schlachter formula [72]. Solid curves — calculation using the CAPTURE program [71] with indication of the shells of the argon atom from which electrons are captured; thick curve — total (summed over all shells) electron-loss cross section, this work.

This feature is illustrated in Fig. 12, where the cross sections of electron capture of Pb^{25+} ions on argon atoms, calculated using the CAPTURE program [71], are compared with experimental data [36]. As the ion energy increases to $E \sim 0.8$ MeV/u, electrons from the outer 3p^6 and 3s^2 shells of argon are captured; at $E = 0.8$–10 MeV/u, electrons from the inner 2p^6 and 2s^2 shells are captured; and at $E > 10$ MeV/u, the capture of 1s^2 electrons (K-shell) makes the main contribution to the cross section, which in this energy region decreases as $\sigma \sim E^{-5.5}$.

Cross sections for one-electron capture of multiply charged ions on neutral atoms are often estimated using the semi-empirical Schlachter formula [72], obtained on the basis of experimental data:

$$\sigma[\mathrm{cm}^2] = \frac{1.1\times10^{-8}}{\tilde{E}^{4.8}}\,\frac{q^{0.5}}{Z_{\mathrm{T}}^{1.8}}\left[1-\exp\left(-0.037\tilde{E}^{2.2}\right)\right] \times\left[1-\exp\left(-2.44\times10^{-5}\tilde{E}^{2.6}\right)\right], \tag{4.5}$$

$$\tilde{E} = \frac{E}{Z_{\mathrm{T}}^{1.25} q^{0.7}}\,, \quad q \geqslant 3\,, \quad \tilde{E} > 10\,, \tag{4.6}$$

where E is the ion energy in keV/u units. The accuracy of Eqn (4.5) is no less than a factor of 2. Note that semi-empirical formulas (4.5) for electron-capture cross sections and (3.16) for electron-loss cross sections are used to estimate the lifetime of ion beams in accelerator systems [2].

4.2 Target-density effects in electron capture and ionization

The high density of target atoms in a solid (foil) or dense gas significantly affects the probabilities of the processes of interaction of ions with targets and, consequently, the macro-characteristics associated with them: energy losses and equilibrium charges of beams when passing through the medium, equilibrium thicknesses of the target, etc. This is the so-called *target density* (gas-solid) effect, which greatly affects the electron-capture cross sections, decreasing cross sections up to a factor of 10, and less significantly electron-loss cross sections, increasing them by 10–30% (see [1, 71, 73–81]).

In the case of electron capture, the density effect is as follows. As the density of atoms in the medium increases, the frequency of collisions of ions with target atoms increases, so the time between sequential collisions becomes shorter than the lifetime of excited ionic states formed as a result of electron capture, which are actively ionized during subsequent collisions with target atoms. As a result of the process, only those ions survive whose principal quantum numbers n range from the ground state $n = n_0$ to some excited one with the maximum number $n = n_{\max}$, $n_0 \leqslant n \leqslant n_{\max}$, while excited ions with $n > n_{\max}$ are effectively ionized by subsequent collisions with target atoms. A similar effect of 'lowering' the ionization boundary occurs in a dense plasma during the ionization of atoms and ions by electrons [4].

Taking into account the target density effect, the total cross section for one-electron capture

$$\mathrm{X}^{q+} + \mathrm{A} \rightarrow \mathrm{X}^{(q-1)+}(n) + \mathrm{A}^+ \tag{4.7}$$

to all possible states n of the ion $\mathrm{X}^{(q-1)+}$ has the form

$$\sigma_{\mathrm{tot}}^{\mathrm{DE}}(v) = \sum_{n=n_0}^{n_{\max}} \sigma_n(v)\,, \quad n_{\max} = n_0 + \Delta n\,, \tag{4.8}$$

where $\sigma_n(v)$ is the cross section of electron capture to the state with the principal quantum number n, n_0 is the ground state, and $n_{\max}$ is the maximum quantum number $\Delta n = n_{\max} - n_0$. In a rarefied gas, $n_{\max} \rightarrow \infty$, i.e., the $\mathrm{X}^{(q-1)+}(n)$ ions are formed in all possible quantum states. In a dense gas or solid, $n_{\max}$ is limited and determined by the maximum possible value, which depends on the atomic structure of the colliding particles and the energy of the ions. In a superdense medium, electron capture occurs primarily to the ground state, i.e., at $\Delta n = 0$ and $n_{\max} = n_0$. An example of the distribution of electron-capture cross sections over the principal quantum number n of the final state of the ion is presented in Fig. 13.

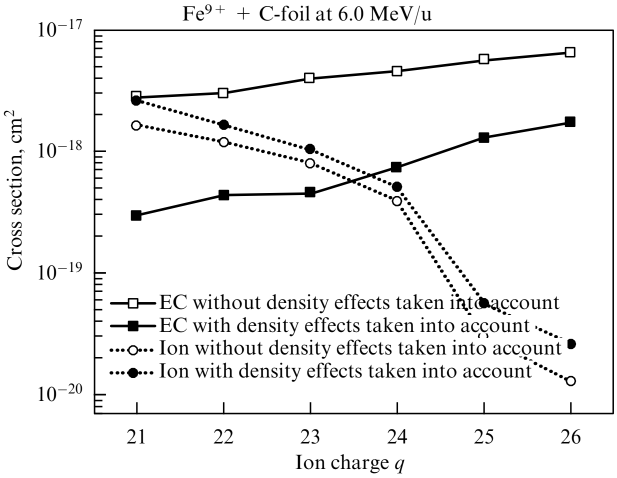

Figure 13. Ionization (ion) and electron capture (EC) cross sections in collisions of Fe^{9+} ions at an energy of 6 MeV/u with graphite foil as a function of charge q — calculation with and without taking into account the target density effect. (From [80].)

To estimate the parameter Δn in (4.8), two alternative formulas are used:

$$\Delta n = q\left(\frac{10^{18}}{Z_{\mathrm{T}}^2 N_{\mathrm{T}}\,[\mathrm{cm}^{-3}]}\right)^{1/7}\left(\frac{E\,[\mathrm{keV/u}]}{250q^2}\right)^{1/14} \tag{4.9}$$

or

$$\Delta n = q\left(\frac{5\times10^{16}}{Z_{\mathrm{T}}^2 N_{\mathrm{T}}\,[\mathrm{cm}^{-3}]}\right)^{1/9}\left(\frac{E\,[\mathrm{keV/u}]}{q^6}\right)^{1/18}, \tag{4.10}$$

where E is the ion energy [keV/u], and N_{T} is the target density [cm^{-3}]. Formula (4.9), which was derived in [71] based on the classical formulas of Thompson and Kramers for ionization cross sections and radiative transition probabilities, corresponds to the *pure* ionization of ions formed as a result of electron capture. Equation (4.10) obtained in [82] describes the maximum number $n_{\max}$ at *step* ionization, when the $[\mathrm{X}^{(q-1)+}]^*$ ion is first excited to an adjacent level and then ionized. Calculations of the cross section showed that Eqn (4.10) usually describes experimental data more accurately than Eqn (4.9) does. Note that estimating the influence of density effects on the cross sections for the electron loss of heavy ions in interactions with neutral atoms is more complicated problem than in the case of electron capture (see [80]).

4.3 Multi-electron capture

Due to the strong Coulomb interaction, the electron capture of multiply charged ions on atoms leads with a high probability to the capture of more than one electron:

$$\mathrm{X}^{q+} + \mathrm{A} \rightarrow \mathrm{X}^{(q-k)+} + \mathrm{A}^{k+}\,, \quad k \geqslant 1\,. \tag{4.11}$$

Multi-electron capture for all charges $k \geqslant 2$ makes a significant contribution (up to 50%) to the total electron-capture cross section and occurs at almost all energies. Multi-electron processes also play an important role in the electron loss of heavy ions in reactions with neutral atoms (Section 3.3).

Experimental data on multi-electron capture cross sections were obtained primarily at low ($E = 0.01$ eV/u–10 keV/u

Table 2. Parameters of approximation (4.12) and (4.13) of experimental cross sections of electron capture involving $k = 1-4$ electrons at energies $E \approx 1$ eV/u–20 keV/u. (From [67].)

k	$C(k)$	$A(k)$	$B(k)$
1	1.43 ± 0.76	1.17 ± 0.09	2.76 ± 0.19
2	1.08 ± 0.95	0.71 ± 0.14	2.80 ± 0.32
3	$(5.50 \pm 5.8) \times 10^{-2}$	2.10 ± 0.24	2.89 ± 0.39
4	$(3.57 \pm 8.9) \times 10^{-4}$	4.20 ± 0.79	3.03 ± 0.86

[83–85]) and medium ($E = 1$–10 MeV/u) energies [36, 37] in collisions of multiply charged ions with gas targets H_2, He, inert gases, and molecules (see also [1–3]). For example, studies [67, 84] present experimental data on the cross sections $\sigma_{q,q-k}$ of processes at very low collision energies $E \approx 1$ eV/u–20 keV/u:

$$X^{q+} + A \to X^{(q-k)+} + A^{k+}, \; 1 \leqslant k \leqslant 4, \; 2 \leqslant q \leqslant 8, \quad (4.12)$$

$$X = \mathrm{Ne}, \mathrm{Ar}, \mathrm{Kr}, \mathrm{Xe},$$

$$A = \mathrm{He}, \mathrm{Ne}, \mathrm{Ar}, \mathrm{Kr}, \mathrm{Xe}, \mathrm{H_2}, \mathrm{N_2}, \mathrm{O_2}, \mathrm{CH_4}, \mathrm{CO_2},$$

which are described with an accuracy of 35% by the semi-empirical formula

$$\sigma_{q,q-k} = 10^{-12}[\mathrm{cm}^2]\, C q^A \left(I_{\mathrm{T}}[\mathrm{eV}]\right)^{-B}, \qquad (4.13)$$

where I_{T} is the ionization potential of the target atom, and A, B, C are the fitting parameters (see Table 2).

The results of studies [67, 83] showed that electron-capture cross sections capturing $k = 1-4$ electrons weakly depend on the energy and chemical element of the ion, but depend primarily on the charge of the ion and the target atom. Figure 14 shows experimental data on the cross sections for multi-electron capture in collisions of Ar^{q+}+Ar and Ar^{q+}+Xe^{q+}+Kr as a function of ion energy.

A large amount of experimental data on the cross sections for one-electron and multi-electron capture and ionization (electron loss) is presented in [36] for heavy ions Xe, Pb, and U with an energy of 1.4 MeV/u in collisions with He, N_2, and Ag. Table 3 shows the experimental cross sections for one- and multi-electron capture of multiply charged lead and uranium ions on argon atoms at MeV/u energies. It can be seen that the total contribution of multi-electron capture to the total cross section is fairly large. Multi-electron processes of ionization and electron capture of heavy and superheavy ions play a significant role in the formation of the average charge of ion beams passing through gas targets (Sections 3.3 and 4.3).

Theoretical calculations of multi-electron capture cross sections were carried out primarily for two-electron capture using the strong coupling method [86], based on the quasi-molecular model [87, 88], and the independent particle

Table 3. Experimental cross sections of electron capture (in units of 10^{-18} cm^2) involving $k = 1-4$ electrons and total cross sections of the collision of xenon, lead, and uranium ions with Ar atoms at energies of 1.4 and 3.5 MeV/u. Relative contribution (%) of the total cross section of multi-electron capture $k \geqslant 2$ to total cross section σ_{tot} is also presented.

Ion	σ_1	σ_2	σ_3	σ_4	σ_{tot}	$\sum \sigma_k/\sigma_{\mathrm{tot}}$, %	Energy, MeV/u	Source
Xe^{27+}	154	38.9	8.06	—	201	23.4	1.4	[38]
Xe^{30+}	165	52.8	14.5	—	232	29.5	—	[38]
Xe^{33+}	209	59.7	22.4	—	291	28.2	—	[38]
Pb^{27+}	115	13	—	—	128	10.2	—	[38]
Pb^{39+}	248	96.7	38.4	—	383	35.3	—	[38]
Pb^{42+}	288	99.1	51.4	—	439	34.3	—	[38]
U^{27+}	95.6	13.2	0.11	—	109	12.2	—	[38]
U^{39+}	224	75.1	25.5	—	324	33.9	—	[38]
U^{42+}	247	81.5	40.8	—	369	33.1	—	[38]
U^{28+}	12.6	—	—	—	—	—	3.5	[39]
U^{39+}	52.3	8.1	0.3	—	60.7	13.8	—	[39]
U^{42+}	61.6	16.1	2.0	—	79.7	22.7	—	[39]
U^{52+}	82.5	35.3	10.6	1.4	130	36.5	—	[39]

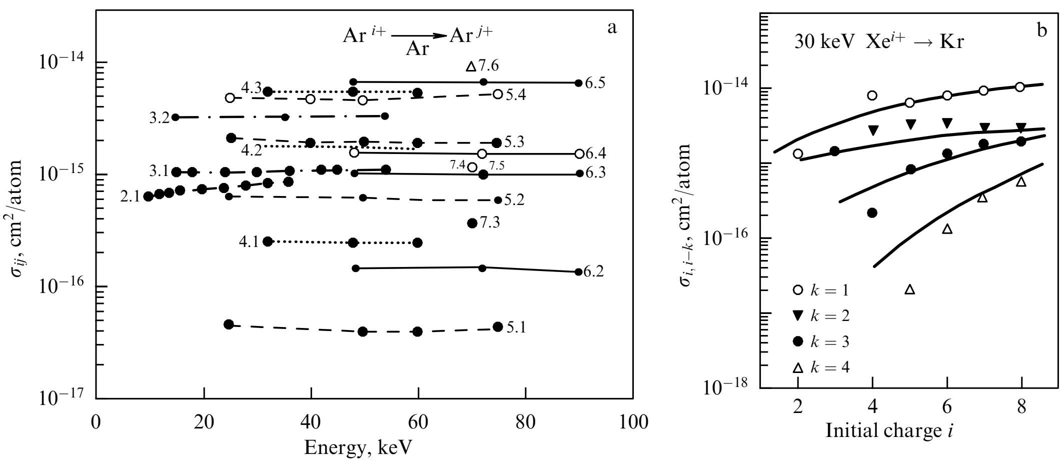

Figure 14. Cross sections for multi-electron capture of multiply charged ions on noble gas atoms at low energies: (a) argon ions on argon atoms as a function of energy and (b) xenon ions on argon atoms at energy $E = 30$ keV as a function of xenon ion charge. Symbols — experimental data; curves — semi-empirical formula (4.13). (From [67].)

method [89] at low and medium collision energies (see review [90]). In general, the properties of multi-electron capture cross sections, i.e., the dependence of cross sections on the atomic structure of colliding particles, the velocity of the incident ion, and other atomic parameters have not been fully studied experimentally or theoretically and require further consideration.

4.4 Electron capture at relativistic energies

At relativistic energies, an additional process of radiative electron capture (REC) occurs, which is accompanied by photon emission:

$$X^{q+} + A \to X^{(q-1)+} + A^+ + \hbar\omega\,. \qquad (4.14)$$

This process is similar to photorecombination,

$$X^{q+} + e \to X^{(q-1)+} + \hbar\omega\,, \qquad (4.15)$$

the difference being that in REC a *bound* electron of the target atom is captured, while in (4.15) a *free* electron is captured. The REC emission spectrum depends on the incident ion energy and the atomic structure of the colliding particles (for more information on REC processes, see review [27]). At high and relativistic energies, electron capture in ion-atomic collisions occurs through two competing channels, radiative (REC) and nonradiative (NRC), so the total cross section is determined by the sum

$$\sigma_{\text{tot}} = \sigma_{\text{NRC}} + \sigma_{\text{REC}}\,. \qquad (4.16)$$

The cross sections of each of the processes have the following asymptotic behavior:

$$\sigma_{\text{NRC}} \sim \frac{q^5 {Z_{\text{T}}}^5}{E^{5.5}}\,, \quad \sigma_{\text{REC}} \sim \frac{q^4 Z_{\text{T}}}{E^2}\,, \qquad (4.17)$$

i.e., the NRC cross section decreases with energy E faster than the REC cross section does, but increases faster with increasing charge of the incident ion q and the atomic number of the target Z_{T}. Therefore, the relative contribution of each process depends on the atomic parameters of the reactions.

Cross sections for electron capture of heavy ions on atoms at high energies were measured in the accelerators BEVALAC, SUPER-EBIT (USA), and LINAC (Germany) (see [1–3, 91–93]). Relativistic NRC cross sections were calculated in the eikonal [94, 95] and the Brinkman–Kramers approximation with normalization based on the CAPTURE program [71]. To calculate the REC cross sections, the Kramers formula [96] and tables of relativistic cross sections [97], in combination with recurrence relations described in [27], are used.

Typically, at relatively low energies, NRC is the dominant process; however, as energy increases, REC processes become dominant. This situation is illustrated in Fig. 15, which shows the cross sections for one-electron capture of uranium ions on argon atoms in a wide energy range. It can be seen that, at energies $E \gtrsim 400$ MeV/u, the REC processes start playing a significant role in the electron capture process.

Figure 16 presents a calculation of the electron-capture cross sections of Xe^{54+} ions on hydrogen molecules per atom at energies of 5.5 and 30.9 MeV/u as a function of the principal quantum number n of the resulting ion. The NRC cross sections calculated in the eikonal approximation and using the CAPTURE program are in good agreement with each other for all values of n. The REC cross sections were calculated in the nonrelativistic approximation taking into account recurrence relations [98].

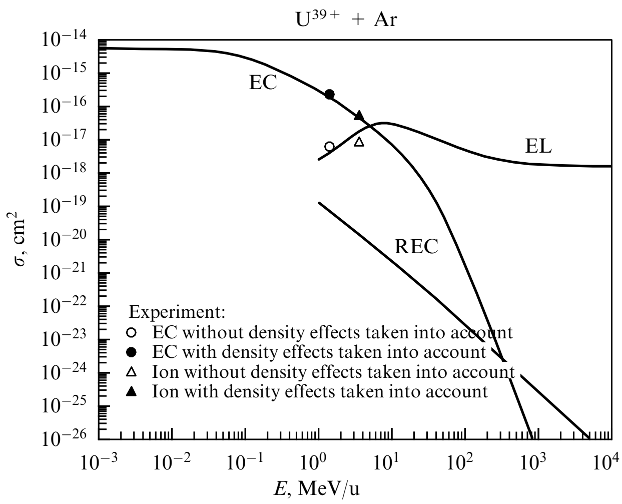

Figure 15. Cross sections for one-electron electron capture and ionization of U^{38+} ions in collisions with argon atoms as a function of ion energy. Symbols show experimental data [36, 37]. EC and EL are the cross sections for one-electron capture and ionization calculated using the CAPTURE and RICODE programs, respectively [34], REC is the Kramers formula [96]. (From [34].)

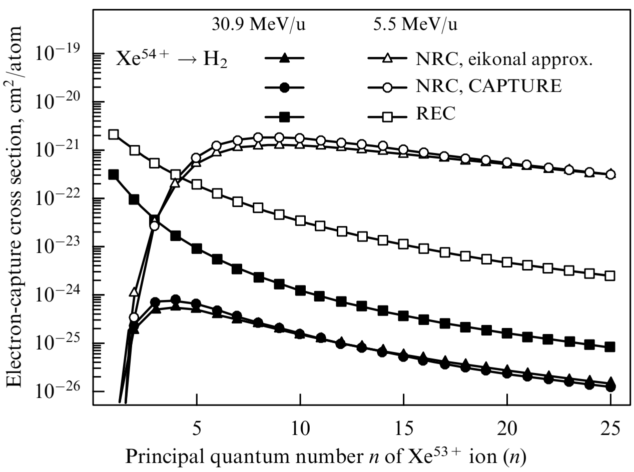

Figure 16. Cross sections for electron capture of Xe^{54+} ions on hydrogen molecules at energies of 5.5 and 30.9 MeV/u as a function of the principal quantum number n of the resulting $Xe^{53+}(n)$ ion. NRC — calculations made in the eikonal approximation using the CAPTURE program, REC — Kramers formula [96]. (From [98].)

The relative contribution of the calculated electron-capture NRC and REC cross sections in collisions of Au^{78+} ions with nickel atoms at relativistic energies is compared with experimental data in Fig. 17. At energies $E < 300$ MeV/u, nonradiative capture prevails; at $E = 400-900$ MeV/u, both processes are of importance, and at $E > 1000$ MeV/u, REC electron capture makes the main contribution to electron capture by a hydrogen molecule.

X-ray spectra arising during REC electron capture are used in X-ray spectroscopy of multiply charged ions to determine radiative transition probabilities, photoionization cross sections, QED effects, and other characteristics [27, 100, 101].

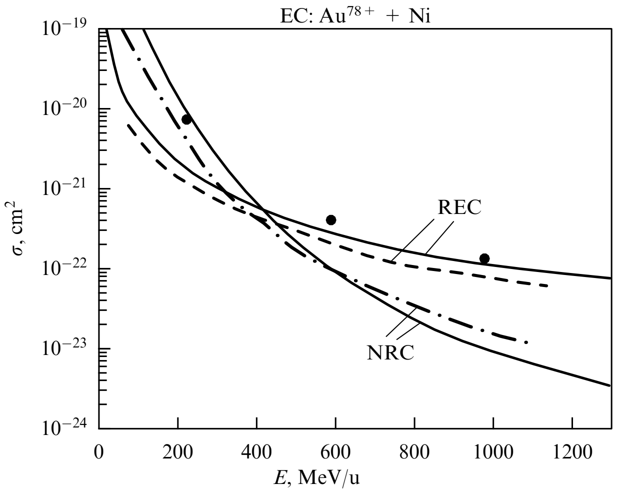

Figure 17. Relativistic electron-capture cross sections NRC and REC of Au^{78+} ions interacting with nickel atoms as a function of ion energy. Circles indicate experimental data [93]. REC: solid and dashed curves — calculation using the CAPTURE program and the eikonal approximation, respectively; NRC: solid and dashed curves — calculation using the Kramers formula and the Stobbe formula [99]. (From [93].)

5. Collisions of ions with molecules

5.1 Bragg's additivity rule

Many physical applications require information on the cross sections for the interaction of ions with *molecules* (electron capture and ionization), for example, to estimate the lifetime of ion beams in a vacuum accelerator system containing primarily the molecules H_2, N_2, H_2O, CO_2, CH_4, etc. For these atomic processes, *Bragg's additivity* rule is used, according to which the cross section for the interaction of an ion with a molecule can be represented as the sum of the cross sections for the interaction with the constituent *atoms* of the molecule,

$$\sigma_{\mathrm{mol}} = \sum_i N_i \sigma_i(Z_i)\,, \tag{5.1}$$

where $\sigma_i(Z_i)$ is the cross section for the interaction of an ion with an atom, Z_i is its atomic number, and N_i is the number of atoms with atomic number Z_i. For example, the cross section for the interaction of an ion with a CH_4 molecule according to Bragg's rule is represented as

$$\sigma(\mathrm{CH_4}) = \sigma(\mathrm{C}) + 4\sigma(\mathrm{H})\,. \tag{5.2}$$

The use of Bragg's rule is associated with difficulties in calculating cross sections for molecular targets, even in the case of the simplest hydrogen molecule H_2 (see, for example, [102]). Bragg's rule is applied in those cases where molecular effects (chemical bonds, polarizability, vibrations, rotation, etc.) can be neglected, i.e., when atoms in a molecule can be considered independent scattering centers. This approximation is realized at high collision energies, when the collision time is short, and the interaction with the molecule can be separated into interactions with the individual atoms of which it consists.

Study [103] experimentally showed that Bragg's rule is well satisfied for the cross sections of total ionization (electron loss) of heavy ions in interactions with diatomic and polyatomic molecules (with the exception of the simplest H_2 molecule) and even for partial (multi-electron) ionization cross sections. Figure 18a shows the total electron-loss cross sections σ_{mol}/N of Xe^{18+} ions as a function of the total number of electrons N_{e} and the average charge of the target molecule $\tilde{Z}$, determined from the equation based on Bragg's rule:

$$\frac{\sigma_{\mathrm{mol}}}{N_{\mathrm{e}}} = \sigma(\tilde{Z})\,, \quad \tilde{Z} = \frac{\sum_i Z_i N_i}{N_{\mathrm{e}}}\,, \tag{5.3}$$

where $\sigma(\tilde{Z})$ is the cross section of ionization by an atom with average atomic number $\tilde{Z}$. The experimental data obtained in this way, with the exception of H_2 and CH_4 molecules, agree with an accuracy of 6% with the values on the straight line plotted using experimental data for atomic targets He and Ne. The ratio of the total cross sections for the electron loss of xenon ions in interactions with hydrogen atoms and molecules, obtained in [103], is $\sigma(\mathrm{H_2})/\sigma(\mathrm{H}) = 3.4$, i.e., is not equal to 2 (as it should be according to Bragg's rule: see Section 5.2). It should be noted that in the general case the average charge $\tilde{Z}$ in Eqn (5.3) is not an integer: for example, for molecules C_3F_8 and SF_6, it is equal to $\tilde{Z}(\mathrm{SiH_4}) = 18/5 = 3.6$ and $\tilde{Z}(\mathrm{SF_6}) = 70/7 = 10.0$, respectively.

Experimental cross sections of k-electron ionization, $k = 1-8$, of Xe^{18+} ions in collisions with N_2, CO, and CO_2 molecules with close average charges $\tilde{Z}$ (7.0, 7.00, and 7.33, respectively) are presented in Fig. 18b in coordinates (5.3). The scaled multi-electron ionization cross sections for these molecules agree well with each other.

5.2 Violation of Bragg's rule for cross sections for one-electron capture of ions on H_2 molecules

Bragg's additivity rule (5.1) is also used to determine the electron-capture cross sections of ions on molecules, where it is partially justified by the fact that at high energies the main contribution to the electron-capture cross section comes from the capture of inner-shell electrons of the target (Section 3.1), the structure of which in atoms and molecules is approximately the same.

Bragg's rule is violated in the case of one-electron capture of ions on H_2 hydrogen molecules, the cross sections of which are required for many applications in plasma physics and accelerator physics to find optimal conditions for electron loss of low-charge ions in gas targets, obtain ion beams with the maximum average charge, etc.

Study [104] used experimental data to establish that the ratio of the cross sections for one-electron capture of multiply charged ions on hydrogen atoms and molecules is not equal to 2, $\sigma(\mathrm{H_2})/\sigma(\mathrm{H}) \neq 2$, and with increasing ion energy it increases nonmonotonically from 0.8 up to 3.8:

$$0.8 \leqslant \frac{\sigma(\mathrm{H_2})}{\sigma(\mathrm{H})} \leqslant 3.8\,, \quad 0.1 \leqslant \frac{E\,[\mathrm{keV/u}]}{q^{4/7}} \leqslant 10^3\,, \tag{5.4}$$

where q is the incident ion charge. A slightly different dependence of the $\sigma(\mathrm{H_2})/\sigma(\mathrm{H})$ ratio was later obtained in [105] using a different law for scaling the ion charge and energy.

The ratio of one-electron capture cross sections $\sigma(\mathrm{H_2})/\sigma(\mathrm{H})$ in coordinates (5.4) is presented in Fig. 19, where the solid curve represents the calculation in the Bohr–Lindhard approximation [107] and the dotted curve is the

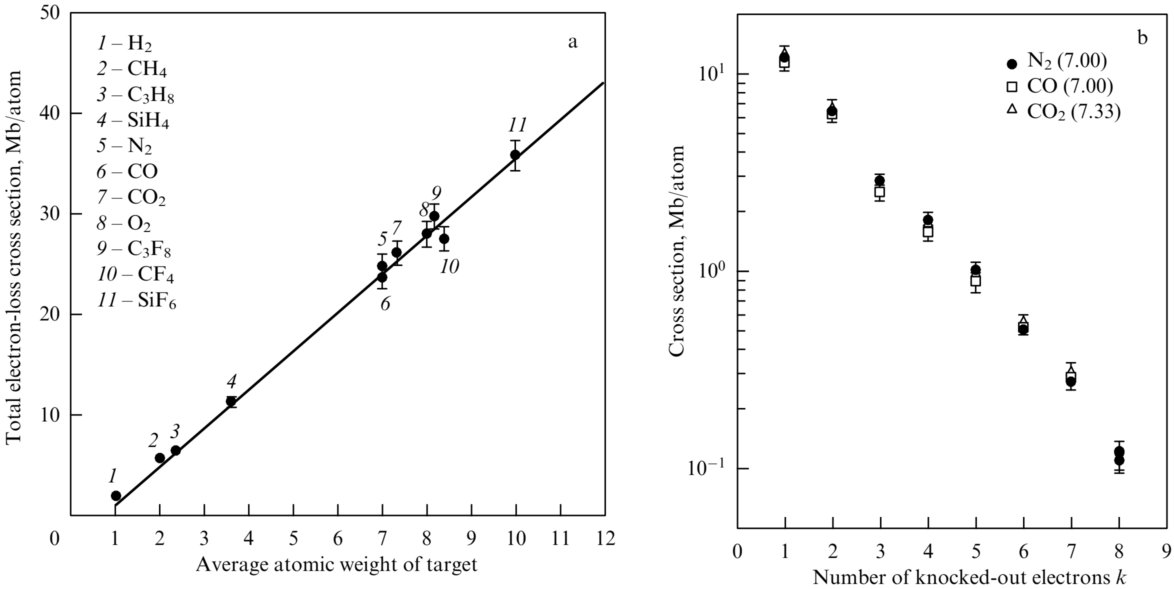

Figure 18. Total cross sections for ionization (electron capture) of Xe^{18+} ions by gas molecules at an energy of 6 eV/u. (a) Total ionization cross sections as a function of the averaged atomic number (5.3): symbols indicate experimental data, solid line is plotted using experimental data for cross sections of ionization of Xe^{18+} ions by atoms from He to Ne. (b) Experimental cross sections for multi-electron ionization, $k = 1-8$, of Xe^{18+} ions by N_2, CO, CO_2 molecules having similar average atomic charges $\tilde{Z}$ (indicated in parentheses). It can be seen that the cross sections are close to each other for all values of knocked-out electrons k. (From [103].)

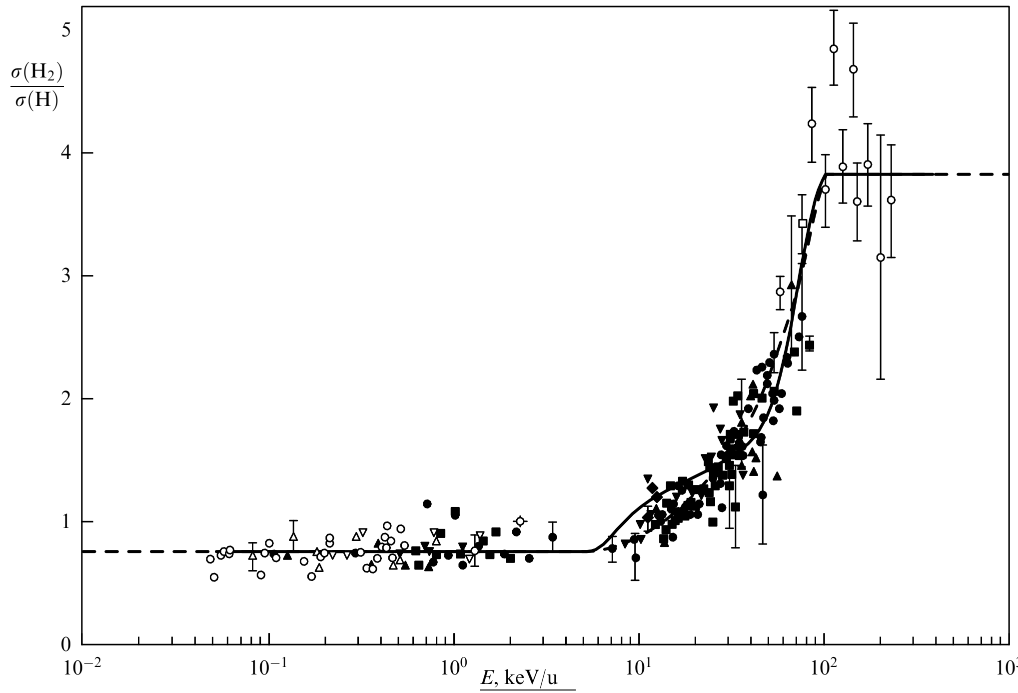

Figure 19. Ratio of one-electron-capture cross sections $\sigma(H_2)/\sigma(H)$ of multiply charged ions in interaction with hydrogen atoms and molecules. Symbols — experiment [106], solid curve — approximation (5.5).

approximation of experimental data:

$$\frac{\sigma(H_2)}{\sigma(H)} = \left\{ \begin{array}{cc} 0.76, & X < 6 \\ 1.76 + 0.0328\,(X - 6), & 6 < X < 100 \\ 3.84, & X > 100, \end{array} \right\},$$

$$X = \frac{E\,[\mathrm{keV/u}]}{q^{4/7}}\,. \qquad (5.5)$$

The ratio of electron capture cross sections $\sigma(H_2)/\sigma(H)$ has been theoretically studied in a number of works (see, for example, [108, 109]); however, a sufficiently complete explanation of the violation of Bragg's rule in the entire energy range is still absent.

5.3 Lifetimes of ion beams in an accelerator. Vacuum conditions

Effective cross sections for the interaction of ions with neutral atoms, accompanied by a change in the charge state of incident ions (ionization, recombination), are the basic data for many problems in atomic, nuclear, and accelerator physics. One of these problems is to determine the lifetime of ion beams in accelerators for planning experiments in which ion beams with high-quality characteristics (small momentum spread, low divergence, etc.) can be created.

The lifetime of an *ion beam* τ in an accelerator is given by the formula

$$I(t) = I_0 \exp\left(-\frac{t}{\tau}\right), \quad (5.6)$$

where $I(t)$ is the time dependence of the beam intensity, and I_0 is its initial value, i.e., τ is determined by the time at which the beam intensity decreases by a factor of e.

In general, the total beam lifetime τ in an accelerator is determined by three main factors as per the formula

$$\frac{1}{\tau_{\mathrm{tot}}} = \frac{1}{\tau_{\mathrm{rg}}} + \frac{1}{\tau_{\mathrm{tg}}} + \frac{1}{\tau_{\mathrm{ec}}}, \quad (5.7)$$

where τ_{rg}, τ_{tg}, and τ_{ec} are the lifetimes associated with the interaction of the ion beam with atoms and molecules of the residual gas in the accelerator, with the gas target, and with free electrons in the process of electron cooling of the beam, respectively.

The quantities τ_{rg} and τ_{tg} are determined by the formula

$$\tau_{\mathrm{rg,\,tg}}\,[\mathrm{s}] = \left[\rho\beta c \sum_T Y_{\mathrm{T}}(\sigma_{\mathrm{EL}} + \sigma_{\mathrm{EC}})\right]^{-1}, \quad \sum_T Y_{\mathrm{T}} = 1, \quad (5.8)$$

where ρ is the gas density in cm^{-3} units, $\beta = v/c$ is the relativistic factor, v is the velocity of ions in the beam, c is the speed of light ($c \approx 3.0 \times 10^{10}$ cm s^{-1}), Y_{T} are gas component fractions, and σ_{EC} and σ_{EL} are total cross sections for electron capture and electron loss [cm^2], i.e., the cross section summed over all multi-electron processes. The summation in (5.8) is carried out over all gas components, and, in the case of molecular targets, Bragg's additivity rule is used (Section 5.1). Thus, the ion beam lifetime in an accelerator depends on the ion energy, the cross sections for the interaction of the beam ions with atomic particles, and *vacuum conditions*, i.e., the pressure and concentration of residual gas atoms and molecules.

Equation (5.8) is used to determine the ion beam lifetime in accelerating facilities (see, for example, [1, 110]). The residual gas components are usually H_2, He, H_2O, O_2, N_2, CO, CO_2, CH_4, Ar, and Xe. Satisfactory results for estimating lifetimes at high energies are provided by semi-empirical formulas for the electron-capture and electron-loss cross sections (see [1]).

5.3.1 Lifetimes of ion beams in an accelerator due to collisions of ions with atoms and molecules of the residual gas. Recently, as part of the Gamma Factory project at CERN, lifetimes τ_{rg} have been measured for beams of multiply charged xenon and lead ions [111]. The goal of the project is to study relativistic heavy-ion beams with energy $E = 26-260$ GeV/u as sources of gamma radiation with wavelengths $\lambda = 1-400$ MeV and radiation fluxes of the order of 10^3 photons per nucleon. The implementation of the Gamma Factory program is based on the principle of laser cooling of a relativistic ion beam. The long lifetimes of Xe^{39+}, Pb^{80+}, and Pb^{81+} ion beams measured at the Super Proton Synchrotron (SPS) and the Large Hadron Collider (LHC) have shown that beams of heavy multiply charged ions can be stored and accelerated to ultra-high energies (see [111]).

Table 4 shows the experimental and theoretical values of the lifetimes τ_{rg} of beams of multiply charged xenon and lead

Table 4. Experimental lifetimes of beams of multiply charged xenon and lead ions obtained at SPS and LHC (CERN) in comparison with theoretical calculations of electron-loss cross sections using the RICODE-M program.

Ion	τ_{rg} exp.	Energy, GeV/u	Accelerator	τ_{rg} theor. [115, 116]
Xe^{39+}	2.550±0.085 s [112]	60	SPS	2.6 s
Pb^{81+}	600 ± 30 s [113]	270	SPS	330 s
Pb^{81+}	∼ 50 h [114]	6.5×10^3	LHC	50 h
Pb^{80+}	350 ± 50 s [113]	270	SPS	160 s
Pb^{79+}	—	270	SPS	70 s
Pb^{71+}	—	270	SPS	10 s
Pb^{69+}	—	270	SPS	7.6 s
Pb^{54+}	—	270	SPS	2.0 s

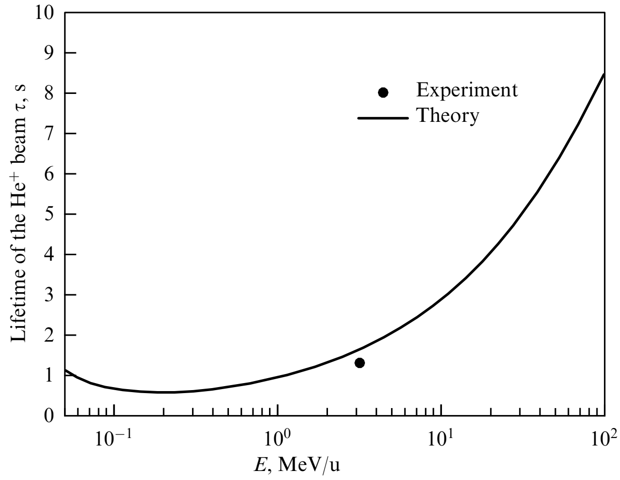

Figure 20. Lifetime of the He^+ ion beam in the NICA Booster as a function of ion energy: dot — experimental value [118], solid curve — calculation based on Eqn (5.8) using the RICODE-M program [35] (this work).

ions under vacuum conditions corresponding to the operation of the SPS and the LHC. The long lifetime of the Pb^{81+} ion beam, $\tau_{\mathrm{rg}} \sim 5$ h, is associated with a higher vacuum in the collider, $P = 4.3 \times 10^{-11}$ mbar, compared to the vacuum in the synchrotron, $P = 2.8 \times 10^{-8}$ mbar. The main components of the residual gas in these systems are molecules of H_2, H_2O, CO_2, CO, and CH_4.

Since 2013, the Joint Institute for Nuclear Research (JINR, Dubna) has been implementing the national project NICA to produce intense beams of heavy ions and polarized nuclei to study new forms of baryonic matter, including quark-gluon plasma [19, 20, 117]. Study [118] reports the results of the first run (December 2020) for commissioning the Booster of the NICA project based on vacuum conditions and measuring the lifetime of a helium He^+ ion beam at an injection energy of 3.2 MeV/u. The measured beam lifetime $\tau_{\mathrm{rg}}(\mathrm{exp.}) = 1.32 \pm 0.06$ s is compared with the theoretical calculation ($\tau_{\mathrm{rg}}(\mathrm{theor.}) = 1.74 \pm 0.50$ s) using the RICODE-M and CAPTURE computer programs. Figure 20 shows the theoretical dependence of the lifetime of an He^+ ion beam on the ion energy in the Booster vacuum. Under these conditions, the He-beam lifetime is determined by ionization of helium ions by atoms and molecules of the residual gas, while electron capture plays virtually no role.

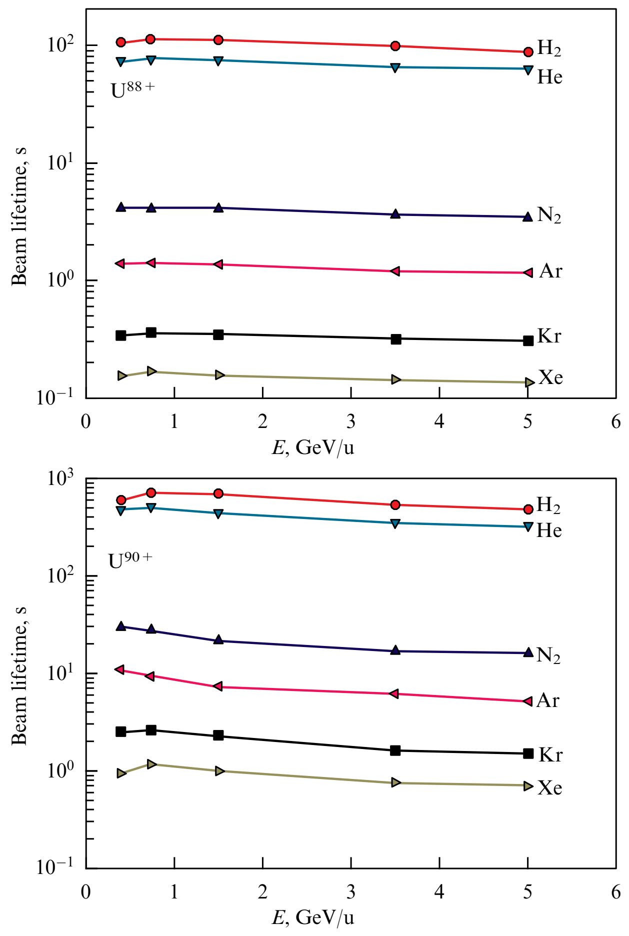

Figure 21. Theoretical lifetimes of U^{88+} and U^{90+} ion beams interacting with gas targets at a pressure of 6.44×10^{-8} mbar. (From [119].)

5.3.2 Lifetimes of ion beams in collisions with gas targets. As part of the FAIR (Facility for Antiproton and Ion Research) project intended to study heavy multiple-charge ions, the GSI Helmholtz Centre (Darmstadt) is constructing the High-Energy Storage Ring (HESR) designed to accumulate and cool beams of multiply charged ions in the energy range $E = 400$ MeV/u–5 GeV/u. In [119], to plan experiments at the HESR, the effective cross sections of electron capture and ionization and lifetimes of beams of multiply charged ions U^{88+}, U^{90+}, U^{92+}, Sn^{49+}, and Sn^{50+} were calculated, and lifetimes related to the interaction of beams with atoms and molecules of the residual gas and gas targets H_2, He, N_2, Ar, Kr, and Xe were estimated.

Figure 21 shows calculated lifetimes τ_{tg} of beams of He-like ions and uranium nuclei colliding with gas targets. For U^{92+} uranium nuclei, the τ_{tg} values are much larger than for He-like U^{90+} ions, since, in the case of bare nuclei, there are no electron ionization processes, and the τ_{tg} values are only determined by electron-capture cross sections, which at these energies are relatively small.

5.3.3 Lifetimes of ion beams when using an electron beam cooling system. The method of cooling beams of heavy charged particles with an electron beam, proposed by G Budker in 1966 [120], is widely used in the world's largest accelerators to reduce the spread in the longitudinal and transverse velocities of the beam ions, i.e., diminish the spread of momentum, diameter, and divergence of the ion beam [8, 12, 121–129].

Table 5. Experimental values of lifetimes τ of ion beams at the Heidelberg-based TSR facility [124].

Ion	Energy, MeV	Pressure, 10^{-11} mbar	τ, s, cooled	τ, s, uncooled
Proton	21	4	220,000 (60 h)	—
HD^+	2	7	—	5
$^7Li^+$	13	6	—	48
$^9Be^+$	7	6	16	16
$^{12}C^{6+}$	73	6	7470	—
$^{28}Si^{14+}$	115	6	540	260
$^{32}S^{16+}$	196	5	450	—
$^{35}Cl^{15+}$	157	6	366	306
$^{35}Cl^{17+}$	202	6	318	366
$^{56}Fe^{22+}$	250	5	77	—
$^{58}Ni^{25+}$	342	5	60	—
$^{63}Cu^{26+}$	510	6	122	—
$^{74}Ge^{28+}$	365	5	45	—
$^{80}Se^{25+}$	480	5	204	—
$^{197}Au^{51+}$	710	5	23	51

When an ion beam is cooled by an electron beam with a longitudinal velocity close to that of the ions, the beam lifetime in the accelerator τ_{ec} is determined by radiative (RR) and dielectronic (DR) recombination of ions during interaction with the electron beam (Sections 6.3 and 6.4). The value of τ_{ec} is determined by the rate of recombination processes and electron beam density N_e:

$$\tau_{ec} = \left[N_e\left(\langle v\sigma\rangle_{RR} + \langle v\sigma\rangle_{DR}\right)\right]^{-1}, \qquad (5.9)$$

where $\langle v\sigma\rangle$ is the process cross section averaged over the anisotropic two-temperature electron velocity distribution function in the beam $F(v, T_\parallel, T_\perp)$.

Table 5 shows experimental values of the ion beam lifetime obtained at the Heidelberg-based Test Storage Ring (TSR) using the electron cooling system (cooled) and without it (uncooled). Recombination of beam ions on cooling beam electrons is especially important in the case of beams of heavy multiply charged ions (for example, Au^{51+}). This is due to the fact that the rates $\langle v\sigma\rangle$ of both processes (RR and DR) depend approximately equally on the ion charge $\langle v\sigma\rangle \sim q^2$; however, the calculation of the values $\langle v\sigma\rangle$ for DR is much more complicated than for RR due to the resonant nature of dielectronic recombination processes.

6. Collisions of ions with electrons

This section discusses the features of the collisions of ions with electrons, leading to a change in the charge of ions: one- and multi-electron ionization and radiative, dielectronic, and ternary recombination. These processes play a significant role in the interaction of ions with electrons in an isolated plasma and during the passage of an ion beam through the plasma.

6.1 One-electron ionization

One-electron ionization of ions by electrons,

$$X^{q+} + e \to \ldots \to X^{(q+1)+} + 2e\,, \tag{6.1}$$

plays an important role in almost all sources of laboratory and astrophysical plasma and in accelerator systems. The ellipsis in reaction (6.1) indicates that intermediate processes are possible, ultimately leading to the formation of one additional electron, i.e., ionization can occur through *direct* and *indirect* (intermediate) processes. Direct processes are associated with the stripping (knockout) of outer and inner electrons of target atoms or ions by an incident electron. Indirect processes include *autoionization* as a result of the Auger process when an inner-shell electron is excited into an autoionization state, and *resonant ionization* associated with the capture of an incident electron and subsequent autoionization of the resulting $X^{(q+1)+}$ ion. Thus, the one-electron ionization cross section of a positive ion consists of three main components:

$$\sigma_{1\text{ion}} = \sigma_{\text{DI}} + \sigma_{\text{EA}} + \sigma_{\text{RI}}\,, \tag{6.2}$$

where the subscripts DI, EA, and RI refer to direct ionization, excitation with autoionization, and resonant ionization, respectively.

6.1.1 Direct ionization. The cross sections and rates of one-electron direct ionization (DI) of positive ions by electrons are often estimated using semi-empirical Lotz formulas [130]:

$$\sigma_{\text{L}} = 2.43N\left(\frac{\text{Ry}}{I_{nl}}\right)^2 \frac{\ln(u+1)}{u+1}\,[\text{cm}^2]\,,$$

$$\langle\sigma_{\text{L}} v\rangle = 6.0\times10^{-8} N\beta^{1/2}\left(\frac{\text{Ry}}{I_{nl}}\right)^{3/2} \exp(-\beta) f(\beta)\,[\text{cm}^3\,\text{s}^{-1}]\,,$$

$$f(\beta) = \exp(\beta)\big|\text{Ei}(-\beta)\big|\,,\ \beta = \frac{I_{nl}}{kT}\,,\ u = \frac{E}{I_{nl}} - 1\,, \tag{6.3}$$

where the function $f(x)$ with integral exponent Ei is approximated with an accuracy of 5% by the formula

$$f(x) = \exp(x)\big|\text{Ei}(-x)\big| \approx \ln\left(1 + \frac{0.562 + 1.4x}{x(1+1.4x)}\right)\,,\quad x > 0\,. \tag{6.4}$$

Here I_{nl} is the binding energy of the nl^{N} electron shells of the X^{q+} ion and T is the electron temperature of the plasma. The accuracy of Lotz's formulas is of the order of the factor 2–3; they were obtained based on calculations in the Born–Coulomb approximation for H-like ions, i.e., ions with one electron.

Studies [3, 131] provide analytical approximations of cross sections and ionization rates with an accuracy of 15% based on numerical calculations of cross sections for multiply charged ions in the Born-Coulomb exchange (BCE) approximation for shells $nl = 1\text{s}, 2\text{s}, \ldots, 6\text{h}$ in the form

$$\sigma_{nl}(u) = p\left(\frac{\text{Ry}}{I_{nl}}\right)^2 \frac{Cu}{(u+1)(u+\varphi)}\,[\pi a_0^2]\,,\ u = \frac{E}{I_{nl}} - 1\,,$$

$$\langle v\sigma_{nl}\rangle(\beta) = p\left(\frac{\text{Ry}}{I_{nl}}\right)^{3/2} \exp(-\beta)\,G(\beta)\,[10^{-8}\ \text{cm}^3\,\text{s}^{-1}]\,,$$

$$G(\beta) = \frac{A\beta}{\beta+\chi}\,,\quad \beta = \frac{I_{nl}}{T}\,,$$

$$0 \leqslant u \leqslant 16\,,\quad 0.125 \leqslant \beta \leqslant 8\,, \tag{6.5}$$

Table 6. Fitting parameters C and φ for cross sections and A and χ for the rates of ionization of multiply charged ions by electron impact from the outer and inner shells nl of a target ion, Eqns (6.5). (From [131].)

nl	C	φ	A	χ
1s	7.96	2.70	5.65	0.40
2s	6.69	2.03	6.23	0.52
2p	6.93	1.47	9.05	0.73
3s	6.00	1.59	7.37	0.70
3p	6.24	1.31	9.11	0.82
3d	6.57	1.08	7.76	1.00
4s	5.77	1.43	9.11	0.76
4p	6.00	1.26	11.7	0.86
4d	6.23	1.11	10.8	0.97
4f	7.06	1.00	13.5	1.07
5s	5.66	1.36	7.96	0.79
5p	5.88	1.23	9.13	0.87
5d	6.08	1.12	10.4	0.96
5f	6.26	1.08	11.1	1.00
5g	6.47	1.04	11.9	1.03
6s	5.60	1.32	8.07	0.80
6p	5.82	1.22	9.13	0.88
6d	6.00	1.13	10.2	0.95
6f	6.24	1.07	11.2	1.00
6g	6.33	1.04	11.7	1.03
6h	6.44	1.01	12.2	1.06

where p is the number of equivalent electrons. The fitting parameters C, φ, A, χ are presented in Table 6.

6.1.2 Excitation with autoionization. In the case of ionization of multi-electron ions, the excitation of inner-shell electrons into autoionization states can make a large contribution to the total ionization cross section due to the nonradiative decay of these states. This ionization channel is called *excitation with ionization*. For example, in the case of ionization of Li-like ions, the excitation of the inner 1s electron to an $n \geqslant 2$ state can lead to ionization:

$$X^{q+}(1\text{s}^2 2\text{s}) + e \to \left[X^{q+}(1\text{s}2\text{s}nl)\right]^{**} + e \to X^{(q+1)+}(1\text{s}^2) + 2e\,,\quad n \geqslant 2\,. \tag{6.6}$$

The double-excited state can decay into the ground state via another channel emitting a photon:

$$\left[X^{q+}(1\text{s}2\text{s}nl)\right]^{**} \to X^{(q+1)+}(1\text{s}^2 2\text{s}) + \hbar\omega\,; \tag{6.7}$$

therefore, the cross section of ionization taking into account excitation/autoinonization has the form

$$\sigma = \sigma_{\text{DI}} + \sum_j B_j\,\sigma_{\text{ex}}^{(j)} \tag{6.8}$$

$$B_j = \sum_{m\leqslant j} A_{jm}^{\text{a}}\left(\sum_{m\leqslant j} A_{jm}^{\text{r}} + \sum_{l\leqslant j} A_{jl}^{\text{a}}\right)^{-1}\,, \tag{6.9}$$

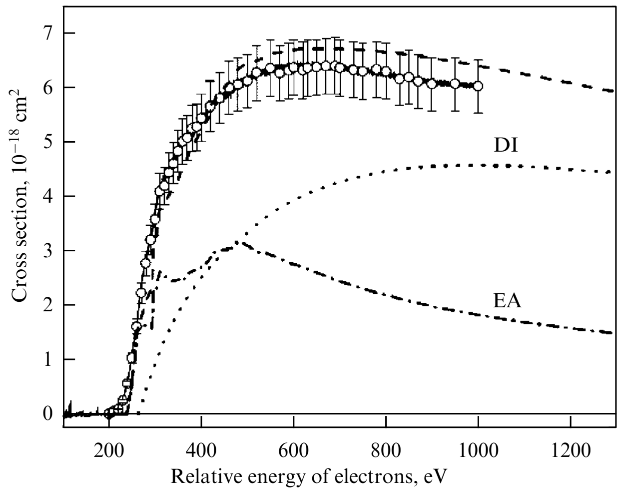

Figure 22. Cross section of one-electron ionization of W^{12+} ions as a function of electron energy. Experiment: solid curve and circles with error bars; theory: DI — direct ionization cross section, EA — excitation with ionization, dashed curve — total cross section. (From [132].)

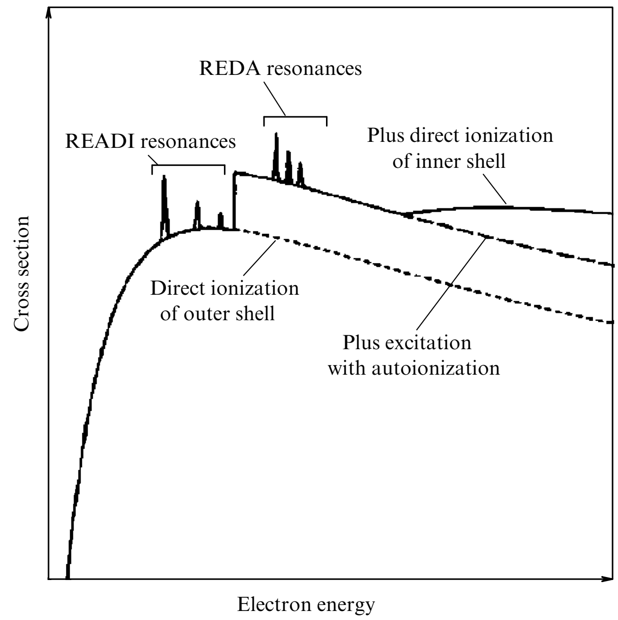

Figure 23. Schematic dependence of the total cross section of ionization by electron impact, taking into account the contribution of various processes leading to ionization. Dashed line — DI, direct ionization of the outer electron shell, dashed line — DI + autoionization EA, resonances — READI and REDA processes, solid curve — total (summed) ionization cross section. (From [138].)

where B_j is the *branching coefficient* of the level j, $A^{\rm a}$ and $A^{\rm r}$ are the probabilities of autoionization and radiative decay, and $\sigma_{\rm ex}^{(j)}$ is the cross section for the excitation of the inner electron into the autoionization state j. The probabilities are usually of the order of $A^{\rm a} \sim 10^{13}-10^{14}$ s^{-1} and weakly depend on the ion charge q, in contrast to the probabilities of radiative transitions, for which $A^{\rm r} \sim q^4$, so that $A^{\rm a} \gg A^{\rm r}$ for ions with charge $q \lesssim 10$. Therefore, for low-charge ions, the branching coefficients $B_j \approx 1$, and

$$\sigma = \sigma_{\rm DI} + \sum_j \sigma_{\rm ex}^{(j)} \,. \tag{6.10}$$

Excitation with autoionization is of special importance for heavy atoms and ions that have unoccupied outer shells and filled inner shells (p^6, d^{10}, f^{14}), since for such systems the excitation cross sections are proportional to the number of equivalent shell electrons. The contribution of excitation/autoionization processes to the total cross section can be large and greatly exceed that of direct ionization processes; however, the calculation of branching coefficients for heavy multiply charged ions is a fairly challenging problem, since it requires taking into account relativistic effects, strong coupling effects, and interaction between configurations.

Figure 22 shows as an example the experimental cross section for ionization of $W^{12+}(Z = 74)$ ions by electrons in comparison with the theoretical calculation. It can be seen that the DI and EA processes make comparable contributions to the total ionization cross section.

6.1.3 Resonant ionization. Resonant ionization is multistage in nature and manifests itself in the form of narrow resonances in the total ionization cross section. Among the resonant ionization processes, the largest contribution to the total cross section is provided by resonant excitation auto double ionization (READI),

$$X^{q+}(1s^2 2s) + e \to \left[X^{(q-1)+}(1s^2 2s 2p 3l)\right]^{**} X^{(q+1)+}(1s^2 2s) + 2e \,, \tag{6.11}$$

and resonant excitation double autoionization (REDA),

$$X^{q+}(1s^2 2s) + e \to \left[X^{(q-1)+}(1s^2 2s 3p 3l)\right]^{**} \to \left[X^{q+}(1s^2 2s 2l')\right]^{*} + e \to X^{(q+1)+}(1s^2 2s) + 2e \,, \tag{6.12}$$

although there are other processes of resonant ionization of ions by electron impact (see [133]).

The READI and REDA processes were predicted theoretically in [134, 135] and confirmed experimentally in [136], while measurements of such complex multi-stage processes only became possible with the advent of new methods for measuring and diagnosing reaction products in crossed beams [137] (for more details, see [133]). The relative contribution of each process to the total ionization cross section depends on the incident ion energy and the atomic structure of the target ion X^{q+}. The main contribution is usually made by the DI and EA processes. The contribution of direct and indirect processes to ionization is presented schematically in Fig. 23.

6.2 Multi-electron ionization of ions by electrons

Multi-electron ionization during a single collision of heavy (multi-electron) atoms and ions with electrons,

$$e + X^{q+} \to e + X^{(q+n)+} + ne \,, \quad n \geqslant 2 \,, \tag{6.13}$$

plays an important role in both basic research and practical applications. For example, during the formation of ionization equilibrium in a nonstationary high-temperature (laser) plasma, such processes are responsible for the high-temperature 'tail' of the ionization distribution, since multiply charged ions do not have sufficient time to be formed by means of conventional one-electron stepwise ionization. The

Table 7. Fitting parameters $a(n)$ and $b(n)$ for cross sections of ionization of $2 \leqslant n \leqslant 10$ electrons (6.14). (From [141, 142].)

n	$a(n)$	$b(n)$
2	14.0	1.08
3	6.30	1.20
4	0.50	1.73
5	0.14	1.85
6	0.049	1.96
7	0.021	2.00
8	0.0096	2.00
9	0.0049	2.00
10	0.0027	2.00

contribution of multi-electron ionization to the total cross section can reach 30–50%; therefore, such processes should be taken into account along with one-electron ionization.

Currently, quantum mechanical calculations of multi-electron ionization cross sections are virtually unavailable, even for two-electron ionization of He atoms and He-like ions; therefore, for applications, semi-empirical formulas are usually employed [139–148].

In [141, 142], based on an analysis of experimental data for atoms and ions ranging from He to U, electron energies from the threshold to $E = 100$ keV sufficient for the removal of $n = 2-13$ electrons and under the assumption of a Bethe–Born behavior of cross sections, a semi-empirical formula was derived:

$$\sigma_n\,[\mathrm{cm}^2] = 10^{-18}\,\frac{a(n)N^{b(n)}}{(I_n/\mathrm{Ry})^2}\left(\frac{u+1}{u}\right)^c\frac{\ln u}{u}\,,\quad u = \frac{E}{I_n} - 1 \geqslant 0\,, \tag{6.14}$$

where E is the incident ion energy and a, b, and c are fitting constants. For neutral atoms, $c = 1.0$, for ions, $c = 0.75$, and $I_n = \sum_k I_k$ is the *threshold energy* of n-electron ionization equal to the sum of the ion ionization potentials. For example, for ternary-electron ionization, the threshold ionization value I_3 is equal to the sum of the first, second, and third ionization potentials of the original atom (ion).

The fitting parameters $a(n)$ and $b(n)$ in Eqn (6.14) for the ionization of $2 \leqslant n \leqslant 10$ electrons are presented in Table 7, and for $n > 10$ they are approximated in the form [141, 142]

$$a(n) \approx 1350n^{-5.7}\,,\quad b(n) = \mathrm{const} = 2.00\,,\quad n > 10\,. \tag{6.15}$$

Cross section (6.14) reaches its maximum at $u_{\max} \approx 3.2$, i.e.,

$$\sigma_{\max}\,[\mathrm{cm}^2] \approx 2.7\times10^{-19}\,\frac{a(n)N^{b(n)}}{(I_n/\mathrm{Ry})^2}\,,\quad E_{\max} \approx 4.2I_n\,. \tag{6.16}$$

The accuracy of Eqn (6.14), which is similar to Lotz's formula (6.3) for the one-electron ionization cross section, is of the order of the factor 2–3. As an example, Figs 24 and 25 show the multi-electron ionization cross sections of the Kr atom and the Rb^+ ion compared with those that follow from Eqn (6.14).

The multi-electron ionization rate with cross sections (6.14) for the Maxwell electron velocity distribution has the

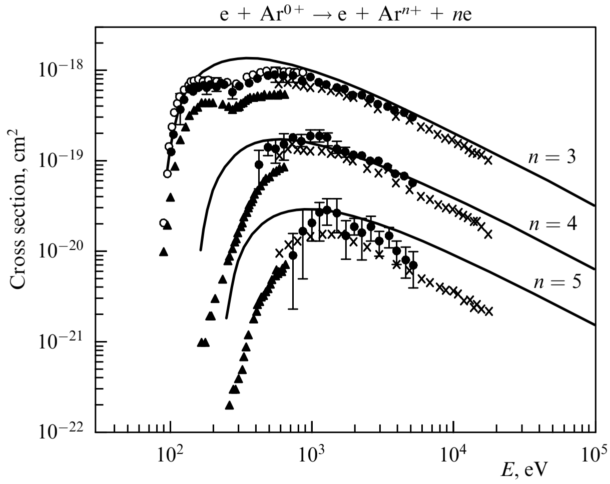

Figure 24. Cross sections of the ionization of $n = 3-5$ electrons of argon atoms as a function of electron energy. Symbols — experiment, solid curves — Eqn (6.14). (From [145].)

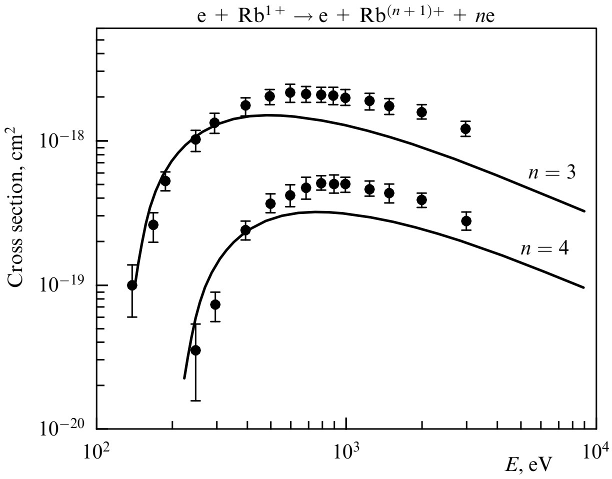

Figure 25. Cross sections of the ionization of $n = 3$ and 4 electrons of Rb^+ ions as a function of electron energy. Symbols — experiment, solid curves — Eqn (6.14). (From [145].)

form [144]

$$\langle v\sigma\rangle[\mathrm{cm}^3\,\mathrm{s}^{-1}] = 2.5\times10^{-10}\,a(n)N^{b(n)}\left(\frac{\mathrm{Ry}}{I_n}\right)^{3/2}\times\exp(-\beta)F(\beta)\,,\quad \beta = \frac{I_n}{kT}\,, \tag{6.17}$$

$$F(\beta) = \beta^{3/2}\int_0^\infty\left(\frac{u}{u+1}\right)^c\exp(-\beta u)\ln(u+1)\,\mathrm{d}u \approx \beta^{1/2}\,\frac{\ln(1+0.5/\beta)}{1+0.25\beta}\,, \tag{6.18}$$

where k is Boltzmann constant.

The universal function $\exp(-\beta)\,F(\beta)$ is plotted in Fig. 26.

The multi-electron ionization rate (6.17) is maximum at $\beta \approx 0.07$:

$$\langle v\sigma\rangle_{\max}[\mathrm{cm}^3\,\mathrm{s}^{-1}] \approx 1.24\times10^{-10}\,a(n)N^{b(n)}\left(\frac{\mathrm{Ry}}{I_n}\right)^{3/2}. \tag{6.19}$$

At $\beta = 1.0$, i.e., $kT = I_n$, we obtain

$$\langle v\sigma\rangle[\mathrm{cm}^3\,\mathrm{s}^{-1}] \approx 3.0\times10^{-11}\,a(n)N^{b(n)}\left(\frac{\mathrm{Ry}}{I_n}\right)^{3/2}. \tag{6.20}$$

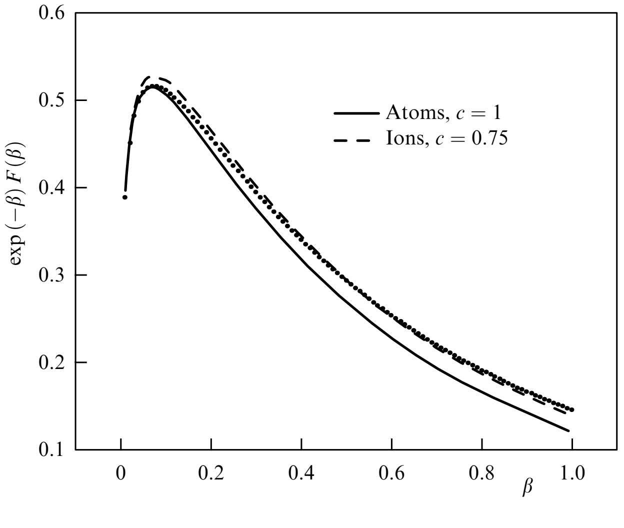

Figure 26. Plot of universal function $\exp(-\beta)\,F(\beta)$ from Eqn (6.17) vs parameter $\beta = I_n/kT$. Solid curve: $c = 1$ for atoms, dashed curve $c = 0.75$ for ions, dotted curve: Eqn (6.18).

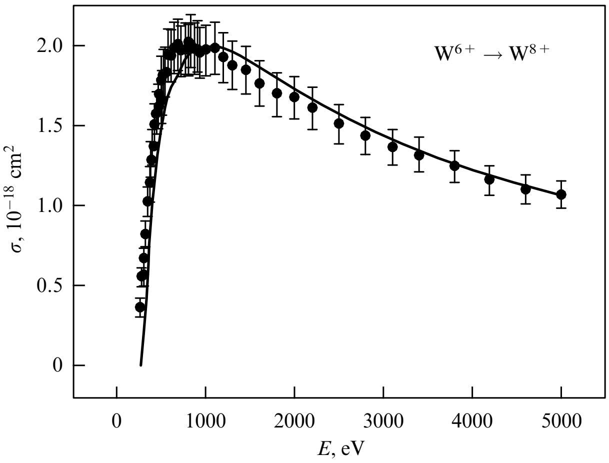

Figure 27. Cross sections for double ionization of W^{6+} ions as a function of electron energy. Symbols — experiment [148], solid curve — Eqn (6.21). (From [147].)

Equations (6.14)–(6.19) can be used to solve problems in plasma kinetics and the interaction of electron and ion beams with plasma.

6.2.1 Two-electron ionization of heavy ions. Processes of one- and two-electron ionization of heavy multi-electron ions by electron impact make the main contribution to the total ionization cross section.

Equation (6.14) describes multiple ionization cross sections *as a whole*, i.e., without taking into account subtle effects associated with the influence of autoionization processes. Semi-empirical formulas for *double* ($n = 2$) ionization cross sections $\sigma_2(E)$ that are more accurate than Eqn (6.14) were also derived based on experimental data: for light ions (from He to Ar) in [146], and for heavy ions (from Ti, $Z = 22$ to Bi, $Z = 83$) in [147].

In the case of double ionization of heavy ions, the formula for $\sigma_2(E)$ has the form

$$\sigma_2(E)\ [\mathrm{cm}^2] = 10^{-13}\left[\Big(1 - \exp\big(-3(u-1)\big)\Big)\frac{A}{I_2^3}\,\frac{u-1}{(u+5)^2}\right.$$
$$\times\big(1 + 0.1\ln(4u+1)\big) + \sum_{\gamma}\frac{B_\gamma}{I_\gamma^2}\,\frac{x-1}{x(x+5.0)}$$
$$\left.\times\left(1 + \frac{0.3}{n}\ln(4x+1)\right)\right], \tag{6.21}$$

$$u = \frac{E}{I_2} \geqslant 1\,, \quad x = \frac{E}{I_\gamma} \geqslant 1\,, \tag{6.22}$$

where E is the incident electron energy, I_2 is the threshold energy of two-electron ionization, I_γ is the binding energy of inner electrons, and A and B_γ are fitting parameters; the sum over γ is the sum over inner shells of the ion. The first term in Eqn (6.21) with the constant A describes the contribution of autoionization processes, while the sum over γ is the summation of the direct ionization cross sections over the inner shells of the target ion. Unlike Eqn (6.14), the accuracy of formula (6.21) for double ionization is higher and amounts to 20–30% (see Fig. 27).

6.3 Radiative recombination

Radiative recombination (RR) or photorecombination is a process inverse to photoionization, which consists of the capture of a free electron by an ion and emission of a photon:

$$X^{(q+1)+} + e \to X^{q+} + \hbar\omega\,, \quad \omega = E_e + E(nl)\,,$$
$$E(nl) > 0\,, \tag{6.23}$$

where E_e is the kinetic energy of the captured electron, and $E(nl)$ is the energy of the ion produced in a state with the principal and orbital quantum numbers *nl*. RR processes (6.23) play an important role in the charge balance of multiply charged ions in electron-ion beam experiments, in processes occurring in laboratory and astrophysical plasmas, when using an electron cooling system (ECS) for ion beams, etc. [120, 121, 126, 127, 149].

The effective RR cross sections, averaged over orbital quantum numbers l, are calculated using the classical Kramers formula [96]:

$$\sigma_{RR}(n, E_e)\ [\mathrm{cm}^2] = 2.105\times10^{-22}\,\frac{Z_{\mathrm{eff}}^4\mathrm{Ry}^2}{n^3 E_e(E_e + Z_{\mathrm{eff}}^2\,\mathrm{Ry}/n^2)}\,, \tag{6.24}$$

where Ry = 13.606 eV, and Z_{eff} is the effective charge of the produced X^{q+} ion.

The Rydberg formula is often used for Z_{eff}:

$$Z_{\mathrm{eff}} = n_0\sqrt{\frac{I_P}{\mathrm{Ry}}}\,, \tag{6.25}$$

where I_P and n_0 are the ionization potential and the principal quantum number of the X^{q+} ion in the ground state.

For convenience, the dependence of Z_{eff} on the ion charge q can be represented in the form of analytical approximations. For example, for multiply charged ions of uranium, gold, lead, and bismuth, these dependences have the form

$$U^{q+},\ Z_n = 92:\ Z_{\mathrm{eff}}(q) = 9.0 + 1.15q^{0.960}\,,\ q > 6\,, \tag{6.26}$$

$$Bi^{q+},\ Z_n = 83:\ Z_{\mathrm{eff}}(q) = 5.0 + 1.15q^{0.966}\,,\ q > 20\,, \tag{6.27}$$

$$Pb^{q+},\ Z_n = 82:\ Z_{\mathrm{eff}}(q) = 4.8 + 1.15q^{0.966}\,,\ q > 20\,, \tag{6.28}$$

$$Au^{q+},\ Z_n = 79:\ Z_{\mathrm{eff}}(q) = 5.0 + 1.30q^{0.938}\,,\ q > 4\,. \tag{6.29}$$

The accuracy of Eqns (6.26)–(6.29) is within 10–15%; they were derived using ionization potentials I_P from study [45] for uranium ions and from [150] for gold, lead, and bismuth ions. It is worth mentioning that, for H-like ions, Eqns (6.26)–(6.29) yield values of Z_{eff} that differ from the nucleus charge Z_n. For example, for the U^{91+} ion, according to (6.26), $Z_{\mathrm{eff}} = 96.4$, while nuclear charge $Z_n = 92$. This difference is associated with taking into account the influence of relativistic corrections on the potentials I_P in [45, 150], which are not taken into account in simple Rydberg formula (6.25); however, the use of the formula for calculating the cross sections of many processes (radiative recombination, radiative electron capture, etc.) usually yields satisfactory results.

The cross section for radiative recombination summed up over all states n has the form

$$\sigma_{\mathrm{RR}}^{\mathrm{tot}}(n_0, E_e) = \left(1 - \frac{p}{2n_0^2}\right)\sigma_{\mathrm{RR}}(n_0, E_e) + \sum_{n>n_0}^{n_{\mathrm{cut}}} \sigma_{\mathrm{RR}}(n, E_e)\,, \tag{6.30}$$

where p is the number of equivalent electrons in the n_0^p configuration of the X^{q+} ion in the ground state, and n_{cut} is the maximum value of the principal quantum number n determined by experimental conditions (high density of plasma electrons, electric field, etc.). For example, in the case of electron cooling of an ion beam (Section 5.3.3), the electric field of electrons determines the value n_{cut} according to the formula [151]

$$n_{\mathrm{cut}} \approx \left(6.2 \times 10^8\, \frac{Z_{\mathrm{eff}}^3}{\mathcal{E}}\right)^{1/4}, \tag{6.31}$$

where $\mathcal{E}$ is the electric field strength [V cm^{-1}].

In the electron cooling of an ion beam, a major role is played by the recombination rates $\langle v\sigma\rangle_{\mathrm{RR}}$, i.e., the cross section of the process averaged over the anisotropic two-temperature electron-velocity distribution function in the beam $F(v, T_\parallel, T_\perp)$, which has the form [123]

$$F(v, T_\parallel, T_\perp) = \frac{m_e}{2\pi k T_\perp}\left(\frac{m_e}{2\pi k T_\parallel}\right)^{1/2} \times \exp\left(-\frac{m_e v_e^2}{2kT_\perp} - \frac{m_e(v_e - v_{\mathrm{rel}})^2}{2kT_\parallel}\right), \tag{6.32}$$

and, consequently, the process rate is determined as

$$\begin{aligned}\langle v\sigma\rangle &= \int_0^\infty v\sigma(v)\, F(v, T_\parallel, T_\perp)\, \mathrm{d}^3 v \\ &= \frac{m_e}{kT_\perp}\left(\frac{m_e}{2\pi k T_\parallel}\right)^{1/2} \int_0^\infty v\sigma(v)\, v^2\, \mathrm{d}v \int_0^\pi \sin\theta\, \mathrm{d}\theta \\ &\quad \times \exp\left(-\frac{m_e v^2}{2kT_\perp}\sin^2\theta - \frac{m_e}{2kT_\parallel}(v\cos\theta - \Delta)^2\right),\end{aligned} \tag{6.33}$$

$$v_{e\perp} = v\sin\theta\,, \quad v_{e\parallel} = v\cos\theta\,, \quad v_{\mathrm{rel}} = \Delta = |v_{e\parallel} - v_{i\parallel}|\,,$$

$$E_{\mathrm{rel}}\,[\mathrm{a.u.}] = \frac{m_e \Delta^2}{2}\,, \tag{6.34}$$

where m_e is the mass of the electron, k is the Boltzmann constant, $v_{e\parallel}, v_{i\parallel}$ is the component of the longitudinal velocity of electrons and ions in the laboratory system, respectively, $v_{e\perp}$ is the component of the electron velocity in the direction perpendicular to the beam, $T_\parallel$ and $T_\perp$ are the temperatures characterizing the distribution of relative velocities of electrons and ions in the longitudinal and transverse directions, respectively, and E_{rel} is the kinetic energy of the electron in the center-of-mass system of the ion beam. Typically, $kT_\parallel \sim 0.1$ meV and $kT_\perp \sim 10$ meV, i.e., $T_\parallel \ll T_\perp$, so the distribution $F(v, T_\parallel, T_\perp)$ is referred to as 'flattened.'

In practice, Eqn (6.33) is used to estimate the lifetime of heavy ion beams due to electron cooling at $E_{\mathrm{rel}} \to 0$; however, a comparison of a large number of experimental data for recombination rates α showed that in most cases the experimental values are much greater than the RR rates, and the main contribution in this area is made by dielectronic recombination, accounting for which in theoretical analysis is a very challenging problem. Figure 28 shows as an example the experimental rate of recombination of Au^{20+} ions on cooling-beam electrons as a function of the relative energy of the electron in comparison with the theoretical value multiplied by a factor of 40.

A comparison of theoretical calculations of recombination rates with experiment showed that, at low values of the relative electron energy E_{rel}, the difference between the experimental $\alpha_{\exp}$ and theoretical α_{RR} rates of RR processes in hydrogen-like ions increases greatly with increasing ion charge Z [129]:

$$\Delta\alpha = \alpha_{\exp} - \alpha_{\mathrm{RR}} \sim (T_\parallel T_\perp)^{-1/2} Z^{2.8}\,, \tag{6.35}$$

where $T_\parallel$ and $T_\perp$ are the longitudinal and transverse temperatures of the electron distribution in the cooling beam. A slightly different dependence of Z on $\Delta\alpha$ was obtained in [122]:

$$\Delta\alpha = \alpha_{\exp} - \alpha_{\mathrm{RR}} \sim (T_\parallel T_\perp)^{-1/2} Z^{2.6}\,. \tag{6.36}$$

Note that both scaling laws $Z^{2.8}$ and $Z^{2.6}$ exceed the quadratic dependence of Z^2 for the RR rate. Figure 29 shows the dependence of the scaled value $\Delta\alpha(T_\parallel T_\perp)^{1/2}$ on the nuclear charge Z for H-like ions from He^{2+} to U^{92+}. It can be seen that, with an increase in Z in the range $Z = 2-92$, the value of $\Delta\alpha$ increases by five orders of magnitude.

6.4 Dielectronic recombination: ions in plasma and in an incident beam

Dielectronic recombination (DR), a process of interaction of an ion with a free electron (2.10),

$$X^{q+} + e^- \to \left[X^{(q-1)+}\right]^{**} \to X^{(q-1)+}(nl) + \hbar\omega\,, \tag{6.37}$$

is a two-step process in which a free electron is first captured, and an inner-shell electron of the ion is simultaneously excited into a doubly excited state, which then decays into the *nl* state with the emission of a photon. DR processes do not occur at all values but only at certain values of the free electron energy that satisfy the resonance condition:

$$E_e \approx \Delta E - \frac{q^2\mathrm{Ry}}{n^2} < \Delta E\,, \quad \Delta E > 0\,, \tag{6.38}$$

where ΔE is the excitation energy in the $X^{(q-1)+}$ ion. Due to the resonance condition, the DR cross section does not depend on the electron velocity in a continuous way, as is the case in other atomic processes, but is characterized by a structure of *resonances* with a certain width at energies set by Eqn (6.38) (for more details, see [3]).

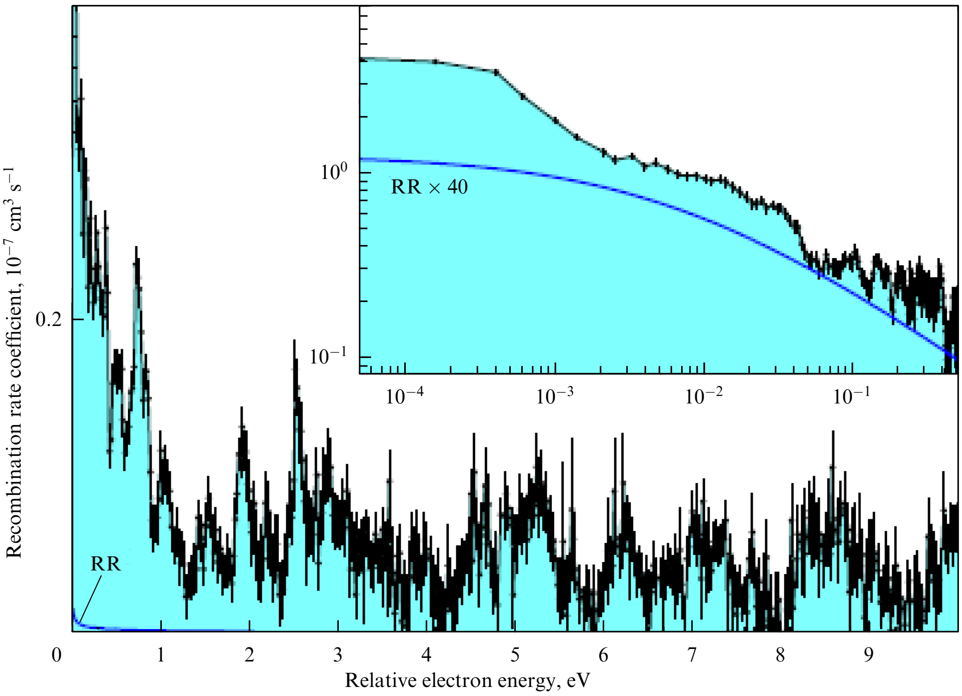

Figure 28. Experimental rate of the recombination of Au^{20+} ions on cooling beam electrons as a function of relative energy: solid smooth curve — theoretical RR rate multiplied by a factor of 40, maxima and minima — total experimental recombination rate associated with dielectronic recombination. (From [128].)

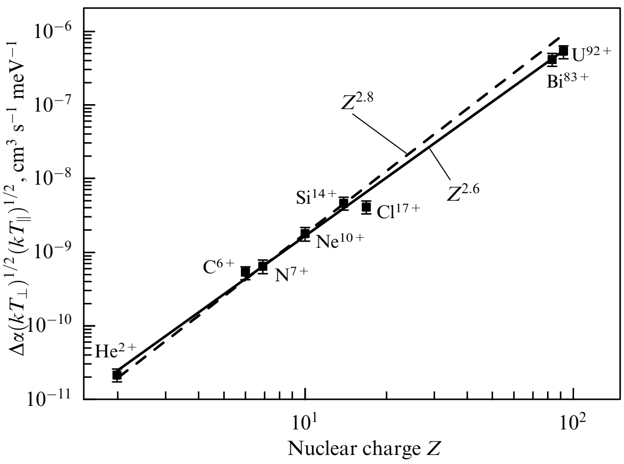

Figure 29. Dependence of scaled value $\Delta\alpha(T_\parallel T_\perp)^{1/2}$ on nuclear charge in the case of recombination of H-like ions at $E_{\rm rel} \to 0$: symbols correspond to experimental data for ions from He^{2+} to U^{92+}, dashed curve is scaling according to Eqn (6.35), solid curve is Eqn (6.36). (From 122].)

The intermediate state is formed in two stages: a free electron is captured into the *nl* state by an ion with charge q in the initial state i, and excess energy is transferred to the bound electron of the ion, which is excited, forming an ion $[{\rm X}^{(q-1)+}]^{**}$ in the intermediate state. We consider process (6.37) in more detail and present its first capture stage in the form

$$ {\rm X}^{q+}(i) + {\rm e} \to \left[{\rm X}^{(q-1)+}(j = i^* nl)\right]^{**}, $$

where $j = i^* nl$ is an autoionization doubly excited state, which decays via two channels: *radiative*,

$$ \left[{\rm X}^{(q-1)+}(j = i^* nl)\right]^{**} \to {\rm X}^{(q-1)+}(h = i^* n'l', inl, i^{*\prime} n'l') + \hbar\omega\,, \tag{6.39} $$

to states h that change the *nl* state of a captured electron or the state of an excited electron — a transition to the initial state i or to an excited state $i^{*\prime}$ lying below the excited state i^*; and *autoionization*,

$$ \left[{\rm X}^{(q-1)+}(j = i^* nl)\right]^{**} \to {\rm X}^{q+}(m = i, i^{*\prime} i' nl)\,, \tag{6.40} $$

into states m with *autoionization* of a captured electron *nl* or a valence electron in the initial state if the inner-shell electron is excited; the i' state corresponds to the initial state without a valence electron. The states f among the states h in (6.39) that are stable with respect to autoionization are considered to be a result of *dielectronic* recombination (for DR processes, see, for example, [123,152]).

The total coefficient of the rate of a DR-ion in the initial state i, which is located in a plasma with electron temperature $T_{\rm e}$ and Maxwell electron energy distribution, has the form [152]

$$ \alpha_{\rm d}^{\rm tot}(i) = \left(\frac{4\pi a_0^2 I_{\rm H}}{kT_{\rm e}}\right)^{3/2} \sum_{i_{\rm lev}} \frac{1}{2g_{i_{\rm lev}}} \sum_j g_j\, Q_{\rm d}(j, i_{\rm lev}) \exp\left(\frac{-E_s(j)}{kT_{\rm e}}\right), \tag{6.41} $$

$$ Q_{\rm d}(j, i_{lev}) = \frac{\sum_f A_{\rm r}(i \to f) A_{\rm a}(j \to i_{lev})}{\sum_h A_{\rm r}(j \to h) + \sum_m A_{\rm a}(j \to m)}\,. \tag{6.42} $$

Here, a_0 and $I_{\rm H}$ are the Bohr radius and the ionization energy of the hydrogen atom, respectively, k is the Boltzmann constant, and the coefficient $(4\pi a_0^2 I_{\rm H}/k)^{3/2} = 4.14 \times 10^{-16}$ cm^3 K$^{3/2}$ (K is the Kelvin).

In Eqn (6.42), $A_{\rm r}$ and $A_{\rm a}$ are the probability of radiative and autoionization transitions, respectively. The first summation in Eqn (6.41) is carried out over the levels $i_{\rm lev}$ of the initial state i in the coupling scheme used in the calculations; $g_{i_{\rm lev}}$ and g_j are the statistical weight of the levels of the initial state and the intermediate doubly excited state $j = i^* nl$, respectively;

and $E_s(j)$ is the excitation energy of the autoionization state j relative to the level $i_{\rm lev}$.

Study [153] examined the DR process that occurs when a *beam* of fast heavy ions passes through a cold plasma. Under these conditions, the total coefficient of the rate of the DR-ion in the initial state i, which moves at velocity $v_{\rm p}$ through a plasma with electron temperature $T_{\rm e}$, is equal to

$$\alpha_{\rm d}^{\rm tot}(i) = \left(\frac{4\pi a_0^2 I_{\rm H}}{kT_{\rm e}}\right)^{3/2} \sum_{i_{\rm lev}} \frac{1}{2g_{i_{\rm lev}}} \sum_j g_j\, Q_{\rm d}(j, i_{\rm lev}) F(s,t)\,, \tag{6.43}$$

where $Q_{\rm d}(j, i_{\rm lev})$ is defined by Eqn (6.41), and $F(s,t)$ is the shifted Maxwell distribution function (Section 8):

$$F(s,t) = \frac{\exp\left[-(s-t)^2\right] - \exp\left[-(s+t)^2\right]}{4st}\,,$$
$$s = \left(\frac{E_s(j)}{kT_{\rm e}}\right)^{1/2}, \quad t = \left(\frac{mv_{\rm p}^2}{2kT_{\rm e}}\right)^{1/2}. \tag{6.44}$$

If the contribution of doubly excited states $j = i^*nl$ should be taken into account up to large values of the principal quantum number of the captured plasma electron $n = n_{\max}$, the total DR rate coefficient is calculated using the following approximation:

$$\alpha_{\rm d}^{\rm tot}(i) = \alpha_{\rm d}(i, n_{\rm cut}) + \sum_{n_{\rm ext}=n_{\rm cut}+1}^{n_{\max}} \alpha_{\rm d}^{\rm ext}(i, n_{\rm ext})\,, \tag{6.45}$$

where $\alpha_{\rm d}(i, n_{\rm cut})$ is defined by Eqn (6.43) with the sum over states j with the principal quantum number of the captured electron $n \leqslant n_{\rm cut}$. To estimate the contribution of j-states with $n \leqslant n_{\rm cut}$, employed are the data which are calculated for $n = n_{\rm cut}$ and the following scaling laws: $1/n^3$ for autoionization rates $A_{\rm a}(n_{\rm ext})$ and probabilities of radiative transitions $A_{\rm r}(n_{\rm ext})$ for transitions $i^*nl - i^*n'l'$, $A_{\rm r}(n) = A_{\rm r}(n_{\rm cut})$ for radiative transitions $i^*nl - inl$, $i^*nl - i^{*\prime}nl$, and

$$E_s^{\rm ext}\big(j(n_{\rm ext})\big) = E_s^{\rm ext}\big(j(n_{\rm cut})\big) - q_{\rm scr}^2\left(\frac{1}{2}n_{\rm ext}^2 - \frac{1}{2}n_{\rm cut}^2\right) \tag{6.46}$$

for excitation energy, where $q_{\rm scr} = Z - N$ is the screened charge of the ion, Z is the nucleus charge, and N is the number of electrons in the original ion in the i state. The probabilities of emission and autoionization in Eqn (6.42) and s in Eqn (6.44) have the form

$$A_{\rm r}^{\rm ext}\big(j(n_{\rm ext}) \to h\big) = \left(\frac{n_{\rm cut}}{n_{\rm ext}}\right)^3 \sum_{h,\, n' \leqslant n_{\rm cut}} A_{\rm r}\big(j(n_{\rm cut}l) \to h(n'l')\big) + \sum_{h,\, n \leqslant n_{\rm cut}} A_{\rm r}\big(j(n_{\rm cut}l) \to h(nl)\big)\,, \tag{6.47}$$

$$A_{\rm r}^{\rm ext}\big(j(n_{\rm ext}) \to i_{\rm lev}\big) = \left(\frac{n_{\rm cut}}{n_{\rm ext}}\right)^3 \sum_{i_{\rm lev}} g_{j(n_{\rm cut})} A_{\rm a}\big(j(n_{\rm cut}) \to i_{\rm lev}\big)\,, \tag{6.48}$$

$$A_{\rm a}^{\rm ext}\big(j(n_{\rm ext}) \to m\big) = \left(\frac{n_{\rm cut}}{n_{\rm ext}}\right)^3 \sum_m A_{\rm a}\big(j(n_{\rm cut}) \to m\big)\,, \tag{6.49}$$

$$s^{\rm ext} = \left(\frac{E_s\big(j(n_{\rm ext})\big)}{kT_{\rm e}}\right)^{1/2}. \tag{6.50}$$

Finally, the expression for $\alpha_{\rm d}^{\rm ext}(n_{\rm ext})$ in Eqn (6.45) can be represented as

$$\alpha_{\rm d}^{\rm ext}(i, n_{\rm ext}) = \left(\frac{4\pi a_0^2 I_{\rm H}}{kT_{\rm e}}\right)^{3/2} \sum_{i_{\rm lev}} \frac{1}{2g_{i_{\rm lev}}} \times \sum_{j(n_{\rm cut})} \frac{A_{\rm r}^{\rm ext}\big(j(n_{\rm ext}) \to f\big) A_{\rm a}^{\rm ext}\big(j(n_{\rm ext}) \to i\big)}{A_{\rm r}^{\rm ext}\big(j(n_{\rm ext}) \to h\big) + A_{\rm a}^{\rm ext}\big(j(n_{\rm ext}) \to m\big)} \times F(s^{\rm ext}, t)\,. \tag{6.51}$$

6.5 Ternary recombination

Ternary recombination (TR) of ions on electrons,

$$X^{q+} + e^- + e^- \to X^{(q-1)+} + e^-\,, \tag{6.52}$$

which is a process inverse to ionization process (6.1), plays an important role in plasma processes at low temperatures and high densities of plasma electrons.

The recombination cross section $\sigma_{\rm TR}$ has a dimension cm^4 s^{-1}, unusual for cross sections, and the TR rate, unlike other processes, is not linear in the electron density $N_{\rm e}$, but is proportional to its square:

$$\kappa_{\rm TR} = N_{\rm e}^2 \iint v_1 v_2\, F(E_1) F(E_2)\, \sigma_{\rm TR}(E)\, {\rm d}E_1\, {\rm d}E_2\, [{\rm s}^{-1}]\,, \tag{6.53}$$

where $F(E)$ are the velocity distribution functions of two incident electron beams, usually Maxwell functions.

In an isolated plasma, the TR rate has the form

$$\kappa_{\rm TR} = C \times 10^{-27}\, [{\rm s}^{-1}]\, q^3 N_{\rm e}^2\, [{\rm cm}^{-3}] T_{\rm e}^{-9/2}\, [{\rm eV}]\,, \tag{6.54}$$

where $T_{\rm e}$ is the electron temperature of the plasma, and the constant $C = 8.75$ in the classical approximation [154] and $C = 5.5$ in the quantum approach [4]. Equation (6.54) shows that TR processes are of importance at low temperatures and high plasma densities.

In the case an *ion beam* interacting with plasma, the TR rate is determined in the classical approximation by the formula [155]

$$\kappa_{\rm TR} = 2.92 \times 10^{-31} [{\rm s}^{-1}] q^3 N_{\rm e}^2\, [{\rm cm}^{-3}]\, v_{\rm r}^{-9} [{\rm a.u.}]\,, \tag{6.55}$$

$$v_{\rm r} = \sqrt{v_{\rm P}^2 + v_{\rm th}^2}\,, \quad v_{\rm th} = \sqrt{\frac{8kT_{\rm e}}{\pi m}}\,, \tag{6.56}$$

where $v_{\rm r}$ is the relative velocity in atomic units, 1 a.u.$= 2.2 \times 10^8$ cm s^{-1}, $v_{\rm P}$ is the velocity of ions in the beam, $v_{\rm th}$ is the average (thermal) velocity of electrons in the plasma, and k is the Boltzmann constant. At $v_{\rm P} \ll v_{\rm th}$, Eqn (6.55) transforms into (6.54) with a constant $C = 12.3$, close to the classical one in approximation [154].

A comparison of the rates of radiative and ternary recombination yields the following estimate [156]:

$$\frac{\kappa_{\rm RR}}{\kappa_{\rm TR}} \approx 1.6 \times 10^{17}\, \frac{q v_{\rm r}^6\, [{\rm a.u.}]}{N_{\rm e}\, [{\rm cm}^{-3}]}\,, \tag{6.57}$$

from which it follows that the ternary recombination rate is small and becomes comparable to the radiative recombination rate only at very high plasma densities $N_{\rm e}$. The rates of ionization and recombination of various atomic processes in the interaction of ion beams with plasma are compared in Section 8.3.

7. Interaction of heavy ion beams with media

7.1 Ionic fractions. Balance equations

The interaction of an ion beam with a medium (gas, liquid, solid, plasma) leads to the formation of *ion fractions* $F_q(x)$ with various charges q as a function of penetration depth x (target thickness). Each fraction $F_q(x)$ characterizes the probability of the formation of an ion with a charge q at a distance x from the entrance to the target. The dynamics of the fractions depend on competing atomic processes accompanied by a change in the charge state, i.e., ionization and recombination of incident ions by particles of the medium: atoms, molecules, ions, and electrons.

Information about the dynamics of ionic fractions in the process of interaction with matter plays an important role in many areas of physics and applications: atomic physics, the study of radiative and collisional processes involving multiply charged ions (emission spectra, QED effects, cross sections of ion-atomic collisions), the stopping power of matter, plasma physics (beam diagnostics of plasma density and temperature based on energy and charge losses of the incoming beam of heavy ions), nuclear physics (detection of heavy and superheavy elements, creation of beams of bare nuclei of heavy ions), accelerator physics (vacuum conditions, lifetimes of ion beams in an accelerating system), proton and ion therapy for tumors, the production of new composite materials and electronic microcircuits using ion implantation, etc. [1–3, 8, 9, 157, 158].

The dependence of ion fractions on the target thickness has an important feature: at thickness values x much greater than the mean free path L of ions in the medium, $x \gg L$, fractions $F_q(x)$ no longer depend on x and reach the so-called *equilibrium regime*, in which equilibrium is established between the number of ionization and recombination events; in this case, the ion fractions and the thickness of the target are called *equilibrium* (Section 7.3). Another important feature of equilibrium fractions is their independence from the initial charge of ions q_0 in the incident beam, i.e., the values of the equilibrium fractions are the same for all ion charges from a neutral atom to a bare nucleus: $0 \leqslant q_0 \leqslant Z_{\mathrm{n}}$, where Z_{n} is the nucleus charge. In the equilibrium regime, the ions 'forget' about the charge of the ions q_0 in the incident beam.

The dynamics of ionic fractions in a medium are studied using differential equations of *balance* that relate fractions $F_q(x)$ to effective cross sections σ for recombination and ionization of ions in the medium. In the case of a gas or solid target (foil), the balance equations have the form [159]

$$\frac{\mathrm{d}}{\mathrm{d}x} F_q(x) = \sum_{q' \neq q} F_{q'}(x)\sigma_{q'q} - F_q(x) \sum_{q' \neq q} \sigma_{qq'} \tag{7.1}$$

$$\sum_q F_q(x) = 1\,, \quad 0 \leqslant q \leqslant Z_{\mathrm{n}} \tag{7.2}$$

with initial conditions at $x = 0$:

$$\sum_q F_q(x = 0) = 1\,, \tag{7.3}$$

where σ_{ij} are the cross sections for ionization and recombination, including multi-electron processes, and the sum over q means the summation over all possible charge states $0 \leqslant q_0 \leqslant Z_{\mathrm{n}}$.

The dimension of the penetration depth or *surface* density x is [atom cm^{-2}]. It is assumed that in the system of equations (7.1)–(7.3) the effective cross sections σ do not vary with changes in the parameter x, i.e., the energy losses of ions after passing through a layer of thickness x are ignored. The sum of fractions is normalized to unity as a consequence of the law of conservation of the number of ions before and after collision with the medium.

In the case of a *plasma* target, the coefficients in balance equations are not effective cross sections, but process rates, since plasma consists of atomic particles (electrons, atoms, ions, molecules, molecular ions), the densities of which depend on the electron temperature and density of plasma. The balance equations for plasma targets have the form

$$\frac{\mathrm{d}}{\mathrm{d}t} F_q(x) = \sum_{q' \neq q} F_{q'}(x)\,\alpha_{q'q} - F_q(x) \sum_{q' \neq q} \alpha_{qq'}\,, \tag{7.4}$$

$$\sum_q F_q(x) = 1\,, \quad x = v_{\mathrm{P}} t\,, \quad 0 \leqslant q \leqslant Z_{\mathrm{P}}\,, \tag{7.5}$$

where $\alpha_i = N_i \langle v\sigma_i \rangle$ are the rates of ionization and recombination for *each* type of plasma particle per unit time t. Equations (7.4) and (7.5) take into account interaction of ions with all plasma particles: radiative and dielectronic recombination, ternary recombination, electron impact ionization, etc., which are usually absent in the case of gas and solid targets (regarding atomic processes in the interaction of ion beams with plasma, see, for example, [2, 153, 156, 160, 161]).

The surface density of the target x is related to other characteristics by the formula

$$x\,[\text{atom cm}^{-2}] = N\,[\text{atom cm}^{-3}]\,L\,[\text{cm}] = x\,[\text{g cm}^{-2}]\,\frac{N_{\mathrm{A}}}{M}\,, \tag{7.6}$$

where N is the conventional density of the target, L is the target thickness, M is the atomic mass of particles of the medium in a.m.u. (atomic mass unit), and $N_{\mathrm{A}} = 6.022 \times 10^{23}$ is Avogadro's number. For carbon, $M(\mathrm{C}) = 12$ a.m.u.; for hydrogen molecules, $M(\mathrm{H_2}) = 2$ a.m.u.

An analytical solution to the system of equations (7.4) and (7.5) for the case of three fractions is presented in [46]. This case is of interest, for example, for the collision of a relativistic ion beam with foils, when the main fractions are fractions of H- and He-like ions and incident ion nuclei. In the general case, the system of differential equations (7.4) and (7.5) is solved using the Runge–Kutta the method or by diagonalization of the interaction matrix (Section 7.4).

7.2 Equilibrium fractions and average charge of an ion beam upon interaction with a medium

The *average* charge of the beam $\bar{q}(x)$ depends on the target thickness x and is determined by the expression

$$\bar{q}(x) = \sum_q qF_q(x)\,. \tag{7.7}$$

At $x \to \infty$, the average charge of the ion beam is equal to the *equilibrium* charge, which does not depend on the target thickness:

$$\bar{q} = \sum_q qF_q(\infty)\,, \quad \sum_q F_q(\infty) = 1\,, \quad x \to \infty\,, \tag{7.8}$$

where $F_q(\infty)$ are the equilibrium fractions that are the solution to the system of differential equations (7.1) and (7.2) at $\mathrm{d}F_q/\mathrm{d}x = 0$, which transforms into a system of linear *algebraic* equations:

$$0=\sum_{q'\neq q} F_{q'}(\infty)\sigma_{q'q} - F_q(\infty)\sum_{q'\neq q}\sigma_{qq'}\,,\quad \sum_q F_q(\infty)=1\,. \quad (7.9)$$

The equilibrium fractions $F_q(\infty)$ depend on the cross sections of the interaction of ions with target particles, but do not depend on the initial charge of the incident ion q_0 (see [10, 107, 160] and Section 7.2), i.e., when a beam of neutral atoms or bare nuclei passes through the target, the values of the equilibrium fractions $F_q(\infty)$ are the same. The target thickness $X_{\rm eq}$ at which the ion fractions become equilibrium is referred to as the *equilibrium thickness*, which, unlike equilibrium fractions, depends on the charge of the incident ion q_0.

In the case of beams of heavy multi-electron ions, a large number of equilibrium fractions are formed, the distribution of which over q features a wide spectrum. In the case of ions with several electrons, this distribution has a narrower profile, i.e., only a few fractions dominate, as is the case, for example, of relativistic collisions of an ion beam with a target.

The distribution of equilibrium functions $F_q(\infty)$ over the charge q at the target exit is described by a symmetric Gaussian function, which can become asymmetric due to various physical mechanisms: the effect of target density in gases and foils (Section 4.2), the influence of dielectronic recombination in plasma [153,156], relativistic effects, etc. The Gaussian distribution of equilibrium fractions is described by the following parameters:

distribution *width*

$$d=\left[\sum_q (q-\bar{q})^2 F_q(\infty)\right]^{1/2} \quad (7.10)$$

and the *asymmetry parameter*

$$s=\sum_q \frac{(q-\bar{q})^3 F_q(\infty)}{d^3}\,. \quad (7.11)$$

The average beam charge $\bar{q}(x)$ is usually maximum in the equilibrium regime, i.e., when

$$F_q(x\to\infty)=F_q(\infty)\,,\quad \bar{q}(x\to\infty)=\langle q\rangle\,; \quad (7.12)$$

however, nonequilibrium fractions for particular charges may significantly exceed equilibrium fractions, i.e., $F_q(x)\geqslant F_q(\infty)$ (see, for example, [13, 162]).

The system of equations (7.1) and (7.2) has a simple *analytical* solution if we take into account only one-electron cross sections, $|q-q'|=1$, i.e., if we ignore multi-electron processes. In this case, the equilibrium fractions are determined through the ratio of one-electron-loss cross sections to electron-capture cross sections [46, 160]. Thus, if n fractions are taken into account, the solution to system (7.1) and (7.2) takes the form

$$F_1(\infty)=\left[1+\frac{\sigma_{12}}{\sigma_{21}}\left(1+\frac{\sigma_{23}}{\sigma_{32}}\left(1+\frac{\sigma_{34}}{\sigma_{43}}\left(1+\ldots\frac{\sigma_{n-2,n-1}}{\sigma_{n-1,n-2}}\right.\right.\right.\right.$$
$$\left.\left.\left.\left.\times\left(1+\frac{\sigma_{n-1,n}}{\sigma_{n,n-1}}\right)\right)\right)\ldots\right)\right]^{-1},$$

$$F_{i+1}(\infty)=F_i(\infty)\,\frac{\sigma_{i,i+1}}{\sigma_{i+1,i}}\,,\quad 1\leqslant i\leqslant n-2\,,$$

$$F_n(\infty)=1-\sum_{i=1}^{n-1}F_i(\infty)\,. \quad (7.13)$$

In the case of a four-charge model, the equilibrium fractions are

$$F_1(\infty)=\frac{1}{1+\sigma_{12}/\sigma_{21}\left(1+\sigma_{23}/\sigma_{32}\left(1+\sigma_{34}/\sigma_{43}\right)\right)}\,,$$

$$F_2(\infty)=F_1(\infty)\frac{\sigma_{12}}{\sigma_{21}}\,,$$

$$F_3(\infty)=F_2(\infty)\frac{\sigma_{23}}{\sigma_{32}}\,,$$

$$F_4(\infty)=1-\left[F_1(\infty)+F_2(\infty)+F_3(\infty)\right]. \quad (7.14)$$

7.3 Equilibrium target thickness

Each fraction $F_q(x)$ attains its equilibrium value $F_q(\infty)$ at its own equilibrium thickness $X_{\rm eq}(q)$, and the variance of values $X_{\rm eq}(q)$ for various charges q can be quite significant. The *equilibrium* thickness of the target is the thickness at which all fractions attain an equilibrium state. The equilibrium thicknesses $X_{\rm eq}(q)$ depend on the rate of interaction processes and on the initial charge of the ion beam q_0, while the equilibrium fractions $F_q(\infty)$ do not depend on the charge q_0 [10]. In numerical calculations, the equilibrium thickness is determined by the condition under which the relative deviation of each fraction $F_q(x)$ relative to the equilibrium solution $F_q(\infty)$ is close to zero. For example, in the BREIT program [160], each equilibrium thickness $X_{\rm eq}(q)$ is defined as

$$x=X_{\rm eq}(q)\,,\ \text{if}\ \frac{|F_q(x)-F_q(\infty)|}{F_q(\infty)}\leqslant\epsilon\,, \quad (7.15)$$

where x is the depth of beam penetration into the target, and parameter $\epsilon=10^{-3}$ can be altered in the BREIT input file.

The dependence of the equilibrium thickness $X_{\rm eq}(q)$ on the initial charge q_0 was studied theoretically in [13, 162, 163] using the BREIT program [160] for heavy ion beams passing through foils, gas targets, and plasma. It has been established that if the initial charge q_0 is close to the equilibrium average $\bar{q}$ (7.8), i.e., if $q_0\approx\bar{q}$, the $X_{\rm eq}(q, q_0\approx\bar{q})$ values are significantly less than $X_{\rm eq}(q, q_0)$ with $q_0\ll\bar{q}$ or $q_0\gg\bar{q}$. This behavior is explained as follows: when the initial charge q_0 is close to the equilibrium average charge, the ion beam comes to equilibrium faster than at $q_0\neq\bar{q}$ and, consequently, features a smaller equilibrium thickness.

Figure 30 presents the calculation of the equilibrium thicknesses $X_{\rm eq}$ as a function of the initial ion charge q_0 (Fig. a, c) and the equilibrium fractions $F_q(\infty)$ as a function of the final charge q (Fig. b, d) in the collision of uranium ions with a Be foil at energy $E=100$ MeV/u and H_2 gas at $E=1.4$ MeV/u, respectively. It can be seen that the equilibrium thicknesses exhibit a deep minimum at $q_0\approx\bar{q}$, i.e., $q_0=89$, $\bar{q}\approx 89.4$ for the Be foil and $q_0=27$, $\bar{q}\approx 26.4$ for an H_2 gas target.

In practice, it is often necessary to determine the *average* equilibrium thickness of the target $\bar{X}$, which characterizes the interaction of ion beams with the target on average. In [46, 164, 165], semi-empirical formulas expressed in terms of ionization and recombination cross sections are used to estimate the average equilibrium thickness $\bar{X}$. In study [161], it was proposed to define the value $\bar{X}$ as the arithmetic mean of the partial thicknesses $X_{\rm eq}(q)$:

$$\bar{X}=\frac{\sum_{q=q_{\min}}^{q_{\max}} X_{\rm eq}(q)}{q_{\max}-q_{\min}+1}\,, \quad (7.16)$$

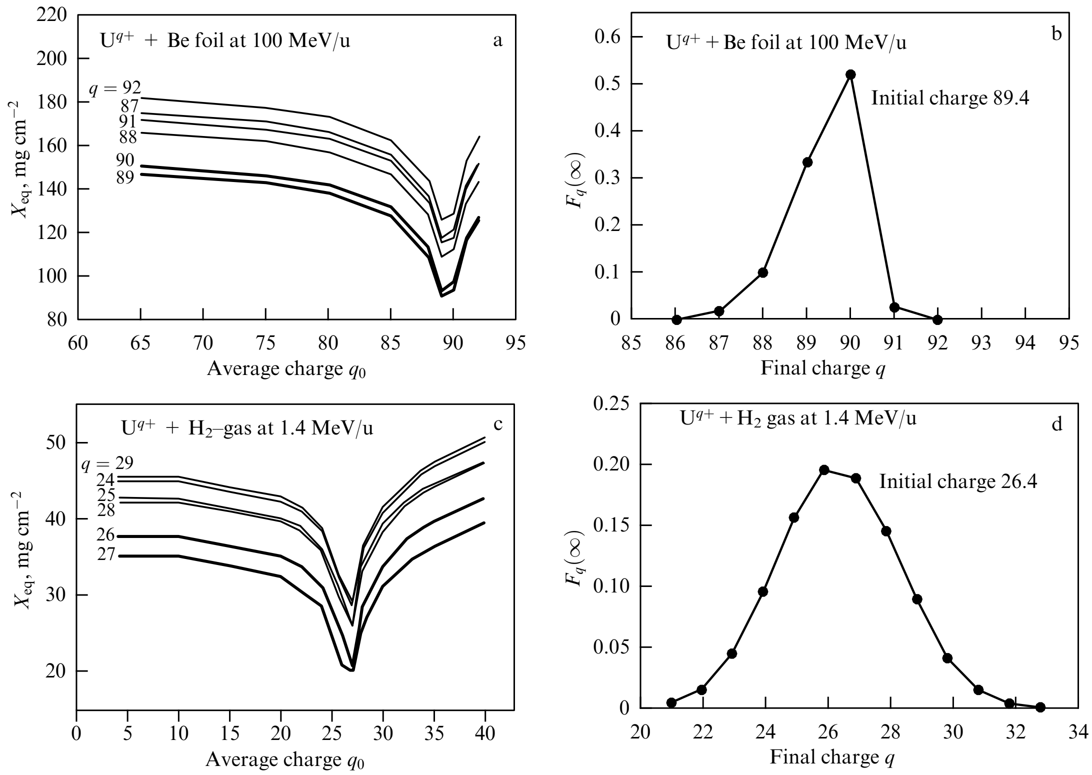

Figure 30. (a) Dependences of equilibrium thicknesses X_{eq} on initial charge q_0 and (b) equilibrium fractions $F_q(\infty)$ on final charge q in collisions of uranium ions with a Be foil at energy $E = 100$ MeV/u and H_2 gas at $E = 1.4$ MeV/u, respectively. Curves with $q = 89, 90$ and $q = 26, 27$ plotted in Fig. a, c correspond to fractions with charges close to equilibrium $\bar{q}$ (Figs b, d). (From [162].)

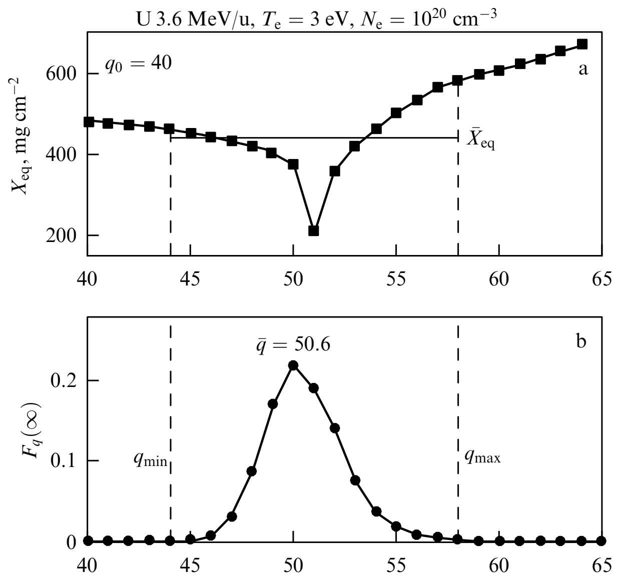

Figure 31. Determination of average equilibrium thickness $\bar{X}$ of a target when U^{40+} ions with an energy of 3.6 MeV/u pass through a hydrogen plasma with electron temperature $T_e = 3$ eV and density $N_e = 10^{20}$ cm^{-3}. Distributions of equilibrium thicknesses $X_{eq}(q)$ and equilibrium fractions $F_q(\infty)$ over the final charge of uranium ions are shown in Figs a and b, respectively. Straight line represents average equilibrium thickness $\bar{X} \approx 440$ mg cm^{-2} that follows from Eqn (7.16).

where q_{min} and q_{max} are the minimum and maximum charges of those equilibrium fractions $F_q(\infty)$ that make the main contribution to the equilibrium charge $\bar{q}$.

Figure 31 presents calculated equilibrium thicknesses $X_{eq}(q)$ and equilibrium fractions $F_q(\infty)$ as functions of the final charge q of U^{40+} ions with an energy of 3.6 MeV/u interacting with hydrogen plasma. The distribution of $X_{eq}(q)$ over q is fairly wide, for example, $X_{eq}(q) = 480$, 212, and 670 mg cm^{-2} for $q = 40$, 51, and 64, respectively. As can be seen from Fig. 31b, the main contribution to the average charge $\bar{q} = 50.6$ comes from the equilibrium fractions $F_q(\infty)$ with $44 \leqslant q \leqslant 58$, for which the average thickness is $\bar{X} \approx 440$ mg cm^{-2}, in accordance with Eqn (7.16). The average equilibrium thickness determined in this way can be used for any type of target (gas, foil, or plasma).

7.4 Computer programs for calculating charge fractions of ions. BREIT program

Currently, five main computer programs are used to study the dynamics of ion beams in media and to calculate the average beam charge and the equilibrium thickness of the target: ETACHA, GLOBAL, CHARGE, MS, and BREIT. A detailed description of the programs is presented in the original works (see Table 8 and [2, 3]). The programs are based on the numerical solution of balance equations (7.1)–(7.3) using effective cross sections and rates of interaction of ions with target particles (atoms, molecules, ions, electrons) and taking into account target *density effects*, multi-electron processes, and energy losses of ions in the medium. It should be noted that the accuracy of determining the experimental and theoretical values of the cross sections is in the range of 10–50%; therefore, the accuracy of calculating ion fractions using balance equations is approximately in the same range. The GLOBAL and CHARGE programs are available for use online at the websites [166, 167].

Table 8. List of programs available for calculating the parameters of interaction of an ion beam with a target. Nuclear charges of Z_n ions, target types, energy ranges of applicability, and methods for solving balance equations are indicated.

Program	Beam ions	Target	Energy, MeV/u	Method	Source
ETACHA (old)	$Z_n \leqslant 28$	Foil	10 – 80	Runge–Kutta	[168]
ETACHA (new)	$Z_n \leqslant 60$	Foil	0.05 – 80	Runge–Kutta	[169]
Charge	Nuclei, H-, He-like ions	Gas, foil, $Z_T \leqslant 92$	30 – 2000	Analytic three-component model [170]	[46]
Global	$Z_n > 30$	Gas, foil, $Z_T \leqslant 92$	30 – 2000	Runge–Kutta	[46]
MC	$Z_n \leqslant 28$	Plasma	> 10	Monte Carlo	[171]
BREIT	$1 \leqslant Z_n \leqslant 120$	Gas, foil, plasma	$0.001 - 10^5$	Diagonalization of interaction matrix	[160]

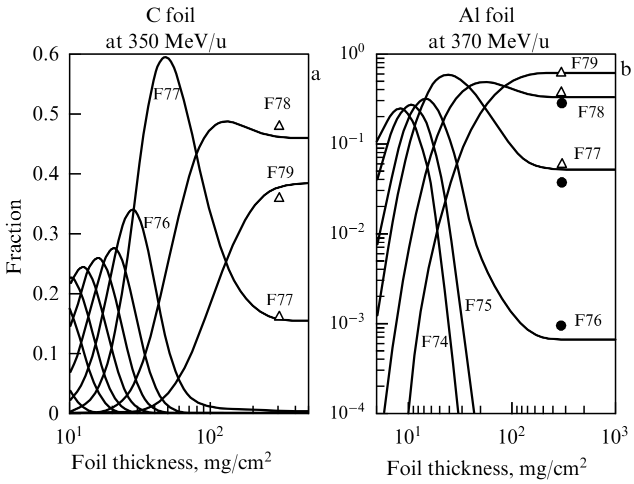

Figure 32. (a) Dependence of fractions $F_q(x)$ of gold ions Au^{78+} on foil thickness when interacting with carbon foil at $E = 350$ MeV/u and (b) aluminum foil at $E = 370$ MeV/u: triangles — GLOBAL program [46], dots — experiment [46], solid curves — BREIT program [160]. (From [13].)

Table 8 shows that the most widely used program in terms of energy, ion charge, and target type is the BREIT program [160], which provides a solution for balance equations for $n \leqslant 200$ fractions by diagonalizing the interaction matrix, which includes the total effective cross sections (or process rates) of beam ion ionization and recombination in a medium. Unlike other programs, in the BREIT program, the interaction cross sections are not calculated but are specified in the input file, which enables program users to freely select cross sections obtained from theory or experiment.

Figure 32 shows as an example the evolution of gold ion fractions upon collision with carbon and aluminum foil as a function of foil thickness. Calculations using the BREIT program in the region of the equilibrium regime are in good agreement with experimental data and calculations made using the GLOBAL program. One of the important results provided by BREIT program calculations is the excess of the fraction of Au^{77+} ions over the maximum equilibrium fraction of Au^{78+} ions (Fig. 32a), which reflects one of the specific features of the interaction of heavy ions with foils.

8. Features of interaction of ion beams with plasma

The specific features of the interaction of ion beams with plasma were examined in many studies, including reviews (see, for example, [3, 10, 11, 156, 161, 172, 173]). As noted above, the main difference between a plasma target and a gas or solid target is that the former contains free electrons, leading to the occurrence of additional processes, such as radiative and dielectronic recombination, ternary recombination, and electron impact ionization, with dielectronic recombination playing a special role (Section 8.1). In addition, an important plasma parameter, the concentration of neutral atoms, significantly depends on the temperature and electron density.

In the case of passage of an ion beam through a plasma with temperature T_e, the velocity distribution function $F(v, v_p, T_e)$ of plasma particles differs from the usual Maxwell one; it is called 'shifted' and has the form

$$F(v, v_p, T_e) = \left(\frac{M}{2\pi k T_e}\right)^{1/2} \frac{v}{v_p}\left[\exp\left(-\frac{M}{2kT_e}(v - v_p)^2\right) - \exp\left(-\frac{M}{2kT_e}(v + v_p)^2\right)\right], \qquad (8.1)$$

$$\int_0^\infty F(v, v_p, T_e)\,\mathrm{d}v = 1\,, \qquad (8.2)$$

where $v = |\mathbf{v}_p - \mathbf{v}_{e,i}|$ is the velocity of ions in the beam relative to the velocity of electrons or the velocity of ions (atoms) in plasma, T_e is the temperature of electrons, atoms, or ions, M is the reduced mass of colliding particles, and k is the Boltzmann constant.

At low velocities of incident ions $v_p \to 0$, the shifted function $F(v, v_p, T_e)$ transforms into the usual velocity distribution function

$$F(v, v_p, T_e)_{v_p \to 0} \to F(v, T_e) = 4\pi v^2 \left(\frac{M}{2\pi k T_e}\right)^{3/2} \exp\left(-\frac{Mv^2}{2kT_e}\right), \qquad (8.3)$$

$$v_p \ll v_{th}\,, \quad v_{th} \approx 1.13\sqrt{\frac{2T_e}{m}}\,, \qquad (8.4)$$

where m is the electron mass, and v_{th} is the average (thermal) velocity of electrons in plasma, which is much greater than the average velocity of atoms and ions due to the difference in mass.

Usual $(v_p = 0)$ and shifted $(v_p > 0)$ Maxwell velocity distribution functions are shown in Fig. 33 for low ($T_e = 3$ eV, thermal electron velocity $v_{th} = 0.06$ a.u.) and high ($T_e = 2000$ eV, $v_{th} = 1.58$ a.u.) plasma temperatures as functions of relative velocity v. It can be seen that the shifted functions are much 'narrower' than the usual ones and are indeed shifted to higher relative velocities v.

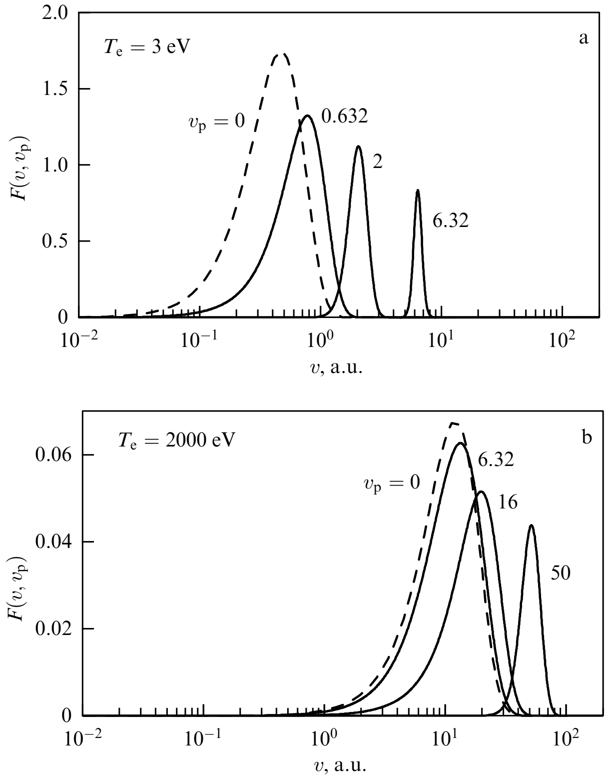

Figure 33. Velocity distribution function $F(v, v_p, T_e)$ of electrons (8.3) in the case of interaction of ions with plasma at various ion velocities v_p and two plasma temperatures $T_e = 3$ eV (a) and $T_e = 2000$ eV (b). Case $v_p = 0$ corresponds to the usual Maxwell function (8.3), dashed curves, and, for $v_p \neq 0$, to the shifted function (8.1). As v_p increases, function width decreases, and maximum shifts to the right. (From [153].)

To calculate the dynamics of interaction of ion beams with plasma, balance equations (7.4) and (7.5) are used for ion fractions $F_q(x)$ with coefficients equal to the atomic process rates of α_i [s^{-1}]:

$$\alpha_i = N_i \langle v\sigma_i \rangle \,, \tag{8.5}$$

where the process *coefficients* $\langle v\sigma_i \rangle$ have dimension [$cm^3\ s^{-1}$] and are determined by averaging the effective cross sections over the shifted distribution function $F(v, v_p, T_e)$. To determine the process rates in plasma, in addition to the effective cross sections σ_i of the interaction of ions with all plasma particles (electrons, atoms, ions, molecules), it is necessary to know the concentration of particles in plasma N_i, which are very different for each type of particle. Calculating the rates of dielectronic recombination is especially challenging due to the resonant nature of the process.

8.1 Role of dielectronic recombination. DRIMP program

To calculate the rate coefficients of DR ions moving in plasma, the DRIMP (Dielectronic Recombination of Ions Moving in Plasmas) program was developed in [153]. In the DRIMP code, level energies and probabilities of radiative and autoionization transitions are calculated in a j–j coupling scheme using the corresponding modified routines of the flexible atomic code (FAC) [174], based on the relativistic multi-configuration Dirac–Fock method. In the FAC code, the calculated level energies can be adjusted using experimental or reference data; however, in DRIMP, such a

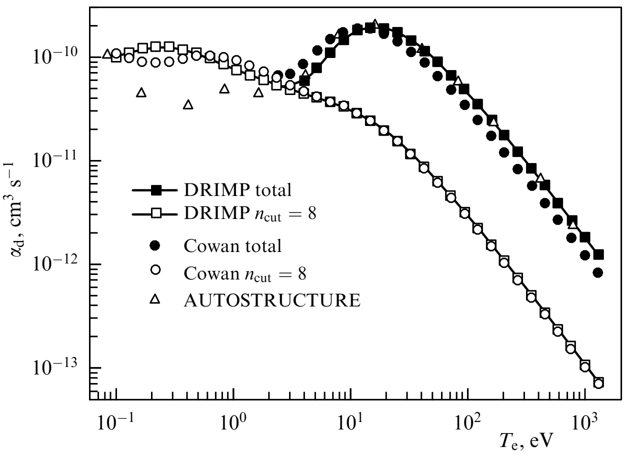

Figure 34. DR rate coefficients in C-like oxygen O^{2+} as a function of electron temperature T_e: open squares — full-scale calculations $\alpha_d(i, n_{cut})$, $n_{cut} = 8$ using the DRIMP program; solid squares — calculation of the sum $\alpha_d(i)$ using the DRIMP code, $n_{max} = 30{,}000$; open and solid circles — the same for calculations using the Cowan code from [176]; open triangles — AUTOSTRUCTURE results from [177].

function is not implemented, since this code is used to calculate the DR of any heavy ions, for many of which such data are not available.

In the case of calculations for a large number of levels (for example, for ions with an open 3d shell, when the number of levels taken into account reaches enormous values of the order of 10^5 !), full-scale calculations become very problematic. In this case, level energies and transition rates are calculated in the DRIMP program in the so-called unresolved transition array (UTA) mode, implemented in the FAC code and based on the average configuration approximation [175, 176]. In the UTA mode, the levels are constructed without taking into account the type of angular momentum coupling, which leads to a significant reduction in their number compared to full-scale calculations in the j–j coupling scheme.

To check the reliability of calculations using the DRIMP program, the velocity coefficients of DR ions in plasma (6.41) were calculated in [153] and compared with theoretical data.

In Figure 34, the results of full-scale calculations (i.e., not based on the UTA mode) using Eqn (6.45) with $n_{cut} = 8$ and $n_{max} = 30{,}000$ are compared with theoretical calculations of the dielectronic recombination coefficient of O^{3+} ions, calculated with the same parameters as in [176] and [177]. Low-charge ions were chosen to test the DRIMP code in the mode least favorable for calculating level energies: the larger the charge, the more accurate the calculation of the energies in the code. In [176], energy levels, radiative transition probabilities, and autoionization rates were calculated in the relativistic approximation using the Hartree–Fock method (Cowan program [178]) in an intermediate coupling scheme. The results are obtained in [177] using the AUTOSTRUCTURE code [179] based on the multi-configuration Breit–Pauli approximation, with $n_{cut} = 15$ and $n_{max} = 1000$.

Figure 34 shows that the DR rate coefficients with $n_{cut} = 8$ and $n_{max} = 30{,}000$ in Eqn (6.45), calculated using the DRIMP code, are in good agreement with calculations made using the Cowan and AUTOSTRUCTURE programs over the entire range of electron temperatures, which confirms the reliability of full-scale DRIMP calculations.

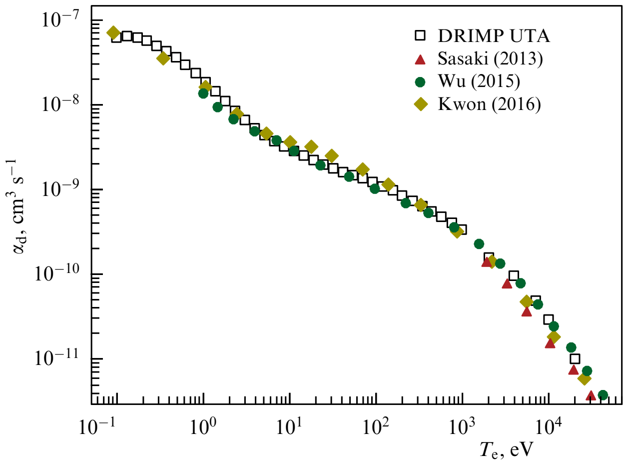

Figure 35. DR rate coefficients in $W^{44+}(3s^23p^63d^{10}4s^2)$ as a function of electron temperature T_e: open squares — DRIMP-UTA calculations with $n_{max} = 10{,}000$; solid triangles — data from [181]; solid diamonds — data from [182]; and solid circles — data from [180].

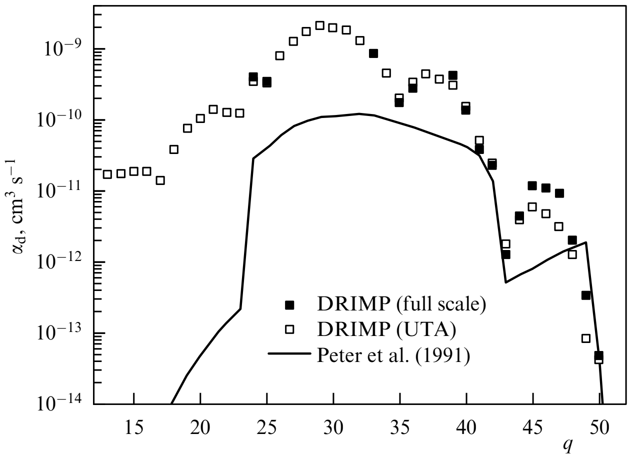

Figure 36. DR rate coefficients for an iodine beam with an energy of 1.5 MeV/u passing through a fully ionized hydrogen plasma with electron temperature $T_e = 10$ eV and density $N_e = 10^{20}$ cm^{-3} vs ion charge q: solid curve — results from [156]; solid squares — full-scale calculations using the DRIMP code; solid squares — DRIMP code calculation in UTA mode.

Figure 35 displays the total DR velocities of Zn-like ions W^{44+} ($n_{max} = 10{,}000$) calculated using the DRIMP program in the UTA mode [153], which are compared with the theoretical calculations presented in [180–182]. The DR velocities in [180] are calculated in the approximation of an independent process, an isolated resonance, and a distorted wave. In [181], atomic data — energy levels and rates of radiative and autoionization decays — were calculated *ab initio* using the HULLAC code [183] without taking into account the interaction between configurations. Data were obtained in [182] using the multi-configuration Dirac–Fock method. Figure 35 shows that the results of the DRIMP-UTA program are in good agreement with all theoretical data presented over the entire range of electronic temperatures.

8.2 Dielectronic recombination of ions in interaction of an ion beam with plasma

In [153], the DR coefficients of ions moving in plasma, which are calculated using the DRIMP program, are compared with the only available data obtained in [156] for iodine ions I^{q+} with an energy of 1.5 MeV/u and charges $q = 12-50$, passing through a fully ionized hydrogen plasma with an electron temperature $T_e = 10$ eV and a density $N_e = 10^{20}$ cm^{-3}. The calculations made in [156] are based on relatively simple atomic simulations and use screened hydrogen energies, wave functions, and oscillator strengths (transition probabilities). To compare the DRIMP results with the results of [156], calculations were made in [153] for the same case using Eqn (6.42) and taking into account all decay channels of the doubly excited state (2.3). To take into account the influence of plasma density, the same formulas are used as in [184]. A consequence of density effects is a decrease in the continuum limit due to dynamic screening of a moving ion, when free electrons screen plasma ions so effectively that the electron in the nth shell ceases to be bound. In this case, n_{max} in equation (6.42) is determined by the condition

$$n_{max} = \left[\frac{q^2}{8\pi}\,\frac{kT_e}{\mathrm{Ry}}\,\frac{1}{N_e a_0^3}\right]^{1/4}\left[1 + \frac{1}{12}\,(4-\pi)\,\frac{v_p^2}{kT_e/m}\right]^{1/2}. \quad (8.6)$$

Another effect is a decrease in the ionization boundary due to the overlap of the wave functions of the moving ion and target ions, which yields the following condition for n_{max}:

$$n_{max} = \left[\frac{3q^3 T_e}{4\pi N_i\, a_0^3}\right]^{1/6}, \quad (8.7)$$

where N_i is the density of plasma ions. In the calculations made in [153] for n_{max}, Eqn (8.6) or (8.7) was used — depending on where the value of n_{max} is greater — the same as in [156]. Due to the large number of levels (up to 10^5) in iodine ions with a 3d shell ($q \leqslant 34$), level energies and transition probabilities were calculated in [153] in the UTA mode, based on the average configuration approximation [175, 176]. The results of full-scale DRIMP and UTA calculations, along with the results reported in [156], are presented in Fig. 36. It should be noted that the results of the two DRIMP modes agree well for all ions up to Ne-like I^{43+}. At larger charges, the UTA approximation underestimates the DR velocities due to the small number of levels taken into account.

The results of calculations in two DRIMP modes and data from [156] show that the total DR velocity features a pronounced n-shell structure: an increase in α_d at $q = 42$ corresponds to the opening of the $n = 3$ shell, and a decrease at $q = 23$, to the opening of the $n = 4$ shell.

The decrease in α_d at $q = 23$ (Zn-like I, $3s^23p^63d^{10}4s^2$) is related to a significant contribution to the autoionization decay channel of the following process:

$$\begin{aligned} I^{q+}(3s^23p^63d^{10}4l^k) + e &\rightarrow I^{(q-1)+}(3s^23p^63d^94l^k n'l') \\ &\rightarrow I^{q+}(3s^23p^63d^{10}4l^{(k-1)}n'l') + e, \\ q \leqslant 23\,, & \quad (8.8) \end{aligned}$$

i.e., autoionization of a valence electron with $n = 4$ after excitation of an electron from the inner shell with $n = 3$ (3d electron in Eqn (8.8)). The excitation of inner-shell electrons plays a significant role at high relative velocities of the heavy ion and free electron, and in the case under consideration makes the main contribution to α_d for ions with $q \leqslant 23$. Compared with the data from [156], the DRIMP results, in addition to the n-shell structure, reflect the structure corresponding to the filling of the nl-subshells (Fig. 36).

The significant difference between the DR rates calculated using the DRIMP code and the results obtained in [156] is due to different calculation methods: the use of relativistic wave functions, accounting for the interaction between configurations, the $j-j$ coupling scheme, and the UTA method for calculating level energies and probabilities of transitions taking into account states with large n in the DRIMP code vs. Slater (nodeless) and hydrogen-like wave functions, screened hydrogen-like energies, and oscillator strengths in [156]. The difference becomes significant for iodine ions with charge $q \leqslant 23$.

8.3 Charge-state distribution of process rates with account for dielectronic recombination

Study [153] examined the electron loss of iodine ions I^{q+} ($q = 13-51$) with an energy of 1.5 MeV/u in a hydrogen plasma with electron temperature $T_e = 10$ eV and density $N_e = 10^{20}$ cm^{-3}, taking into account all ionization and recombination rates, including DR rates. Figure 37 shows the dielectronic recombination rates as a function of ion charge q. For DR rates, two results are presented in the figure: the values calculated in [156] and those obtained [153] using the DRIMP code. Ionization rates (EL) and recombination rates (EC, without DR contribution) were taken from [156].

Arrows at the points of intersection of the EL, EC, and DR curves in Fig. 37 show the approximate average equilibrium charges for cases with and without DR. The average charges $\bar{q}$ in the cases without DR and with DR taken into account are equal, respectively: $\bar{q}$ without DR ≈ 41, $\bar{q}$ with DR ≈ 31 (from [156]) and $\bar{q}$ with DR ≈ 26 (DRIMP). This implies that the influence of DR processes of the ions passing through a plasma target is very large and leads to a significant decrease in the average charge, as indicated in [156]. More accurate calculations of the DR rates made in [153] indicate a further decrease in the average charge $\bar{q}$.

Figure 38 presents the calculation of the charge state distribution of iodine ions with an energy of 1.5 MeV/u in a cold hydrogen plasma. They were obtained using the BREIT code [160] by solving the balance equations for rates (7.4) and (7.5) with rates $\alpha_{qq'}$ presented in Fig. 37 used as input to the code. The three cases (a)–(c) shown in Fig. 39 clearly show that the average charges decrease from $\bar{q} = 41.4$, which corresponds to calculations without taking DR into account, to $\bar{q} = 31.6$, calculated using the DR coefficients from [156], and to $\bar{q} = 26.1$, obtained using DR coefficients calculated using the DRIMP code in [153]. The hydrogen plasma thicknesses at which the equilibrium regime is attained decrease from $X_{eq} = 5$ mg cm^{-2} (Fig. 38a) to $X_{eq} = 0.5$ mg cm^{-2} (Fig. 38b) and to $X_{eq} = 0.05$ mg cm^{-2} (Fig. 38c). These results clearly indicate the large influence of the DR process on the charge state distribution of ions passing through the plasma target and the importance of accurate determination of the DR rates. A decrease in the equilibrium thickness of the plasma also implies that the plasma source length required to attain the equilibrium regime can be significantly less than when it is determined without taking into account the DR of ions moving in plasma.

Figure 40 shows the distributions of *equilibrium* fractions $F_q(\infty)$ of iodine ions moving in hydrogen plasma over the ion charge q calculated using the BREIT code with and without DR. The final distribution with $\bar{q} = 26.1$, calculated with the DR rates from [153] (DRIMP code), is narrower than the other two distributions and has a larger value at the maximum.

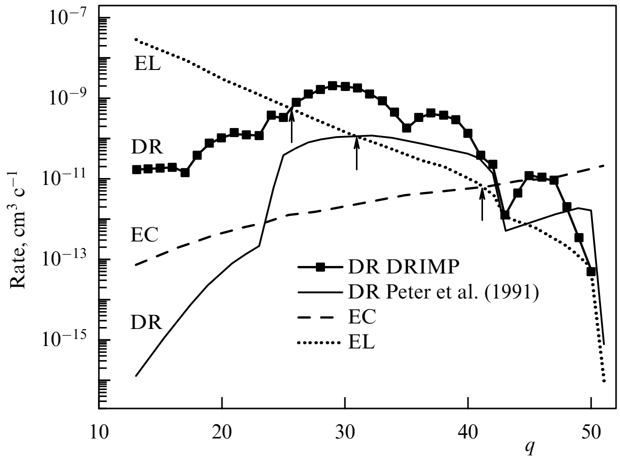

Figure 37. Rate coefficients for ionization and recombination of I^{q+} ions with an energy of 1.5 MeV/u in hydrogen plasma with electron temperature $T_e = 10$ eV and density $N_e = 10^{20}$ cm^{-3} calculated using the shifted Maxwell function. EL is the total rate of all ionization processes from [156]; EC is the total rate of all recombination processes, except DR, from [156]; solid line is the DR rate from [156]; line with symbols is DR from [153]. Arrows indicate the approximate average charges of an iodine ion beam under various assumptions (see text).

9. Conclusion

The properties of effective cross sections and rates of elementary processes in collisions of multiply charged ions with atomic particles are considered. The features of the processes significantly depend on the atomic structure of the colliding particles and their relative velocity. For example, in the case of electron capture of ions on atoms at high energies, the main feature of the process is the capture of inner-shell electrons of the target atom, and in the case of dielectronic recombination, the matching of the kinetic energy of a free electron with the excitation energy of the incident ion, leading to the formation of a resonance in the cross section. Collisions at relativistic energies represent a special case: the cross sections of ionization of ions by atoms (electron-loss cross sections) become independent of the ion energy due to purely relativistic interaction between colliding particles; the cross sections of nonradiative electron capture decrease much more slowly than in the region of high but nonrelativistic energies due to the increasing contribution of radiative electron capture.

The properties of atomic processes determine the effective cross sections and process rates, their dependence on the ion energy, and the temperature of the medium, which in turn affect the characteristics of the interaction of ion beams with media: gas, solid-state (foils), and plasma. For example, the ion beam lifetimes in accelerator systems at relativistic energies are almost completely determined by electron-loss cross sections, the quasi-constant nature of which leads to constant values of lifetimes, also independent of energy with its further growth. Another example is the violation of Gaussian symmetry of equilibrium functions $F_q(\infty)$ as a function of charge q, which is due to several reasons: the influence of target density effects in gases and foils, the effect of dielectronic recombination in plasma, relativistic effects, etc.

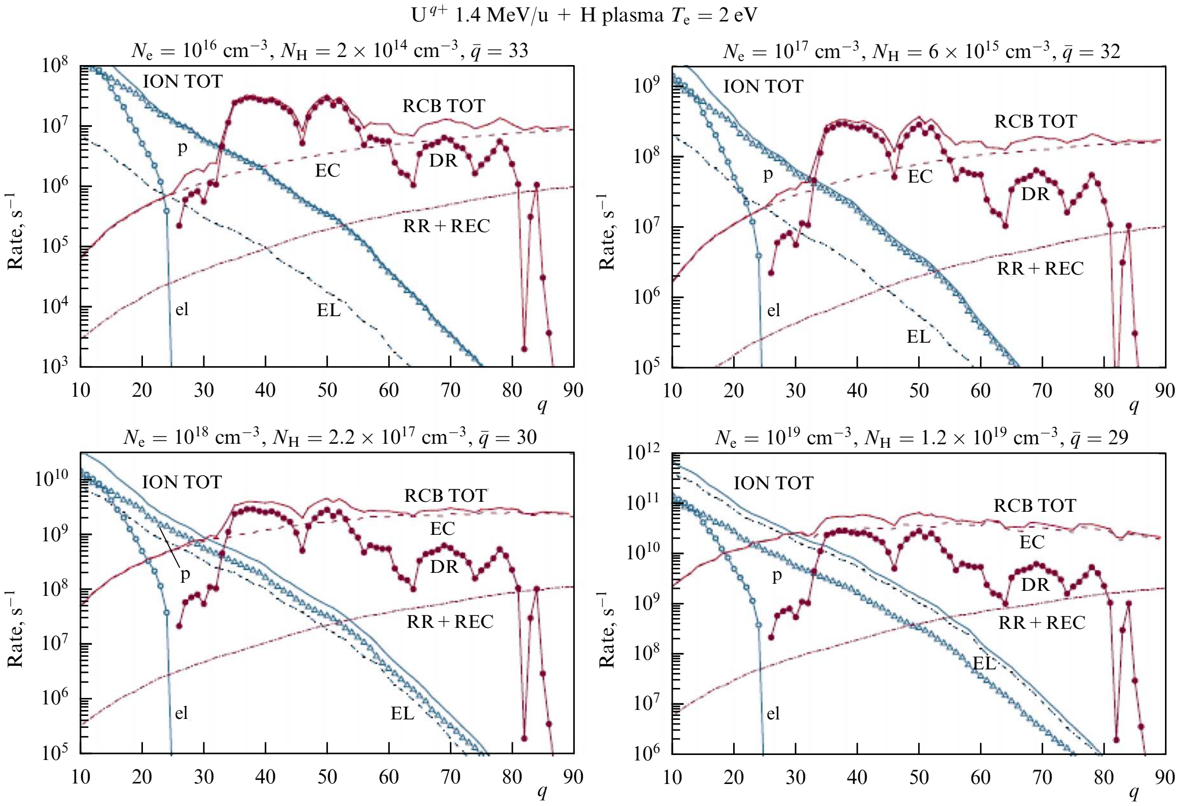

Figure 38. Calculated rates of ionization and recombination of uranium ions with an energy of 1.4 MeV/u passing through a hydrogen plasma with electron temperature $T_e = 2$ eV and density $N_e = 10^{14} - 10^{19}$ cm^{-3} as a function of ion charge q. N_H is the hydrogen density, $\bar{q}$ is the average equilibrium charge of a beam of uranium ions; calculations made using the BREIT program. Process coefficients were calculated using ATOM, CAPTURE, RICODE-M, and DRIMP programs. Designations: el, p, EL, and ION TOT are the rates of ionization by electrons, protons, and hydrogen atoms and total (summed) cross sections of ionization of uranium ions, respectively; RR, REC, DR, EC, and RCB TOT are the rates of radiative recombination, radiative electron capture, dielectronic recombination, nonradiative electron capture, and total recombination rate, respectively. (From [161].)

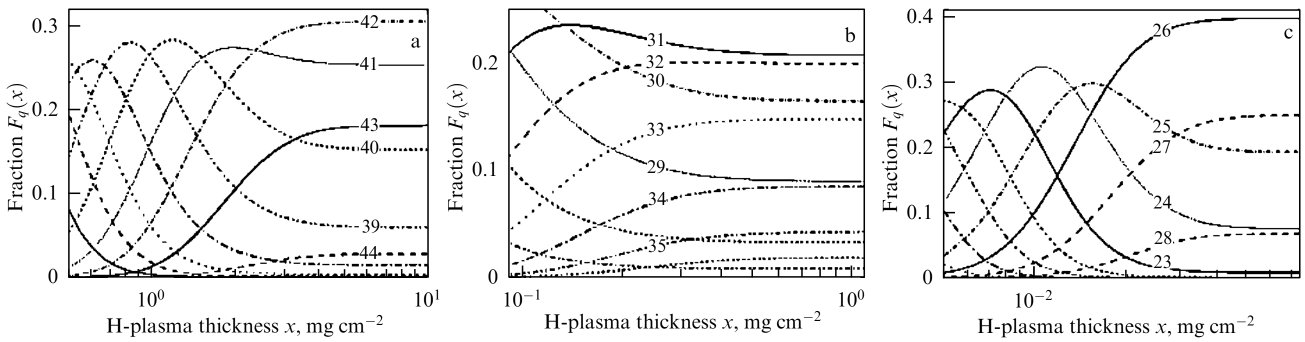

Figure 39. Distributions of fractions of I^{q+} ions with an energy of 1.5 MeV/u in hydrogen plasma with electron temperature $T_e = 10$ eV and density $N_e = 10^{20}$ cm^{-3} as a function of hydrogen density; results of calculations using the BREIT program. (a) Without taking DR into account, the average charge $\bar{q} = 41.4$, (b) taking DR into account [156], $\bar{q} = 31.6$, (c) taking DR into account [153], $\bar{q} = 26.1$. (From [153].)

New theoretical results regarding the role of dielectronic recombination during the interaction of heavy ion beams with hydrogen plasma are presented. The influence of this process turned out to be very significant, leading to three main implications: a decrease in the equilibrium charges of the ion beam, a reduction in the equilibrium plasma thickness, and a distortion of the Gaussian shape of the equilibrium distributions of charge states over the ion charge at the exit from the target.

The list of unsolved problems that require further examination includes the study of ionization and electron capture of heavy low-charge ions interacting with gas targets (He, N_2, Ne, Ar) at low collision energies $E \sim 0-50$ keV. This problem is associated with the study of so-called *exotic* nuclei, i.e., nuclei with an unusual ratio of the number of protons to the number of neutrons compared to stable isotopes, short-lifetime nuclei and nuclei with an unusual structure of the nuclear shell with new magic numbers, and the detection of superheavy elements. Experimental and theoretical studies in this area being are actively carried out at accelerator centers based in Russia, Japan, Germany, the USA. and other countries. The physical properties of exotic nuclei are of great interest for many problems related to astrophysics, condensed matter physics, particle accelerators, medical applications, etc. Information on cross sections of processes with changes in the charge of exotic ions in various

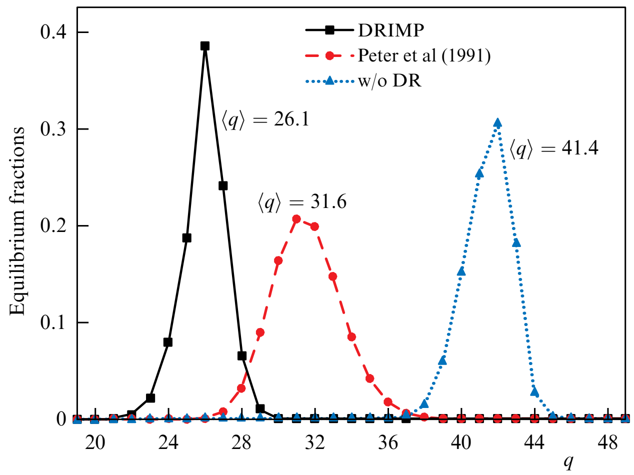

Figure 40. Equilibrium charge fractions $F_q(\infty)$ of I^{q+} ions with an energy of 1.5 MeV/u in hydrogen plasma with electron temperature $T_e = 10$ eV and density $N_e = 10^{20}$ cm^{-3} as a function of ion charge — BREIT results: squares — without taking DR rates into account, dots — DR rates obtained in [156], triangles — DR rates obtained in [153].

gases and on the distribution of charge states of heavy ions (such as Sr, Cd, Ba, Y, Pt) is extremely necessary for the efficient production of low-energy rare-isotope beams (RIBs), effective manipulation using electromagnetic devices, and the study of their unusual nuclear structure. Recently, the first experimental results have been obtained in measurements of the fractions of the heavy low-charge ions Sr, Ba, and Nd at energies $E = 8-60$ keV, and cross sections of the ionization and electron capture of ions in this region have been calculated [184]. Experimental and theoretical studies of the properties of heavy ions at ultra-low energies should certainly be continued.

Acknowledgments. The authors are grateful to I N Meshkov and A V Filippov (JINR, Dubna) and to Yu A Litvinov (GSI, Darmstadt) for interest in the work and their useful comments.

References

1. Tolstikhina I Yu, Shevelko V P *Phys. Usp.* **56** 213 (2013); *Usp. Fiz. Nauk* **183** 225 (2013)
2. Tolstikhina I Yu, Shevelko V P *Phys. Usp.* **61** 247 (2018); *Usp. Fiz. Nauk* **188** 267 (2018)
3. Tolstikhina I, Imai M, Winckler N, Shevelko V *Basic Atomic Interactions of Accelerated Heavy Ions in Matter: Atomic Interactions of Heavy Ions* (Springer Ser. on Atomic, Optical, and Plasma Physics, Vol. 98) (Cham: Springer Intern. Publ., 2018)
4. Sobelman I I, Vainshtein L A, Yukov E A *Excitation of Atoms and Broadening of Spectral Lines* (Berlin: Springer-Verlag, 1981); Translated from Russian: *Vozbuzhdenie Atomov i Ushirenie Spektral'nykh Linii* (Moscow: Nauka, 1979)
5. Janev R K, Presnyakov L P, Shevelko V P *Physics of Highly Charged Ions* (Springer Series in Electrophysics, Vol. 13) (Berlin: Springer-Verlag, 1985); Translated into Russian: *Elementarnye Protsessy s Uchastiem Mnogozaryadnykh Ionov* (Moscow: Energoatomizdat, 1986)
6. Solov'ev E A *Novye Podkhody v Kvantovoi Fizike* (New Approaches in Quantum Physics) (Moscow: Fizmatlit, 2019)
7. Steck M, Litvinov Yu A *Prog. Part. Nucl. Phys.* **115** 103811 (2020)
8. Paul N et al. *Phys. Rev. Lett.* **126** 173001 (2021)
9. Ma X et al. *Chinese Phys. B* **31** 093401 (2022)
10. Sigmund P *Particle Penetration and Radiation Effects* Vol. 2 *Penetration of Atomic and Molecular Ions* (Springer Ser. in Solid-State Sciences, Vol. 179) (Cham: Springer, 2014) https://doi.org/10.1007/978-3-319-05564-0
11. Rosmej F B, Astapenko V A, Lisitsa V S *Plasma Atomic Physics* (Springer Ser. on Atomic, Optical, and Plasma Physics, Vol. 104) (Cham: Springer, 2021) https://doi.org/10.1007/978-3-030-05968-2
12. Dikanskii N S et al. *Phys. Usp.* **61** 424 (2018); *Usp. Fiz. Nauk* **188** 481 (2018)
13. Shevelko V P, Winckler N, Tolstikhina I Yu *Phys. Rev. A* **101** 012704 (2020)
14. Budker D et al. *Ann. Physik* **534** 2100284 (2022)
15. Oganessian Yu Ts, Utyonkov V K *Rep. Prog. Phys.* **78** 036301 (2015)
16. Yamaguchi Y et al. *Prog. Part. Nucl. Phys.* **120** 103882 (2021)
17. Schardt D, Elsässer Th, Schulz-Ertner D *Rev. Mod. Phys.* **82** 383 (2010)
18. Trautmann C, in *Ion Beams in Nanoscience and Technology* (Ed. R Hellborg, H J Whitlow, Y Zhang) (Heidelberg: Springer-Verlag, 2009)
19. Nuclotron-based Ion Collider fAcility, NICA, http://nica.jinr.ru/
20. Kekelidze V D et al. *Eur. Phys. J. A* **52** 211 (2016)
21. Kozlov O S et al. *Phys. Part. Nucl.* **53** 1021 (2022); *Fiz. Elem. Chast. At. Yad.* **53** 1220 (2022)
22. Placzek W et al. *Acta Phys. Polon. B* **50** 1191 (2019)
23. Henning W F (Ed.) "International Accelerator Facility for Beams of Ions and Antiprotons", GSI-Darmstadt, November 2001, http://www.fair-center.de/fileadmin/fair/publicationsFAIR/FAIR-CDR.pdf
24. Shevelko V, Tawara H *Atomic Multielectron Processes* (Berlin: Springer, 1998)
25. Matsuo T et al. *Phys. Rev. A* **50** 1178 (1986)
26. Eichler J, Meyerhof W E *Relativistic Atomic Collisions* (San Diego, CA: Academic Press, 1995)
27. Eichler J, Stöhlker T *Phys. Rep.* **439** 1 (2007)
28. Müller A *Adv. Atom. Mol. Opt. Phys.* **55** 293 (2008)
29. Poth H *Phys. Rep.* **196** 135 (1990)
30. Bates D R, Moffett R J *Nature* **205** 272 (1965)
31. Raizer Yu P *Gas Discharge Physics* (Berlin: Springer, 1997); Translated from Russian: *Fizika Gazovogo Razryada* (Moscow: Nauka, 1992)
32. Beigman I L, Vainshtein L A, Syunyaev R A *Sov. Phys. Usp.* **11** 411 (1968); *Usp. Fiz. Nauk* **95** 269 (1968)
33. Melchert F "Charge changing processes in ion-ion collisions", in *Atomic Physics with Heavy Ions* (Springer Ser. on Atoms + Plasmas, Vol. 26, Eds H Beyer, V P Shevelko) (Berlin: Springer, 1999)
34. Shevelko V P et al. *Nucl. Instrum. Meth. Phys. Res. B* **269** 1455 (2011)
35. Tolstikhina I Yu et al. *J. Exp. Theor. Phys.* **119** 1 (2014); *Zh. Eksp. Teor. Fiz.* **146** 5 (2014)
36. Rashid K, Saadi M Z, Yasin M *Atom. Data Nucl. Data Tabl.* **40** 365 (1988)
37. Lotz W *J. Opt. Soc. Am.* **58** 915 (1968); *J. Opt. Soc. Am.* **60** 206 (1970)
38. Erb W, GSI Report P-7-78 (Darmstadt: GSI, 1978)
39. Perumal A N et al. *Nucl. Instrum. Meth. Phys. Res. B* **227** 251 (2005)
40. Shevelko V P et al. *Nucl. Instrum. Meth. Phys. Res. B* **278** 63 (2012)
41. Shevelko V P et al. *J. Phys. B* **43** 215202 (2010)
42. Litsarev M S *Comput. Phys. Commun.* **184** 432 (2013)
43. Olson R E et al. *J. Phys. B* **37** 4539 (2004)
44. Weber G et al. *Phys. Rev. ST Accel. Beams* **18** 034403 (2015)
45. Anholt R, Becker U *Phys. Rev. A* **36** 4628 (1987)
46. Scheidenberger C et al. *Nucl. Instrum. Meth. Phys. Res. B* **142** 441 (1998)
47. Anholt R *Phys. Rev. A* **19** 1004 (1979)
48. Anholt R et al. *Phys. Rev. A* **36** 1586 (1987)
49. Bertulani C A, Baur G *Phys. Rep.* **163** 299 (1988)
50. Voitkiv A B *Phys. Rep.* **392** 191 (2004)
51. Voitkiv A, Ullrich J *Relativistic Collisions of Structured Atomic Particles* (Springer Series on Atomic, Optical, and Plasma Physics) (Berlin: Springer, 2008) https://doi.org/10.1007/978-3-540-78421-0
52. Baur G et al. *Phys. Rev. A* **80** 012713 (2009)
53. Geissel H et al. *Nucl. Instrum. Meth. Phys. Res. B* **195** 3 (2002)

54. Dutheil Y et al. "Gamma Factory for CERN initiatives — progress report", in *European Physical Society Conf. on High Energy Physics EPS-HEP2019, 10–17 July, 2019, Ghent, Belgium*; *PoS* **EPS-HEP2019** 020 (2019)
55. Mueller D et al. *Phys. Plasmas* **8** 1753 (2001)
56. Watson R L et al. *Phys. Rev. A* **67** 022706 (2003)
57. Olson R E et al. *J. Phys. B* **37** 4539 (2004)
58. Olson R E, Ullrich J, Schmidt-Böcking H *Phys. Rev. A* **39** 5572 (1989)
59. Olson R E, in *Atomic, Molecular, and Optical Physics Handbook* (Ed. G W F Drake) (Woodbury, NY: AIP Press, 1996) p. 869
60. Lo H H, Tite W L *Atom. Data* **1** 305 (1969)
61. Firsov O B *Sov. Phys. JETP* **9** 1076 (1959); *Zh. Eksp. Teor. Fiz.* **36** 1517 (1959)
62. Kunc J A, Soon W H *J. Chem. Phys.* **95** 5738 (1991)
63. Shevelko V P et al. *J. Phys. B* **42** 065202 (2009)
64. Franzke B *IEEE Trans. Nucl. Sci.* **28** 2116 (1981)
65. DuBois R D et al. *Phys. Rev. A* **70** 032712 (2004)
66. Smolyakov A, Spiller P, Internal Note ACC-note-internal-2006-001 (Darmstadt: GSI, 2006)
67. Klinger H, Muller A, Salzborn E *J. Phys. B* **8** 230 (1975)
68. Ryufuku H, Watanabe T *Phys. Rev. A* **19** 1538 (1979)
69. Presnyakov L P, Ulantsev A D *Sov. J. Quantum Electron.* **4** 1320 (1975); *Kvant. Elektron.* **1** 3277 (1074)
70. Chibisov M I *JETP Lett.* **24** 46 (1976); *Pis'ma Zh. Eksp. Teor. Fiz.* **24** 56 (1976)
71. Shevelko V P et al. *J. Phys. B* **37** 201 (2004)
72. Schlachter A S et al. *Phys. Rev. A* **27** 3372 (1983)
73. Fermi E *Phys. Rev.* **57** 485 (1940)
74. Lassen N O *Kgl. Danske Vidensk. Selskab. Mat.-Fyz. Medd.* **26** (12) (1951)
75. Bohr N, Lindhard J *Kgl. Danske Vidensk. Selskab. Mat.-Fyz. Medd.* **28** (7) (1954)
76. Betz H D, Grodzins L *Phys. Rev. Lett.* **25** 211 (1970)
77. Geissel H et al. *Nucl. Instrum. Meth. Phys. Res.* **194** 21 (1982)
78. Basko M M *Sov. J. Plasma Phys.* **10** 689 (1984); *Fiz. Plazmy* **10** 1195 (1984)
79. Val H et al. *Kratk. Soobshch. Fiz. Inst. Akad. Nauk* (8) 28 (2001)
80. Shevelko V P et al. *J. Phys. B* **38** 525 (2005)
81. Ogawa H et al. *Phys. Rev. A* **75** 020703 (2007)
82. Shevelko V P, Winckler N, Tolstikhina I Yu *Nucl. Instrum. Meth. Phys. Res. B* **377** 77 (2016)
83. Barat M, Roncin P *J. Phys. B* **25** 2205 (1992)
84. Klinger H, Muller A, Salzborn E *J. Phys. B* **8** 230 (1975)
85. Müller A, Salzborn E *Phys. Lett. A* **62** 391 (1977)
86. Bárány A et al. *Nucl. Instrum. Meth. Phys. Res. B* **9** 397 (1985)
87. Hansen J P, Taulbjerg K *Phys. Rev. A* **45** R4214 (1992)
88. Mann R *Z. Phys. D* **3** 85 (1986)
89. Sidorovich V A, Nikolaev V S, McGuire J H *Phys. Rev. A* **31** 2193 (1985)
90. Cederquist H et al. *Phys. Scr.* **1999** (T80A) 46 (1999)
91. Stöhlker Th et al. *Phys. Rev. A* **51** 2098 (1995)
92. Scheidenberger C et al. *Nucl. Instrum. Meth. Phys. Res. B* **90** 36 (1994)
93. Fettouhi A et al. *Nucl. Instrum. Meth. Phys. Res. B* **245** 32 (2006)
94. Eichler J *Phys. Rev. A* **32** 112 (1985)
95. Meyerhof W E et al. *Phys. Rev. A* **32** 3291 (1985)
96. Kramers H A *Philos. Mag.* **46** 836 (1923)
97. Ichihara A, Eichler J *Atom. Data Nucl. Data Tabl.* **74** 1 (2000)
98. Kröger F M et al. *Phys. Rev. A* **102** 042825 (2020)
99. Stobbe M *Ann. Physik* **399** 661 (1930)
100. Stöhlker Th et al. *AIP Conf. Proc.* **506** 389 (2000)
101. Fritzsche S, Surzhykov A, Stöhlker Th *Phys. Rev. A* **72** 012704 (2005)
102. Meng L, Reinhold C O, Olson R E *Phys. Rev. A* **40** 3637 (1989)
103. Watson R L et al. *Phys. Rev. A* **67** 022706 (2003)
104. Knudsen H, Haugen H K, Hvelplund P *Phys. Rev. A* **24** 2287 (1981)
105. Nakai Y et al. *Phys. Scr.* **1989** (T28) 77 (1989)
106. Meyer F W et al. *Phys. Rev. A* **19** 515 (1979)
107. Bohr N, Lindhard J *Kgl. Danske Vidensk. Selskab. Mat.-Fyz. Medd.* **28** 1 (1954)
108. Olson R E, Salop A *Phys. Rev. A* **14** 579 (1976)
109. Bottcher C, in *Coherence and Correlations in Atomic Collisions* (Eds H Kleinpoppen, J F Williams) (New York: Plenum Press, 1980)
110. Bozyk L et al. *Nucl. Instrum. Meth. Phys. Res. B* **372** 102 (2016)
111. Krasny M W "The Gamma Factory proposal for CERN", arXiv:1511.07794
112. Hirlaender S et al., in *Proc. of the 9th Intern. Particle Accelerator Conf., IPAC2018, April 29–May 4, 2018, Vancouver, BC, Canada* (Geneva: JACoW, 2018) THPMF015, http://jacow.org/ipac2018/papers/thpmf015.pdf
113. Placzek W et al. *Acta Phys. Polon. B* **50** 1191 (2019)
114. Schaumann M et al. *J. Phys. Conf. Ser.* **1350** 012071 (2019)
115. Tolstikhina I Yu, Shevelko V P "Beam-gas collisions at SPS and LHC", Report, March 25, 2019 (Geneva: CERN, 2019)
116. Kersevan R et al. "PSI collisions with residual gas in the SPS and LHC storage rings at CERN", May 2019, unpublished
117. Sidorin A O, Trubnikov G V, Shurkhno N A *Phys. Usp.* **59** 264 (2016); *Usp. Fiz. Nauk* **186** 275 (2016)
118. Butenko A V et al. *JETP Lett.* **113** 752 (2021); *Pis'ma Zh. Eksp. Teor. Fiz.* **113** 784 (2021)
119. Shevelko V P et al. *Nucl. Instrum. Meth. Phys. Res. B* **421** 45 (2018)
120. Budker G I, Skrinskii A N *Sov. Phys. Usp.* **21** 277 (1978); *Usp. Fiz. Nauk* **124** 561 (1978)
121. Parkhomchuk V V, Skrinskii A N *Phys. Usp.* **43** 433 (2000); *Usp. Fiz. Nauk* **170** 473 (2000)
122. Shi W et al. *Eur. Phys. J. D* **15** 145 (2001)
123. Budker G I *Sov. Atom. Energy* **22** 438 (1967); *Atom. Energ.* **22** 346 (1967)
124. Grieser M "The Heavy Ion Storage Ring TSR", talk at *64th ISCC Meeting, CERN, July 3, 2012*
125. Grieser M et al. *Eur. Phys. J. Spec. Top.* **207** 1 (2012)
126. Philippov A V, Kuznetsov A B, Meshkov I N, in *Proc. Workshop on Beam Cooling and Related Topics, COOL'11, September 12–16, 2011, Alushta* (Dubna: JINR, 2011) p. 48
127. Krantz C et al. *Phys. Rev. Accel. Beams* **24** 050101 (2021)
128. Schippers S et al. *Phys. Scr.* **2011** (T144) 014039 (2011)
129. Gao H et al. *Hyperfine Interact.* **99** 301 (1996)
130. Lotz W *Z. Phys.* **220** 466 (1969)
131. Beigman I L, Shevelko V P, Tawara H *Phys. Scr.* **53** 534 (1996)
132. Schury D et al. *J. Phys. Conf. Ser.* **1412** 152011 (2020)
133. Müller A "Ion formation processes: ionization in ion-electron collisions", in *Physics of Ion Impact Phenomena* (Springer Ser. in Chemical Physics, CHEMICAL, Vol. 5, Ed. D Mathur) (Berlin: Springer, 1991) p. 13, https://doi.org/10.1007/978-3-642-84350-1_2
134. LaGattuta K J, Hahn Y *Phys. Rev. A* **24** 2273 (1981)
135. Henry R J W, Msezane A Z *Phys. Rev. A* **26** 2545 (1982)
136. Müller A et al. *Phys. Rev. Lett.* **61** 70 (1988)
137. Müller A et al. *Nucl. Instrum. Meth. Phys. Res. B* **10–11** 204 (1985)
138. Defrance P, in *Atomic and Molecular Processes in Fusion Edge Plasmas* (Ed. R K Janev) (New York: Plenum Press, 1995) p. 153
139. Deutsch H, Becker K, Märk T D *Contrib. Plasma Phys.* **35** 421 (1995)
140. Fisher V et al. *J. Phys. B* **28** 3027 (1995)
141. Shevelko V P, Tawara H *J. Phys. B* **28** L589 (1995)
142. Bélenger C et al. *J. Phys. B* **30** 2667 (1997)
143. Hahn M, Müller A, Savin D W *Astrophys. J.* **850** 122 (2017)
144. Andreev G I, Bychkov V L, Shevelko V P *JETP Lett.* **117** 435 (2023); *Pis'ma Zh. Eksp. Teor. Fiz.* **117** 428 (2023)
145. Shevelko V P, Tawara H, Salzborn E "Multiple-ionization cross sections of atoms and ions by electron impact", Preprint NIFS-DATA-27 (Nagoya, Japan: Research Information Center, National Institute for Fusion Science, 1995); https://www.nifs.ac.jp/report/NIFS-DATA-027.pdf
146. Shevelko V P et al. *J. Phys. B* **38** 525 (2005)
147. Shevelko V P et al. *J. Phys. B* **39** 1499 (2006)
148. Stenke M et al. *J. Phys. B* **32** 3641 (1999)
149. Mokler P H, Stöhlker Th *Adv. Atom. Mol. Opt. Phys.* **37** 297 (1996)
150. Carlson T A et al. *Atom. Data* **2** 63 (1970)
151. Gao H et al. *J. Phys. B* **30** L499 (1997)
152. Badnell N R *Astrophys. J.* **379** 356 (1991)
153. Tolstikhina I Yu et al. *J. Quant. Spectrosc. Radiat. Transf.* **246** 106944 (2020)
154. Gurevich A V, Pitaevskii L P *Sov. Phys. JETP* **19** 870 (1964); *Zh. Eksp. Teor. Fiz.* **46** 1281(1964)

155. Zel'dovich Ya B, Raizer Yu P *Physics of Shock Waves and High-Temperature Hydrodynamic Phenomena* (New York: Academic Press, 1966, 1967); Translated from Russian: *Fizika Udarnykh Voln i Vysokotemperaturnykh Gidrodinamicheskikh Yavlenii* (Moscow: Nauka, 1966)
156. Peter Th, Meyer-ter-Vehn J *Phys. Rev. A* **43** 2015 (1991)
157. Blaum K, Eliseev S, Sturm S *Quantum Sci. Technol.* **6** 014002 (2021)
158. Oganessian Yu Ts *Pure Appl. Chem.* **76** 1715 (2004)
159. Betz H-D *Rev. Mod. Phys.* **44** 465 (1972)
160. Winckler N et al. *Nucl. Instrum. Meth. Phys. Res. B* **392** 67 (2017)
161. Shevelko V P, Andreev S N, Tolstikhina I Yu *Nucl. Instrum. Meth. Phys. Res. B* **502** 37 (2021)
162. Shevelko V P, Winckler N, Tolstikhina I Yu *Nucl. Instrum. Meth. Phys. Res. B* **479** 23 (2020)
163. Imai M, Tolstikhina I Yu, Shevelko V P *Nucl. Instrum. Meth. Phys. Res. B* **520** 13 (2022)
164. Betz H D "Heavy ion charge states", in *Applied Atomic Collision Physics* Vol. 4 *Condensed Matter* (Ed. S Datz) (New York: Academic Press, 1983)
165. Thieberger P et al. *IEEE Trans. Nucl. Sci.* **32** 1767 (1985)
166. Weick H "Programs to predict charge-state distributions of swift heavy ions", https://web-docs.gsi.de/~weick/charge_states/
167. The program LISE, http://lise.nscl.msu.edu/lise.html
168. Rozet J P, Stéphan C, Vernhet D *Nucl. Instrum. Meth. Phys. Res. B* **107** 67 (1996)
169. Lamour E et al. *Phys. Rev. A* **92** 042703 (2015)
170. Allison S K *Rev. Mod. Phys.* **30** 1137 (1958)
171. Frank A et al. *Phys. Rev. Lett.* **110** 115001 (2013)
172. Jacoby J et al. *Phys. Rev. Lett.* **74** 1550 (1995)
173. Morales R *Phys. Plasmas* **29** 093112 (2022)
174. Gu M F *Can. J. Phys.* **86** 675 (2008)
175. Bauche-Arnoult C, Bauche J, Klapisch M *Phys. Rev. A* **20** 2424 (1979); *Phys. Rev. A* **25** 2641 (1982)
176. Safronova U I et al. *Phys. Scr.* **73** 143 (2006)
177. Altun Z et al. *Astron. Astrophys.* **420** 775 (2004)
178. Cowan R D *The Theory of Atomic Structure and Spectra* Vol. 3 (Berkeley, CA: Univ. of California Press, 1992)
179. Badnell N R *J. Phys. B* **19** 3827 (1986)
180. Kwon D-H, Lee W *J. Quant. Spectrosc. Radiat. Transf.* **179** 98 (2016)
181. Sasaki A, Murakami I *J. Phys. B* **46** 175701 (2013)
182. Wu Z et al. *Atoms* **3** 474 (2015)
183. Klapisch M *Comput. Phys. Commun.* **2** 239 (1971)
184. Tolstikhina I Yu, Imai M, Shevelko V P *Nucl. Instrum. Meth. Phys. Res. B* **532** 27 (2022)